



### 저작자표시-비영리-동일조건변경허락 2.0 대한민국

이용자는 아래의 조건을 따르는 경우에 한하여 자유롭게

- 이 저작물을 복제, 배포, 전송, 전시, 공연 및 방송할 수 있습니다.
- 이차적 저작물을 작성할 수 있습니다.

다음과 같은 조건을 따라야 합니다:



저작자표시. 귀하는 원저작자를 표시하여야 합니다.



비영리. 귀하는 이 저작물을 영리 목적으로 이용할 수 없습니다.



동일조건변경허락. 귀하가 이 저작물을 개작, 변형 또는 가공했을 경우에는, 이 저작물과 동일한 이용허락조건하에서만 배포할 수 있습니다.

- 귀하는, 이 저작물의 재이용이나 배포의 경우, 이 저작물에 적용된 이용허락조건을 명확하게 나타내어야 합니다.
- 저작권자로부터 별도의 허가를 받으면 이러한 조건들은 적용되지 않습니다.

저작권법에 따른 이용자의 권리는 위의 내용에 의하여 영향을 받지 않습니다.

이것은 [이용허락규약\(Legal Code\)](#)을 이해하기 쉽게 요약한 것입니다.

[Disclaimer](#)

공학박사학위논문

**Study on Transient Response Characteristics of a  
PEM Fuel Cell related with Structure and  
Degradation Effects of a Gas Diffusion Layer**

기체확산층의 구조 및 내구저하에 따른  
고분자 전해질형 연료전지의 과도응답 특성에 관한  
연구

2012 년 8 월

서울대학교 대학원

기계항공공학부

조 준 현

**Study on Transient Response Characteristics of a  
PEM Fuel Cell related with Structure and  
Degradation Effects of a Gas Diffusion Layer**

지도교수 민 경 덕

이 논문을 공학박사 학위논문으로 제출함

2012 년 8 월

서울대학교 대학원

기계항공공학부

조 준 현

조준현의 공학박사 학위논문을 인준함

2012 년 5 월

위 원 장           송 성 진           (인)

부위원장           민 경 덕           (인)

위 원           안 성 훈           (인)

위 원           송 한 호           (인)

위 원           이 은 숙           (인)

## Acknowledgements

This project on my Ph.D thesis would not be happened without the advices and helps of following people.

First and foremost, I would like to express my respect and gratitude to my advisor, Professor Kyoungdoug Min. During the graduate course, my knowledge and personality were grown up with his invaluable advices. He gave the inspirations of this study and his guidance and encouragement were the source of power overcoming many difficulties during the project. I would like to special thanks to the project members who offered assistance, valuable discussions and beautiful memories of friendship. Jaeman Park and Hwanyeong Oh assisted lots of the study. Dr. Taehun Ha, Dr. Sanggyu Kang and Professor Han-Sang Kim also gave basic knowledge and inspirations as a senior. This work would never have been achieved without their efforts and patients. Also, I'd like to thanks to my graduate schoolmate Sangyul Lee and BCS member Daebong Jung for unforgettably joyful lab life.

It was an honor to have the opportunity to work with Hyupjin INC and I'd like to thanks to Dr. Eunsook Lee, Dr. Jy-Young Jyoung for the financial, material supports and comments from plentiful experiences on development of the gas diffusion layer. Also I'd like to thanks to Jeong Hwan Chun for active helps and to Sang Gun Lee, Dr. Jung Ho Kang and Professor Charn-Jung Kim.

I would like to present my deepest respect and gratitude to my parents, Hyodeuk Cho and Youngsook Hwang, for their great sacrifice, thoughtful consideration, unimaginable patience, and endless love. I extended my thanks to Sohyun Cho my lovely sister for her thoughtful consideration.

## **Abstract**

# **Study on Transient Response Characteristics of a PEM Fuel Cell related with Structure and Degradation Effects of a Gas Diffusion Layer**

Junhyun Cho

School of Mechanical and Aerospace Engineering

The Graduate School

Seoul National University

The transient response characteristics and durability problems of proton-exchange membrane fuel cells are important issues for the application of PEM fuel cells to automotive systems due to a frequent load change and a requirement for a long term operation. Gas diffusion layer (GDL) is the key component of the fuel cell because it directly influences the mass transport mechanism. Thus, the optimal design of the gas diffusion layer is a crucial process to enhance the water management ability for better performance of the PEM fuel cell. However, few papers have attempted to study dynamic behaviors and durability issues related with the gas diffusion layer. In addition, it is difficult to directly analyze two-phase mass transport mechanism inside the GDL by both experimental and numerical methods. In this study, the transient response of a PEM fuel cell related with characteristics of the GDL and GDL degradation effects is studied by analyzing various experimental results and proven theories.

At first, a systematic transient response and cathode flooding phenomena during the load change are investigated in order to determine effects of operating conditions. The cell voltage was acquired according to the current density

change under a variety of stoichiometric ratio, temperature and humidity conditions, as well as different flooding intensities. Using the transparent fuel cell, the cathode gas channel images are obtained simultaneously with a CCD imaging system. It is shown that the undershoot behavior consists of two stages with different time delays; one is on the order of 1 second and the other is on the order of 10 seconds. It takes about 1 second for the product water to come up to the flow channel surface so that the oxygen supply is temporarily blocked, which causes voltage loss in that "undershoot". The correlation of the dynamic behavior with stoichiometric ratio and cathode flooding is analyzed from the results of these experiments.

Secondly, structural effects of the GDL on the transient response were investigated. Design parameters were varied in each GDL structure which consists of substrate, micro porous layer (MPL) and MPL penetration part. The activated carbon fiber (ACF) which has a large surface area is added in the substrate to enhance attachment of components such as carbon fillers, resins and PTFE, thereby controlling a pore structure of the substrate. Thickness of the MPL penetration was varied to investigate effects of the MPL penetration part. The MPL slurry density was varied and functional structures which have less hydrophobic layer and pore path were added in the MPL. All these design parameters affect the water management ability of the GDL inducing different characteristics of the transient response of the PEM fuel cell. In special, GDLs, which have a better water holding ability, enhance the recovery of voltage performance after undershoot because the GDL increases water supply to the dehydrated membrane due to a higher concentration of water in the GDL. It was shown that capillary pressure gradient is main driving force through the GDL and this capillary pressure gradient is determined by structure of the GDL. The correlation of the transient response with water management characteristics of the GDL which affect the water content of the membrane was investigated.

Finally, the effects of GDL degradation on the transient response of the PEM fuel cell were systematically studied. With GDLs aged by the accelerated stress test, the effects of hydrophobicity and structural changes due to carbon and hydrophobicity loss in the GDL on the transient response of PEM fuel cells were determined. The degraded GDLs that had changed capillary pressure gradient cause local water flooding inside the GDL inducing uneven membrane hydration and oxygen depletion, thereby causing lower and unstable voltage responses after the load changes. Dissolution aging and corrosion aging induces degradation at different location of the GDL respectively, thereby different performance decrease phenomena were obtained. Using a pore network modeling (PNM) of the aged GDL, this phenomenon is also verified. A water-lake is formed inside the GDL where water tends to stay in lower capillary energy spots.

This systematic research on the transient response of the PEM fuel cell related with the characteristics and degradation effects of the GDL contributes to the evaluation of fuel cell modeling, development of optimal cell design, and the construction of control logic and driving strategy for a fuel cell vehicle.

Keywords: Polymer electrolyte membrane fuel cell (PEMFC), Gas diffusion layer (GDL), Transient response, Dynamic behavior, Degradation, Durability

Student Number: 2008-30198

# Contents

<b>Acknowledgements</b> .....	<b>iii</b>
<b>List of Tables</b> .....	<b>x</b>
<b>List of Figures</b> .....	<b>xi</b>
<b>Acronym</b> .....	<b>xviii</b>
<b>Chapter 1. Introduction</b> .....	<b>1</b>
<b>1.1 Backgrounds and Motivations</b> .....	<b>1</b>
1.1.1 Polymer electrolyte membrane fuel cell .....	1
1.1.2 Major issues in the PEM fuel cell.....	2
1.1.3 Gas diffusion Layer.....	4
<b>1.2 Literature Review</b> .....	<b>5</b>
<b>1.3 Objectives</b> .....	<b>12</b>
<b>Chapter 2. Transient response of a PEM fuel cell under various operating conditions</b> .....	<b>17</b>
<b>2.1 Experimental setup</b> .....	<b>18</b>
2.1.1 Fuel cells and test station.....	18
2.1.2 Experimental conditions .....	19
2.1.2.1 Experiments with the large-effective-area PEM fuel cell.....	19
2.1.2.2 Experiments with the transparent PEM fuel cell .....	20

<b>2.2 Experimental results .....</b>	<b>21</b>
2.2.1 Transient voltage response under various operating conditions.....	21
2.2.2 Transient voltage response related with water production during load change using the transparent cell.....	24

**Chapter 3. Transient response of a PEM fuel cell related with structure design of the gas diffusion layer .....38**

<b>3.1 Design parameters of GDL structure.....</b>	<b>38</b>
<b>3.2 Experimental setup .....</b>	<b>42</b>
3.2.1 Fuel cell and test station.....	42
3.2.2 Experimental conditions .....	43
<b>3.3 Experimental results .....</b>	<b>44</b>
3.3.1 Effects of pore structure of the substrate on transient response of the PEM fuel cell .....	44
3.3.2 Effects of MPL penetration thickness on transient response of the PEM fuel cell .....	53
3.3.3 Effects of MPL density on transient response of the PEM fuel cell.....	57
3.3.4 Effects of functional structure of the MPL on transient response of the PEM fuel cell .....	60

**Chapter 4. Transient response of a PEM fuel cell with a degraded gas diffusion layer .....99**

<b>4.1 Experimental setup .....</b>	<b>100</b>
4.1.1 Aging of the GDL.....	100
4.1.1.1 Degradation of the GDL due to dissolution .....	100

4.1.1.2 Degradation of the GDL due to carbon corrosion .....	101
4.1.2 Fuel cell and test station.....	102
4.1.3 Experimental conditions .....	102
<b>4.2 Experimental results .....</b>	<b>104</b>
4.2.1 Transient response of a PEM fuel cell with an aged GDL degraded by dissolution.....	104
4.2.1.1 Change of GDL properties due to dissolution.....	104
4.2.1.2 Transient response change due to dissolution .....	105
4.2.2 Transient response of a PEM fuel cell with an aged GDL degraded by carbon corrosion.....	109
4.2.2.1 Change of GDL properties due to carbon corrosion .....	109
4.2.2.2 Transient response change due to carbon corrosion .....	111
<b>4.3 Numerical study using pore network modeling.....</b>	<b>114</b>
4.3.1 Simulation of the degraded GDL.....	114
4.3.2 Simulation results .....	116
 <b>Chapter 5. Conclusions .....</b>	 <b>144</b>
 <b>Bibliography .....</b>	 <b>150</b>
 초    록.....	 160

## List of Tables

Table 2.1 Experimental conditions for the large effective area fuel cell .....	27
Table 2.2 Experimental conditions for the transparent fuel cell .....	28
Table 3.1 Target boundary of the GDLs .....	65
Table 3.2 Experimental cases. ....	66
Table 4.1 Experimental cases. ....	118
Table 4.2 Voltage performance loss using the degraded GDL under various operating conditions. ....	119
Table 5.1 Summary of GDL structure effects on the transient response of the PEM fuel cell .....	147

## List of Figures

Figure 1.2 Schematic of basic structure and water balance of the PEM fuel cell [3].....	15
Figure 1.3 Structure of the gas diffusion layer .....	16
Figure 2.1 Experimental apparatus for testing the 330 cm <sup>2</sup> PEM fuel cell [97, 98].....	29
Figure 2.2 Unit 25 cm <sup>2</sup> transparent PEM fuel cell [97, 98].....	30
Figure 2.3 Sudden step change of current for large fuel cell (low-load-to-high-load) [97, 98].....	31
Figure 2.4 The voltage response as current is changed from 100 A to 330 A under (a) excess-to-normal and (b) excess-to-starved stoichiometric conditions, with a temperature of 70 °C, humidity of 100 / 100 % and pressure of 1 bar [97, 98].....	32
Figure 2.5 The schematic of voltage undershoot behavior during current step change (low-load-to-high-load) [97, 98].....	33
Figure 2.6 The voltage response as current is changed from (a) 100 A to 200 A, (b) 200 A to 100 A under various humidity conditions, temperature of 70 °C, excess-to-normal stoichiometric ratio (1.2/2.0) and pressure of 1 bar [97, 98].....	34

Figure 2.7 Images of cathode channel flooding at cathode stoichiometric ratio of 1.6, temperature of 40 °C, humidity of 100 / 100 %, and pressure of 1 bar [97, 98] .....	35
Figure 2.8 The modified 1 <sup>st</sup> time delay of undershoot as a saturation level of the GDL .....	36
Figure 2.9 Characteristics of transient response of the PEM fuel cell .....	37
Figure 3.1 Trade-off relation of the GDL as a humidification conditions .....	67
Figure 3.2 Schematic of target boundary of the GDL as design parameters in (a) the substrate, (b) the MPL penetration part and (c) the MPL .....	69
Figure 3.3 The activated carbon fiber (ACF) .....	70
Figure 3.4 Experimental apparatus for testing various types of the GDL .....	71
Figure 3.5 Experimental apparatus for measuring water permeability of the GDL [53] .....	72
Figure 3.6 Schematic and FESEM images (200 x magnifications) of GDL which have different pore structure in the substrate .....	73
Figure 3.7 Pore size distributions of substrate designed samples: (a) all samples, (b) ACF-0/ACF-5/ACF-10, and (c) ACF10-80/ACF10-70/ACF10-60 .....	75
Figure 3.8 FESEM image of the ACF-10 (1000 x magnifications) .....	76
Figure 3.9 The steady-state performance of the ACF-0/ACF-5/ACF-10 at (a) an RH of 100 %, (b) 50 %, and (c) 30 % .....	77

Figure 3.10 The voltage response of the ACF-0/ACF-5 as the current was changed from 15 A to 30 A at (a) an RH of 100 %, (b) 50 %, and (c) 30 %.....	78
Figure 3.11 The steady-state performance of the ACF10-80/ACF10-70/ACF10-60/ACF-0 at (a) an RH of 100 %, (b) 50 %, and (c) 30 %.....	79
Figure 3.12 The voltage response of the ACF10-70/ACF10-60/ACF-0 as the current was changed from 15 A to 30 A at (a) an RH of 100 %, and (b) 30 %.....	80
Figure 3.13 Schematic of relation between GDL water content and membrane hydration .....	81
Figure 3.14 Capillary pressure gradient through the GDL.....	82
Figure 3.15 Schematic of formation of capillary pressure gradient in the substrate .....	83
Figure 3.16 Capillary pressure difference between the relatively large macro pore (LMP) and relatively small macro pore (SMP) .....	84
Figure 3.17 Sectional FESEM images of (a) MP-A, (b) MP-B, and (c) MP-C which has different MPL penetration thickness.....	85
Figure 3.18 Pore distributions of MP-A, MP-B and MP-C which has different MPL penetration thickness .....	86
Figure 3.19 Water permeability of MP-A, MP-B and MP-C which has different MPL penetration thickness.....	87

Figure 3.20 The voltage response of MP-A and MP-C as the current was changed from 15 A to 30 A at an RH of 100 % and an SR of H <sub>2</sub> /Air of (a) 1.5/1.6 (starved), (b) 1.5/2.0 (standard), and (c) 1.5/4.0 (excess).....	88
Figure 3.21 The voltage response of MP-A and MP-C as the current was changed from 15 A to 30 A at an RH of 50 % and an SR of H <sub>2</sub> /Air of (a) 1.5/1.6 (starved), (b) 1.5/2.0 (standard), and (c) 1.5/4.0 (excess) .....	89
Figure 3.22 Standard deviation of the voltage as the current density was varied from 0.6 A/cm <sup>2</sup> to 1.6 A/cm <sup>2</sup> with MP-A and MP-C at an RH of 100 % and an SR of H <sub>2</sub> /Air 1.5/2.0 .....	90
Figure 3.23 Schematic of formation of capillary pressure gradient in the MP-A and MP-C.....	91
Figure 3.24 Schematic and FESEM images of MD-A,B and C .....	92
Figure 3.25 The voltage response of the MD-A/MD-B/MD-C as the current was changed from 15 A to 30 A at (a) an RH of 100 %, (b) 50 %, and (c) 30 % .....	93
Figure 3.26 Schematic of formation of capillary pressure gradient in the MD-A, MD-B and MD-C.....	94
Figure 3.27 FESEM image of the MPL surface of MF-C .....	95
Figure 3.28 The voltage response of the MF-A/MF-B/MF-C as the current was changed from 15 A to 30 A at (a) an RH of 100 % and (b) 50 %.....	96

Figure 3.29 Schematic of formation of capillary pressure gradient in the MF-A, MF-B and MF-C .....	97
Figure 3.30 Design of pore size distribution of the GDL .....	98
Figure 4.1 Experimental procedure of leaching test .....	120
Figure 4.2 Experimental apparatus of three-electrodes carbon corrosion test ...	121
Figure 4.3 Changes in the contact angle of the GDL during the leaching test ..	122
Figure 4.4 SEM image of loss of hydrophobic carbonized resins after the leaching test.....	123
Figure 4.5 The voltage response as the current was changed from 15 A to 30 A at an RH of 100 % and an SR of H <sub>2</sub> /Air of (a) 1.5/1.6 (starved), (b) 1.5/2.0 (standard), and (c) 1.5/4.0 (excess).....	124
Figure 4.6 The voltage response as the current was changed from 15 A to 30 A at an RH of 50 % and an SR of H <sub>2</sub> /Air of (a) 1.5/1.6 (starved), (b) 1.5/2.0 (standard), and (c) 1.5/4.0 (excess).....	125
Figure 4.7 Enlarged area of Figure 4.6, which shows the change from 15 A to 30 A at an RH of 50 % and an SR of H <sub>2</sub> /Air of (a) 1.5/1.6 (starved), (b) 1.5/2.0 (standard), and (c) 1.5/4.0 (excess) .....	126
Figure 4.8 Standard deviation of the voltage as the current density was varied from 0.6 A/cm <sup>2</sup> to 1.6 A/cm <sup>2</sup> with fresh and aged GDLs at an RH of 50 and 100 % and an SR of H <sub>2</sub> /Air 1.5/2.0.....	127
Figure 4.9 Schematic of local flooding in an aged GDL.....	128

Figure 4.10 The voltage response as the current was changed from 30 A to 15 A at an RH of 50 % and an SR of H <sub>2</sub> /Air of (a) 1.5/1.6 (excess), (b) 1.5/2.0 (more excess), and (c) 1.5/4.0. (most excess).....	129
Figure 4.11 Weight (a) and thickness (b) change after carbon corrosion for MP-A and MP-C.....	130
Figure 4.12 Schematic of carbon corrosion in the MPL penetration part .....	131
Figure 4.13 Pore distributions before/after carbon corrosion of MP-A (a) and MP-C (b).....	132
Figure 4.14 FESEM images before/after carbon corrosion of MP-A and MP-C .....	133
Figure 4.15 Contact angle changes before/after carbon corrosion of MP-A and MP-C on substrate surface (a) and MPL surface (b) .....	134
Figure 4.16 Water permeability change before/after carbon corrosion of MP-A and MP-C.....	135
Figure 4.17 Steady-state performance before/after carbon corrosion of MP-A and MP-C.....	136
Figure 4.18 The voltage response of fresh MP-C and aged MP-C as the current was changed from 15 A to 30 A at an RH of 100 % and an SR of H <sub>2</sub> /Air of (a) 1.5/1.6 (starved), (b) 1.5/2.0 (standard), and (c) 1.5/4.0 (excess).....	137
Figure 4.19 The voltage response of fresh MP-C and aged MP-C as the current was changed from 15 A to 30 A at an RH of 50 % and an	

SR of H <sub>2</sub> /Air of (a) 1.5/1.6 (starved), (b) 1.5/2.0 (standard), and (c) 1.5/4.0 (excess).....	138
Figure 4.20 Schematic of water accumulation phenomena in the aged GDL due to (a) dissolution effect caused by leaching test and (b) carbon corrosion effect.....	139
Figure 4.21 Calculation domain of the simulated aged GDL.....	140
Figure 4.22 Pore-network generation: (a) regularly arranged cubic cells, (b) box-shaped pores and throats, (c) liquid water droplet in box-shaped pore, and (d) invading front of liquid water through hydrophobic rectangular throat [61].....	141
Figure 4.23 Simulation results of liquid water saturation distribution before (a)/after (b) aging of the GDL.....	142
Figure 4.24 Liquid saturation changes of the xy-plane along z-coordinate before/after aging of the GDL.....	143
Figure 5.1 Summary of the transient response of the PEM fuel cell.....	149

## Acronym

CL	Catalyst Layer
FESEM	Field Emission Scanning Electronic Microscope
GC	Gas Channel
GDL	Gas Diffusion Layer
GDBL	Gas Diffusion Backing Layer
LBM	Lattice Boltzmann Model
LMP	Large Macro Pore
MPL	Micro Porous Layer
PEM	Proton Exchange Membrane, Polymer Electrolyte Membrane
PNM	Pore Network Model
PTFE	Poly-TetraFluoroEthylene
RH	Relative Humidity
SEM	Scanning Electronic Microscope
SMP	Small Macro Pore
SR	Stoichiometric Ratio

# **Chapter 1. Introduction**

## **1.1 Backgrounds and Motivations**

### **1.1.1 Polymer electrolyte membrane fuel cell**

The requirement for eco-friendly vehicles has been emphasized due to air pollution, global warming and depletion of the energy. The polymer electrolyte membrane fuel cell (PEMFC) is considered to be the best alternative to the internal combustion engine in automotive applications due to its low operating temperature (under 80 °C), high power density and high efficiency [1]. Many researchers have reported that the fuel cell electric vehicle (FCEV) will be the major type of the vehicle in the near future. After introducing an early stage model of the fuel cell vehicles last decade, many automotive manufacturers have attempted to develop commercial fuel cell vehicles. As shown in Figure 1.1, The market share of the fuel cell electric vehicle is expected to encroach 90 % of the total number of vehicle sales in 2040 [2]. To make fuel cell era, production of the hydrogen, construction of hydrogen infrastructure and cost-down also have to be improved.

The polymer electrolyte membrane fuel cell which is also called as the proton exchange membrane fuel cell is one kind of the fuel cell which generates electric energy by an electrochemical reaction of fuels and oxidants. The fuel cell can be classified by a type of the electrolyte determined by its operating temperature. The PEM fuel cell uses a polymer electrolyte to transfer protons from the anode side to the cathode side. A schematic of basic structure and water balance of the PEM fuel cell is shown in Figure 1.2 [3]. The catalyst layer where

the electrochemical reaction occurs is attached to both sides of the membrane. The hydrogen is supplied to the anode side and the oxygen in the air is supplied to the cathode side. To enhance mass transfer from the gas channel which is machined on the bipolar plate, the gas diffusion layer (GDL) is inserted between the bipolar plate and the catalyst layer. The gas diffusion layer is a porous medium which consists of carbon fibers. In addition, to reduce contact resistance and to enhance capillary pressure of the GDL, the micro porous layer (MPL) - which has a very small pore structure due to the use of carbon powder - is adopted between the catalyst layer and the GDL. In general, the GDL includes the MPL. Since the product of the PEMFC is only water, the PEM fuel cell is a zero-emission energy source [4].

### **1.1.2 Major issues in the PEM fuel cell**

The PEM fuel cell has some technical issues that have to be solved before commercializing systems. The primary goal is to achieve a fast and a stable dynamic operation of a PEM fuel cell in response to drivers' power requirements such as start-up, acceleration, and deceleration. In addition, enhanced durability of the fuel cell to sustain a stable long term operation is required to meet consumer's needs.

Major issues in the PEM fuel cell can be summarized as low humidity operation, flooding phenomena and durability problems. Since the membrane conductivity, which is a dominant factor to the performance of the PEM fuel cell, is determined by the membrane water content, a water supply system is required. To enhance membrane water content, the reactant gases are humidified by the external humidifier so that the relative humidity of the cell and reactant gases is maintained as a high level. However, this causes additional power loss in the system level because additional energy is required to maintain the operating

temperature of the humidifier and to overcome the pressure resistance through the humidifier [5, 6]. Also, a high humidification operating condition induces a flooding phenomenon in the fuel cell that saturated water blocks the mass transfer of the reactant gases [7]. Thus, requirements for the low humidification operation are increased to enhance the net efficiency of the fuel cell system [8]. However, removing or reducing the humidification system is challenging work because the performance of the fuel cell can be deteriorated due to low membrane conductivity induced by decrease in the supplied water. Thus, studies about maintaining the optimal water content of the membrane are required.

On the other hand, the flooding phenomena are inevitable in the fuel cell vehicle application because instantaneous increase of the product water temporally blocks the passage of the reactant gases in case of acceleration. Also, water is accumulated inside a cell in case of the high-load operations causing flooding. Since the load change in automotive applications is frequent and rapid, studies about the dynamic behavior and the flooding phenomena of the PEM fuel cell are important [9].

Finally, durability problem is major issue in recent researches. To commercialize the PEM fuel cell vehicle, 5000 hours operating time is required. The U.S. DOE (Department of Energy) have targeted and driven this goal, and many researchers have made an effort to achieve a stable and a robust long term operation [10]. The PEM fuel cell system has catalyst, water, gas flows, carbon materials, temperature gradient and transfer of electrons which induce degradation of the system with a high possibility. Thus, investigation on the mechanism of degradation of each part, the characteristic change after aging and mitigation strategies is essential.

All these major issues are ultimately related with the optimal and the consistent mass balance in the PEM fuel cell. The major component that determines the mass balance is the gas diffusion layer.

### **1.1.3 Gas diffusion Layer**

The GDL which is located between the bipolar plate and the catalyst layer is a key component of a PEM fuel cell at high load operating conditions because it works as a passage for mass transport, such as supplying hydrogen and air, water from by humidification and water produced in the cell [11, 12]. Since water flooding reduces the mass transport ability, which decreases the performance, the GDL has hydrophobic characteristics to improve water removal with high capillary forces [13, 14]. The structure of the GDL is described in Figure 1.3. The GDL consists of two main parts; the gas diffusion backing layer (GDBL) called as a substrate and the MPL which is coated on the GDBL. The substrate and the MPL has a pore structure whose pore size is order of  $0.1 \sim 1 \mu\text{m}$  and  $10 \sim 100 \mu\text{m}$  respectively. The substrate is composed of carbon fibers, carbon fillers, carbonized resins and poly-tetrafluoroethylene (PTFE). The MPL is composed of carbon powder and PTFE. The MPL has been developed to enhance water management and electrical contact [15]. When the MPL is coated on the GDBL, carbon particles of the MPL penetrate through the GDBL forming penetration part.

## 1.2 Literature Review

The dynamic performance of the PEM fuel cell in automotive applications is very important due to rapid and frequent load changes. While most of the studies regarding PEM fuel cells have focused on steady-state behavior, several papers have recently studied the dynamic behavior of PEM fuel cells. However, the majority of this research involves numerical simulation studies.

Ceraolo et al. developed a simplified one-dimensional dynamic model of a PEM fuel cell based on MATLAB/SIMULINK® [16]. Shan et al. predicted the transient response of a PEM fuel cell to an electric load. The model separated the fuel cell into several layers: membrane, catalysts, gas diffusion layer and bipolar plates [17]. Song et al. studied the transient behavior of water transport in the cathode gas diffusion layer using a one-dimensional, non-isothermal, two-phase transient PEM fuel cell model [18].

By developing a three-dimensional dynamic model of the PEM fuel cell, Wang et al. showed that it takes about 10 seconds for the cell to reach a new steady-state condition and that the main reason for this behavior is the water accumulation effect in the membrane [19]. They also studied transient phenomena under current density step changes, focusing on dry cell operation. They concluded that a step increase in the current density instantaneously dries out the anode under the influence of an electro-osmotic drag [20]. This study, however, focused on a single channel model only instead of the conventional cell configuration. In a recent paper, the same group developed a two-phase transient model and analyzed the dynamics of GDL dewetting and its impact on PEM fuel cell performance [21, 22]. Yan et al. studied the effects of gas channel type and the porosity of the gas diffusion layer on the dynamic performance of a

PEM fuel cell using a two-dimensional mass transfer model in the cathode side [23].

Shimpalee et al. estimated undershoot/overshoot behavior of a PEM fuel cell under a fixed stoichiometric ratio condition by using a three-dimensional model simulation. They recently predicted dynamic behavior with a modified model that incorporates water phase change [24-26]. Kumar et al. studied the steady and transient state performance of a PEM fuel cell for different gas flow channel shapes. Their results showed that it takes about 10 seconds for the fuel cell to reach a new steady state after a load change [27].

Mueller et al. developed a quasi-three dimensional dynamic model for controlling a PEM fuel cell. The spatial dynamic behavior of current, water flux, species mole fractions and fuel cell temperature were presented [28]. Kang et al. improved the model to investigate effects of air, fuel, and coolant inlets on the dynamic performance of a proton exchange membrane fuel cell for automotive applications [29]. Hou et al. developed a semi-empirical dynamic model on the basis of experimental results [30]. Ning et al. investigated a dynamic behavior and control strategy [31]. Qu et al. presented numerical investigation of undershoot behavior related with a membrane water content [32]. Khajeh-Hosseini-Dalasm et al. also developed a three-dimensional transient two-phase isothermal model for the cathode side of a proton exchange membrane fuel cell. The time variations of liquid water distribution in along-channel and through-plane directions are investigated [33]. Loo et al. developed a one-dimensional, two-phase, dynamic model of the PEM fuel cell and investigated dynamic response of under various operating conditions [34].

In contrast, few papers have experimentally analyzed the transient response of a PEM fuel cell. Kim et al. performed experimental research on

undershoot/overshoot behavior of PEM fuel cells under different stoichiometric ratio conditions. They also demonstrated the effects of fuel dilution and hydrogen reservoir on the dynamic performance of PEM fuel cells. In addition, they investigated the effect of channel type on the transient response [35-37]. Yan et al. showed various experimental results on the dynamic behavior of a PEM fuel cell under different temperatures, humidities, flow rates and flow channel type conditions. However, specific experimental conditions were not defined clearly, and their study was somewhat limited due to the lack of analysis of the causes of dynamic behavior [38]. Recently, several papers have addressed the experimental relationship between membrane resistance and dynamic performance. Weydahl et al. analyzed the transient response of a single PEM fuel cell through resistance step measurements assisted by EIS and chronoamperometry [39]. Takaichi et al. measured the dynamic change of specific resistances of PEM fuel cells at various positions [40]. Tang et al. showed experimental investigation of dynamic performance and transient responses of a kW-class PEM fuel cell stack [41].

However, these previous studies about the dynamic behavior of the PEM fuel cell were concentrated on phenomenal results. Causes of the transient behavior were not systematically investigated in experimental researches. In case of dynamic modeling studies, effects of the GDL on the transient response are simply concerned despite the GDL is a key component of mass transport in the PEM fuel cell. Although the GDLs have a variety of characteristics, simplified expression for mass transport in the GDL is used. In addition, dynamic two-phase models, developed by various institutes, are different to each other and models are in an early stage due to complexity and difficulty of mathematical analysis of a dynamic gas-liquid behavior in the porous medium. Furthermore, many numerical studies were only concerned with small fuel cells with an effective area of 5 to 25 cm<sup>2</sup> or even single channel cells because of

difficulties associated with meshing and computing. Consequently, these studies were limited with respect to real automotive applications because many companies use fuel cells with an effective area of 200~350 cm<sup>2</sup>. Furthermore, parametric studies or reports of the transient behavior have been rare. Thus, a systematic experimental study on the dynamic behavior related with various operating conditions and mass transfer characteristics in the GDL is required.

Since the GDL is a passage of the water and gas, studies about the effects of a change in the hydrophobicity of the GDBL were widely investigated in an early stage [42-47]. Effects of a GDBL type such as carbon felt, paper and clothes were investigated in several studies [48-50]. After that, to enhance water management and electrical contact, the MPL has been developed [51, 52]. In recent stage, passage design issues of the GDL have been focused to enhance performance of the PEM fuel cell in an active way. Chun et al. controlled pore size distribution of the micro porous layer using a pore former agent [53] and they also developed a novel hydrophobic-hydrophilic double micro porous layer [54]. Weng et al. developed a hydrophobic gradient micro porous layer [55] and Tang et al. developed a porosity-graded micro porous layer [56]. Manahan et al. controlled size and patterns of pores using by laser perforation [57]. Furthermore, novel artificial metallic gas diffusion layers were developed by Zhang et al. [58]. To investigate mass transport phenomena inside of the GDL, visualization method was developed. Santamaria et al. showed the most developed 3-D neutron tomography skills to observe water content of the fuel cell under sub-zero condition [59]. However, it is still difficult to observe water-gas transport phenomena in the GDL which is very thin by through-plane view and under transient condition.

Besides, numerical analysis of mass transport in the GDL has also been reported in recent years. Pore network modes (PNM) [60-65] and Lattice

boltzmann models (LBM) [66-70] are representative numerical studies about two-phase mass transport in the GDL at a pore scale. These models have attempted to investigate micro scale mass transport of water, vapor, hydrogen and oxygen considering a realistic size of control volume simulating the GDL structure.

However, these previous studies only showed characteristics of the GDL and the steady-state performance of the PEM fuel cell. In special, numerical studies about mass transport in the GDL could not connect mass transport characteristics and performance of PEM fuel cell. Various types of the GDL will affect the transient response of the PEM fuel cell due to different characteristics of mass transport. Thus, evaluation of effects of a GDL structure on the transient response is required to enhance the dynamic performance of the PEM fuel cell as well as the steady-state performance by an active passage design of the GDL. In this process, a separate investigation of each component of the GDL is essential because GDL consists of the substrate, the MPL and the MPL penetration part which have different pore size, material, and structure.

Finally, enhancing the durability of PEM fuel cells is a major challenge and a growing focus of research [71, 72]. Thus far, most researchers have mainly focused on the catalyst/membrane for the degradation of PEM fuel cells [73-75]. They have investigated the characteristics of various degradation mechanisms under freeze/thaw cycling [76, 77], carbon corrosion conditions induced by fuel starvation [78-81] and various operating conditions, such as humidification and load cycling [82-85]. It has been found that the main mechanism of degradation of fuel cells is due to platinum catalyst particle agglomeration due to the loss of the carbon support, which decreases the effective reaction surface area [86, 87]. However, few studies have investigated the mechanism and effects of GDL degradation despite its crucial importance to PEM fuel cells [74]. The GDL is

also composed of carbon, similar to catalyst supports, which is a main reason for the degradation of fuel cells. In addition, the GDL is always adjacent to the catalyst layer, which means that it is exposed to a carbon corrosion environment. Furthermore, dissolution effect is expected because there is lots of water transport through the GDL and the cell is maintained above 65°C.

Recently, several studies have reported experimental results on the degradation of the GDL independently. Lee et al. investigated the change of GDL properties, including electrical resistivity, bending stiffness, air permeability, surface contact angle, porosity and water vapor diffusion, under freezing conditions [88]. Parikh et al. showed the effects of deformation of the carbon fibers on the electric resistance of the GDL [89]. Chen et al. showed the impedance changes of PEM fuel cells with hydrophobicity changes due to the degradation of the GDL [90]. Wu et al. also investigated degradation of the GDL at various operating temperatures and gas flow rate conditions [91]. Radhakrishnan et al. presented the property changes of the GDL after cyclic compression stress tests [92]. Ha et al. reported characteristics change of the degraded GDL dividing aging mechanism into dissolution effect of water [93] and carbon corrosion effect due to electrochemical reactions [94]. Through these studies, hydrophobicity aging is considered the main degradation mode of the GDL, wherein the contact angle decreases with time at high temperature and oxidation conditions. Other degradations of the properties are also related to the change of the mass transport characteristics of the GDL.

These studies investigated of the polarization curve of fuel cells. However, studies on how this hydrophobicity change and the related degradation of structure affect the mass transport behavior and dynamic performance are needed [90-96]. As mentioned above, transient response of PEM fuel cell is related with the GDL. It means that the degraded GDL, which has a different

hydrophobicity and structural characteristics, changes the dynamic performance characteristics. However, there are no studies on the effects of GDL aging on the transient response of PEM fuel cells.

## 1.3 Objectives

Transient response, mass transport in the GDL and degradation of the GDL, which are major issues of the PEM fuel cell, have not been connected with each other though the GDL works as a passage of fluids in the PEM fuel cell. Studies on sources and causes of the transient behavior were not enough in experimental researches, and investigations of the relationship between cell performance and mass balance in the GDL were insufficient in numerical studies. Various efforts to improve performance of the PEM fuel cell by redesigning the GDL have focused on the steady-state performance and the transient response characteristics affected by variance of the GDL have not been studied. In addition, there are no studies that include GDL degradation effects on the transient response of the PEM fuel cell. Thus, the objectives of this study are:

1. Investigation of the transient response of the PEM fuel cell under various operating conditions to figure out characteristics and sources of the dynamic behavior by a systematic experimental approach.
2. Investigation of GDL structure effects on the transient response which have different pore distribution, capability of water holding/removal, mass transport passage and so on by designing each part of the GDL which are MPL, MPL penetration part and substrate.
3. Investigation of GDL degradation effects on the transient response which induces characteristic changes of the mass transport and, hence, inducing a change of the transient response of the PEM fuel cell.
4. Ultimately, investigation of mass transport mechanism inside of the GDL directly related to dynamic performance of the PEM fuel cell.

To figure out correlation between mass balance inside of the GDL and dynamic performance of the PEM fuel cell which is impossible to be directly observed in recent level of technology, various types of designed and aged GDLs were experimentally investigated and analyzed with proven governing equations of mass transport in the micro-scale porous medium. Transient response phenomenon is explained by common mass balance mechanism through the GDL.

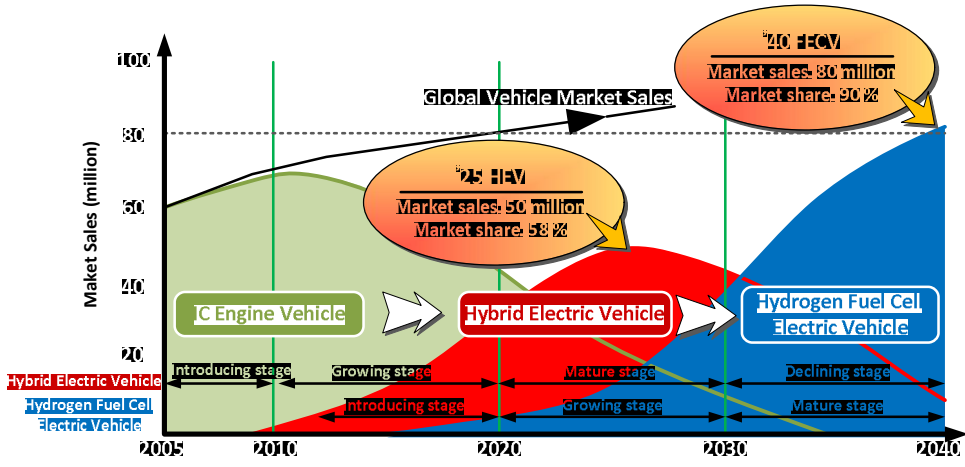


Figure 1.1 Forecast of the future market sales of vehicles [2]

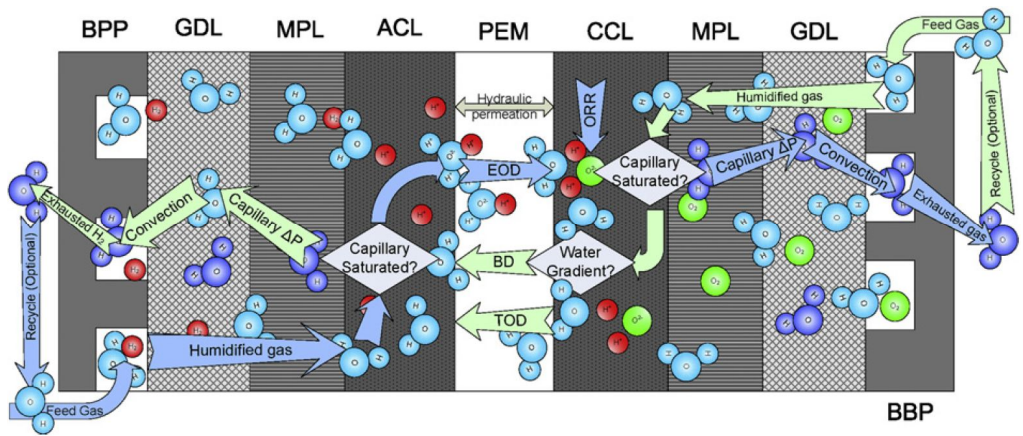


Figure 1.2 Schematic of basic structure and water balance of the PEM fuel cell [3]

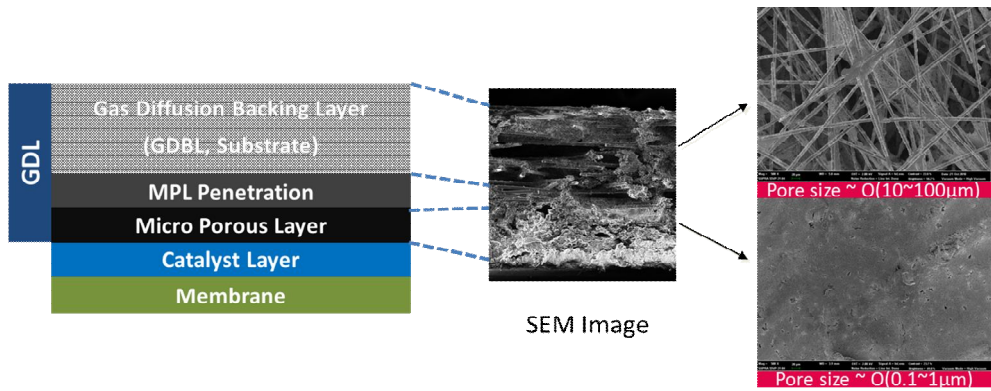


Figure 1.3 Structure of the gas diffusion layer

## **Chapter 2. Transient response of a PEM fuel cell under various operating conditions**

The objectives of this chapter are to analyze characteristics of the transient response of a PEM fuel cell and to determine through experimental methods the operating parameters that influence transient response. This chapter was sophisticatedly introduced in my master's thesis [97] and the previously published paper [98], thus important major results and explanations are introduced to understand transient response of the PEM fuel cell.

First, using a 330 cm<sup>2</sup> unit large fuel cell, dynamic behavior was investigated under various stoichiometric ratios, amounts of load change, temperatures, and humidity conditions to determine how operating conditions affect the transient response of a real automotive-size fuel cell. A direct visualization study using a 25 cm<sup>2</sup> transparent unit fuel cell was then performed to find the relationship between the transient response and the two-phase flow in that cathode flooding. The transparent unit fuel cell is made into a conventional lab scale-sized cell. With these series of experiments, this study tries to demonstrate which operating conditions and water transfer mechanisms influence the transient response of PEM fuel cells.

## 2.1 Experimental setup

### 2.1.1 Fuel cells and test station

The large PEM fuel cell has effective area of  $330 \text{ cm}^2$  (width: 234 mm, height: 141 mm) with a parallel serpentine channel ( $1 \text{ mm} \times 1 \text{ mm}$ ) flow pattern. Its membrane thickness is  $30.48 \text{ }\mu\text{m}$  and the equivalent weight of the dry membrane is 800 ew. It has a coolant channel, and the operating temperature is controlled by the water circulation system.

Figure 2.1 shows the schematic diagram of the test station for the  $330 \text{ cm}^2$  fuel cell. Humidity is controlled by a membrane humidifier at both anode/cathode sides and is also monitored using a humidity sensor. The cell current is controlled by an electric loader (AMREL Inc.). The cell voltage acquisition system consists of the USB 6009 (National Instrument) board and LabVIEW program. The cell voltage data are obtained at 100Hz and analyzed by using a LabVIEW based program.

Figure 2.2 shows the unit transparent fuel cell used for the visualization experiment. A window is used at the cathode side for direct visualization of cathode flooding. A parallel serpentine gas flow channel is fabricated using a thin carbon composite machined sheet (thickness: 1 mm) combined with the acrylic window. A conventional carbon bipolar plate is used at the anode side with a parallel serpentine flow channel type ( $0.8 \text{ mm} \times 1 \text{ mm}$ ). The membrane used in this study is Nafion® 112, which has a thickness of  $50.8 \text{ }\mu\text{m}$  and an effective area of  $25 \text{ cm}^2$ .

The image acquisition system is constructed with a CCD camera (Lumenera Inc.) and Nikon Micro 60 mm lens (Nikon Inc.). The cathode channel images are transferred to a PC and saved once per second during the transient operations. [97, 98]

## **2.1.2 Experimental conditions**

### **2.1.2.1 Experiments with the large-effective-area PEM fuel cell**

In this study, the transient response is defined as the voltage response obtained as a result of a sudden step change of the current as shown in Figure 2.3. To analyze the influence of operating parameters on the transient response characteristics of a large-effective-area fuel cell, different experimental conditions were selected as shown in Table 2.1.

The transient voltage response was obtained under different stoichiometric conditions and the current was step changed between 100 A and 330 A to determine the effect of stoichiometric ratio on the transient response of the fuel cell. Gas flow rates were maintained as a constant and the stoichiometric ratio was changed before and after the load change. The starved condition was set at 80 % (1.0/1.6) of stoichiometric ratio (1.2/2.0). The operating temperature and the humidity were maintained at 70 °C and 100 % at both sides and pressure was fixed at 1 bar.

Second, to determine the influence of load change on the transient voltage response, current was changed from 100 A to 200 A to represent a 50 % power change. An excess-to-normal stoichiometric ratio of 1.2/2.0 anode/cathode side at high load operation, an operating temperature of 70 °C, humidity of 100 % at both sides, and pressure of 1 bar were maintained.

Third, to determine the influence of operating temperature on the transient voltage response, the cell voltage was measured at a current step change from 100 A to 200 A and from 200 A to 100 A at temperatures of 30, 40, 50, 60 and 70 °C. The flow rate was fixed to maintain a stoichiometric ratio of 1.2/2.0 (anode/cathode) at 200 A load. A fully hydrated gas condition and pressure of 1 bar were also maintained.

Finally, to determine the influence of humidity on the transient voltage response, different levels of humidity of hydrogen and air gas such as 50 % and 100 %, respectively, were used. The voltage response was analyzed as a sudden step change of the current: 100 - 200 A and a temperature of 70 °C, pressure of 1 bar and stoichiometric ratio of 1.2/2.0 were maintained. [97, 98]

### **2.1.2.2 Experiments with the transparent PEM fuel cell**

Table 2.2 shows the experimental conditions for the transparent unit cell experiments. In all cases, experiments were conducted at a temperature of 40 °C, hydrogen stoichiometric ratio of 1.2, anode/cathode humidity of 100/100 % and pressure of 1 bar.

The voltage response of the fuel cell was obtained under different stoichiometric conditions as was done in the case of the large-effective-area fuel cell experiments during a step change of the current: 7.5 A to 15 A. The flow rate was fixed so as to maintain the stoichiometric ratio at the high load (15 A) condition. The cathode stoichiometric ratio condition was varied at 2.0 (Normal), 1.6 (Starved) and 4.0 (Excess). Hydrogen stoichiometric ratio was fixed to the 1.2 (Normal) condition. Not only the voltage response of the fuel cell but also the cathode channel image was obtained during the transient operation to analyze the relationship between the cell voltage response performance and the water appearance on the flow channel surface.

Second, to analyze the effect of the mass transfer limit on the transient response, different levels of flooding were enforced by controlling the operating time as 10 seconds and 300 seconds before a load change. The flow rate of the cathode side was fixed at a stoichiometric ratio of 1.6 at the high load condition. The voltage response was recorded corresponding to a sudden step change of current density: 0.3 A/cm<sup>2</sup> (7.5 A) to 0.6 A/cm<sup>2</sup> (15 A). [97, 98]

## 2.2 Experimental results

### 2.2.1 Transient voltage response under various operating conditions

Through many experimental results, characteristics of transient response were investigated. Detailed experimental results were shown in the references [97, 98]. Distinguishing results are shown in Figures 2.4 and 2.6. Figure 2.4 shows the transient voltage response of a large-effective-area cell when the current is changed from 100 A to 330 A under various stoichiometric conditions. A voltage undershoot behavior is observed after a load change. Figure 2.4-(a), the case representing a sufficient amount of gas supply, shows that it takes about 50 seconds to reach a new steady-state condition with a stoichiometric ratio of 1.2/2.0, and 40 seconds and 20 seconds with a stoichiometric ratio of 2.4/2.0 and 1.2/4.0, respectively. This time delay is much longer than the results from previous papers [24-26, 35-37]. This result is due to severe water flooding, which interferes with the mass transfer process; however, simulations were not capable of identifying this phenomenon. In the case of 1.2/2.0 stoichiometric ratio, the voltage decreases continuously after reaching its maximum level. However, when the cathode stoichiometric ratio is 4.0, the voltage remains at the maximum level. This result suggests that long-term voltage loss (as in the 1.2/2.0 case) occurs due to the mass transfer limit of oxygen by cathode flooding at sustained high-load operation. An enlarged graph which is in the Figure 2.4-(a) shows that the voltage does not recover immediately but rather decreases continuously for about 2 seconds after a load change. Also, the time to reach the minimum voltage level decreases as the stoichiometric ratio, especially the cathode stoichiometric ratio, increases.

The schematic of this undershoot behavior is illustrated in Figure 2.5. When the load changes from the low load to the high load, the voltage response exhibits two different time delays until it reaches a new steady state. The first time delay,

which is on the order of 1 second, is the time that the voltage decreases continuously until it reaches the minimum level. The second delay, which is on the order of 10 seconds, is the time until the voltage reaches the new steady state level. The fact that the first time delay decreases as stoichiometric ratio increases, from Figure 2.4-(a), suggests that the gas convection and diffusion process is related to the first time delay. The time to penetrate the GDL for gas is calculated as below:

$$\tau_k \cong \frac{\delta_{GDL}^2}{D_g^{eff}} \quad (2.1)$$

Since the GDL thickness  $\delta_{GDL}$  is around 0.3 mm and the general diffusivity  $D_g^{eff}$  of porous GDL is  $10^{-5} m^2/s$ , the time constant  $\tau_k$  is on the order of 0.01 second [19]. But in this experimental study, the time constant is on the order of 1 second. This difference will be discussed in the latter part of this chapter.

The second stage time delay is due to membrane water content recovery. As the load changes to a high current density, the membrane dehydrates and the membrane resistance correspondingly increases, inducing a voltage loss. In time, due to the supply of humidified gas and internal hydration from electro-osmotic drag and back diffusion, the membrane becomes hydrated, resulting in voltage recovery. The membrane hydration time is estimated to be:

$$\tau_m = \frac{(\rho\delta_m\Delta\lambda)/EW}{I/2F} \quad (2.2)$$

Here,  $\tau_m$  is the time constant for membrane hydration,  $\rho$  is the membrane density,  $\delta_m$  is the membrane thickness,  $\Delta\lambda$  is the water content, EW is the

equivalent weight of the membrane,  $I$  is the current density and  $F$  is the Faraday constant. Inserting typical values, the time constant is found to be on the order of 10 seconds [19].

Figures 2.6-(a) and (b) show the effect of humidity on the transient voltage response. In the case of a load increase, Figure 2.6-(a) shows that the humidity of both hydrogen and oxygen have to be maintained in a fully hydrated state to achieve better transient operation. If there is not enough water supply during a load change, the membrane dehydrates and osmotic drag and back diffusion de-activate, resulting in the decrease of membrane conductivity and mass transfer and an eventual increase in voltage drop. There is a substantial time delay for water accumulation on the membrane compared to the electrochemical reaction time and gas diffusion time, so voltage recovery is slow under the low humidity conditions. As oxygen and hydrogen continues to react and produce water, the membrane becomes hydrated and has low resistance. In the case of anode/cathode humidity of 50/100 %, the continuous back diffusion process helps the recovery of the voltage loss up to a nearly fully hydrated condition. Based on the fact that the voltage loss increases at the low humidity condition, this observation also supports the idea that the second stage time delay shown in the Figure 2.5 is due to the time delay of water content build-up in the membrane.

From these experiments, the humidity of both sides for load increase and any one side for load decrease is a very important factor of the transient response of a PEM fuel cell. And it indicates that water content inside the PEM fuel cell is dominant factor to transient response.

In the series of experiments, the undershoot behavior was observed during low-load-to-high-load change and the overshoot behavior during high-load-to-low-load change. Undershoot behavior is analyzed in more detail to observe two different time delays. In the first stage, the theoretical time delay was on the order of 0.01 second. However, in these experiments, the time delay was found to be on

the order of 1 second. To further investigate this difference in time delay, a visualization study was conducted simultaneously with the voltage performance data analysis. [97, 98]

## **2.2.2 Transient voltage response related with water production**

### **during load change using the transparent cell**

Figure 2.7 shows the cathode gas channel images from 0 second to 3 seconds after the load change at a cathode stoichiometric ratio of 1.6. A steep increase of vapor (white color in channel in image figures) is observed in the image after 2 seconds, which indicates that it takes about 1 second for the water produced at the catalyst layer to come up to the flow channel surface passing through the gas diffusion layer. In other words, the produced water remains in the GDL, blocking the pores for about 1 second. During the time that the supplied gas moves on to the triple phase boundary where the electrochemical reaction occurs, the increasing vapor and the condensed water suddenly block the GDL pores and this blockage interferes with mass transfer, causing a temporary performance decrease. Gas convection also decreases because the produced vapor also blocks the gas flow channel surface. Therefore, the undershoot behavior under transient operation is due to the limitation of the gas diffusion time delay. It is concluded that it takes about 1 second for this two phase conflict motion to reach a new steady state. In Figure 2.4-(a), which presents the result for the case of the large effective area fuel cell, continuous voltage loss occurs for 2 seconds after the load change. This result can be interpreted from the same point of view as the transparent fuel cell analysis that considered two-phase mass transfer conflict motion. Moreover, the fact that more undershoot and slow recovery time are obtained under low air stoichiometric ratio condition with both the large-effective-area and general lab-scale small-area fuel cells indicates that undershoot behavior during low load-to-high load change operation occurs due to the delay of gas diffusion into the catalyst layer from the

cathode flooding phenomenon. As the stoichiometric ratio increases, convection and diffusion processes are improved, which yield good dynamic performance of the fuel cell. [97, 98]

This conclusion also coincides with calculation of two-phase mass transport modeling in the GDL by modifying equation (2.1). If liquid water occupy empty pores of the GDL, then gas diffusivity will be interfered, so effective diffusivity of the gas has to be modified as [22]:

$$D_g^{eff} = [\varepsilon(1-s)]^{\tau_d} D_g \quad (2.3)$$

where  $\varepsilon$  is the porosity of the GDL,  $s$  is the liquid water saturation,  $\tau_d$  is the tortuosity of the GDL and  $D_g$  is the gas diffusivity in porous medium. Then, the first time delay is calculated by coupling equation (2.1) and (2.3):

$$\tau_k = \frac{\delta_{GDL}^2}{[\varepsilon(1-s)]^{\tau_d} D_g} \quad (2.4)$$

Since the GDL thickness  $\delta_{GDL}$  is around 0.3 mm, the general diffusivity  $D_g$ , porosity  $\varepsilon$  and tortuosity  $\tau_d$  of porous GDL is  $10^{-5} m^2/s$ , 0.6 and 1.5 respectively, the first time delay  $\tau_k$  is calculated as a saturation of the GDL as shown in Figure 2.8. Above saturation of 0.7, the first time delay exceeds 0.1 seconds and becomes 1 second at saturation of 0.93. Like as experimental results, the first time delay is on the order of 0.1 ~ 1 second in saturated condition which occurs sudden load change operation. In addition, the result that the first time delay increases as saturation increases as shown in Figure 2.8 is also verified with results

that the first time delay increases as flooding intensity increases as shown in references. [97, 98]

Therefore, it is concluded that undershoot occurs at sudden low-load-to-high-load change condition, which has two different time delays. The first stage time delay, which is on the order of 1 second, is due to through-plane gas convection and the diffusion mass transfer limit induced by lowered effective gas diffusivity due to saturation of the liquid water. Also, the time delay of water content recovery of the dehydrated membrane, which is induced by sudden enormous increase of electro-osmotic drag and low back-diffusion water transport at low humidification condition, was on the order of 10 seconds and is described as a second stage delay. The characteristics of the transient response are summarized in Figure 2.9.

Then the question that “Are there any other parameters which affects to the transient response except operating condition?” comes up. The answer is the GDL because it dominates the gas diffusivity and water balance which are main causes of the transient response.

Table 2.1 Experimental conditions for the large effective area fuel cell

Variable	Load change	Stoichiometric ratio		Humidity (%)		Temperature (°C)	Pressure (bar)
		Anode	Cathode	Anode	Cathode		
Stoichiometric ratio	100A → 330A	1.2	2.0	100	100	70	1
		2.4	2.0				
		1.2	4.0				
	330A → 100A	1.0	2.0				
		1.2	1.6				
		1.0	1.6				
Load change	100A → 200A	1.2 2.4 1.2	2.0 2.0 4.0				
Temperature	100A → 200A					30,40,50,60,70	
Humidity	100A → 200A	1.2	2.0	100	100	70	
200A → 100A	50			100			
	100			50			
				50	50		

Table 2.2 Experimental conditions for the transparent fuel cell

Variable	Load change	Stoichiometric ratio		Humidity (%)		Temperature (°C)	Pressure (bar)
		Anode	Cathode	Anode	Cathode		
Stoichiometric ratio	7.5A → 15A	1.2	1.6 2.0 4.0	100	100	40	1
Initial Flooding	7.5A (300s) → 15A	1.2	1.6				
	7.5A (10s) → 15A						

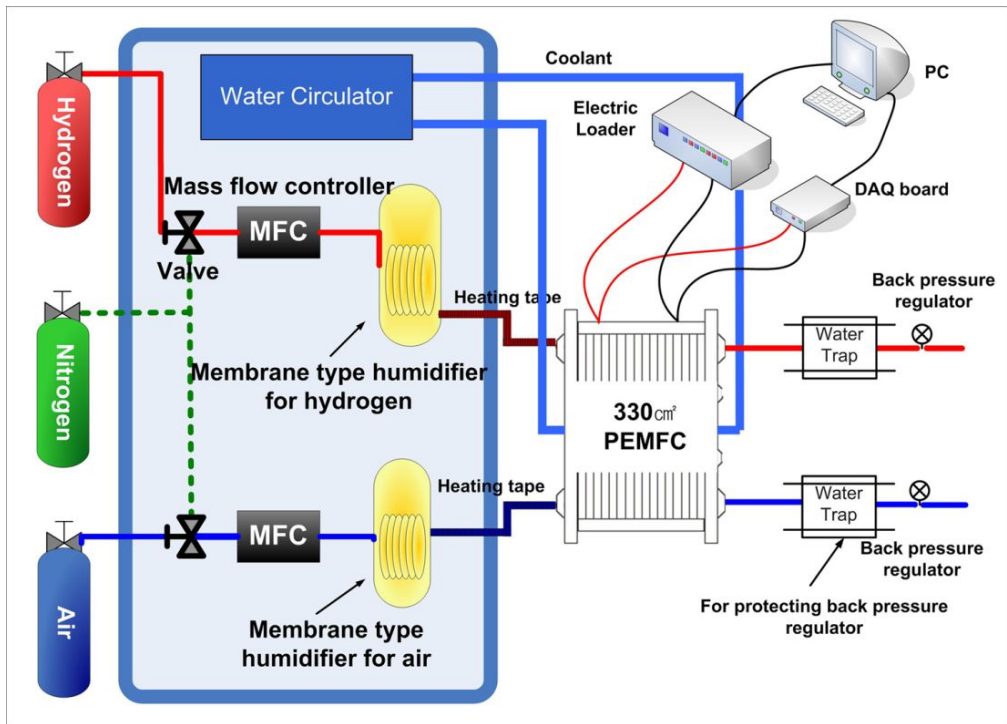


Figure 2.1 Experimental apparatus for testing the 330 cm<sup>2</sup> PEM fuel cell [97, 98]

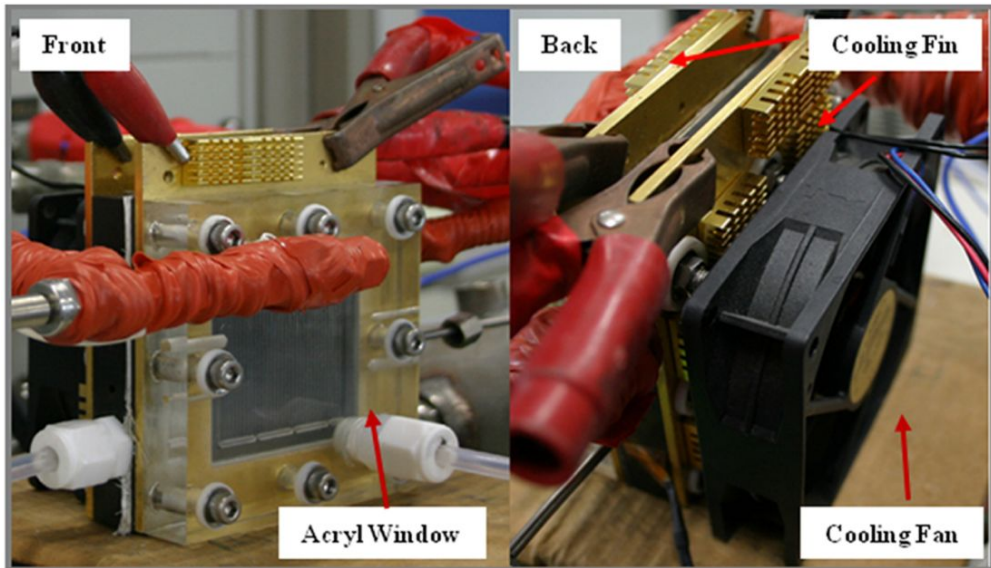


Figure 2.2 Unit 25 cm<sup>2</sup> transparent PEM fuel cell [97, 98]

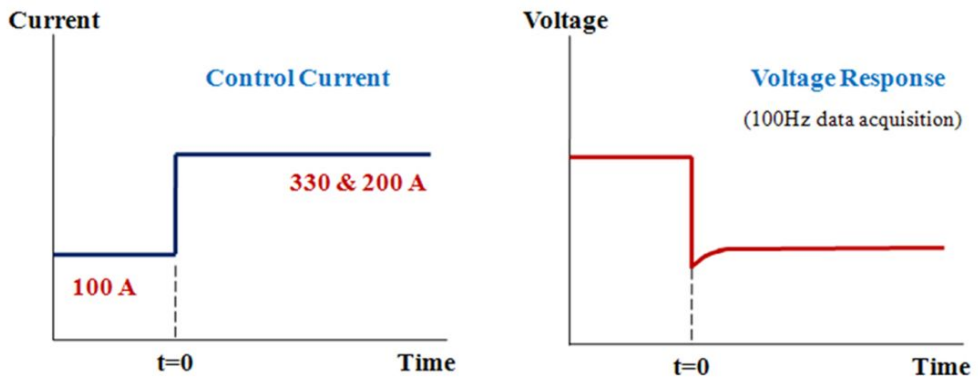
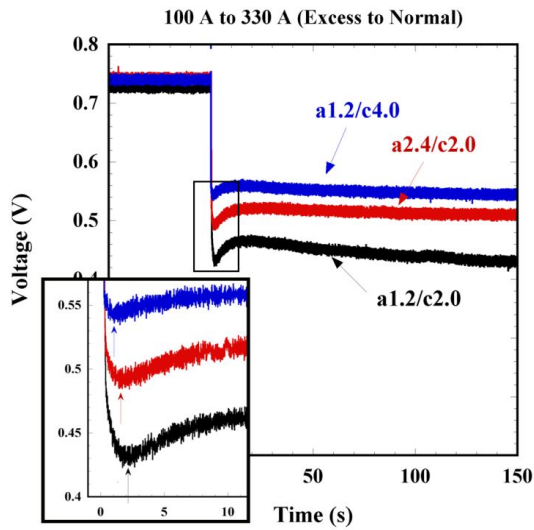
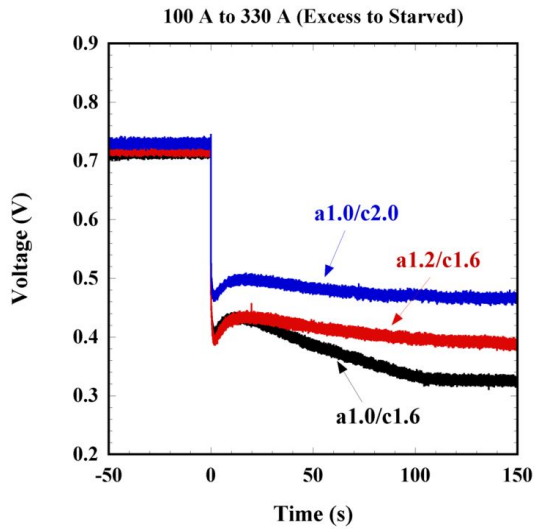


Figure 2.3 Sudden step change of current for large fuel cell (low-load-to-high-load)  
[97, 98]



(a)



(b)

Figure 2.4 The voltage response as current is changed from 100 A to 330 A under (a) excess-to-normal and (b) excess-to-starved stoichiometric conditions, with a temperature of 70 °C, humidity of 100 / 100 % and pressure of 1 bar [97, 98]

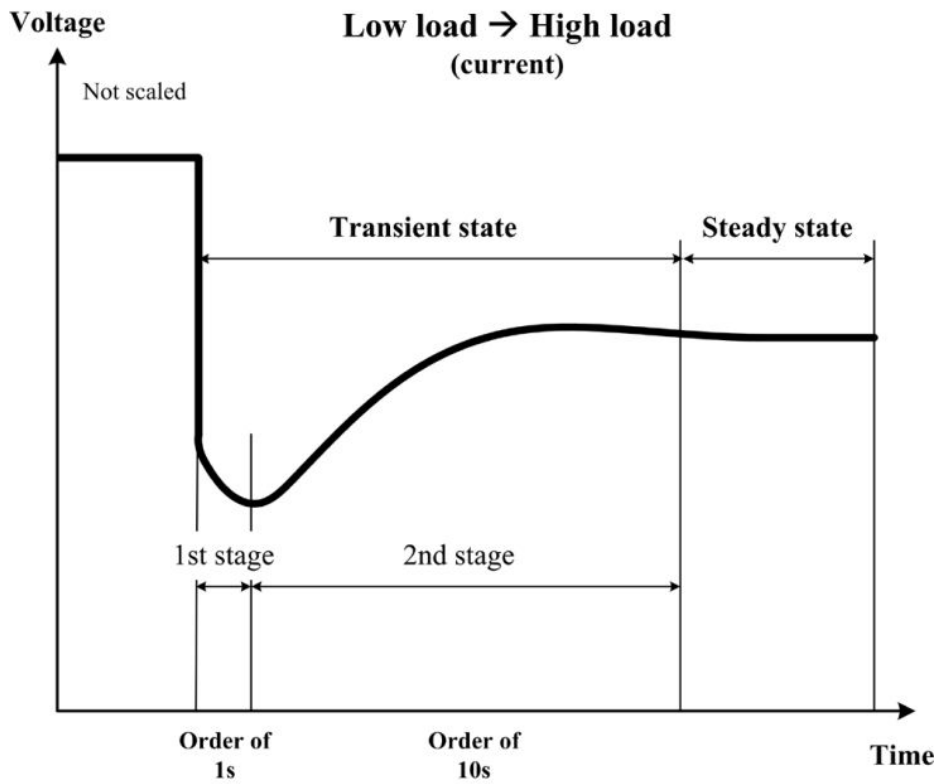


Figure 2.5 The schematic of voltage undershoot behavior during current step change (low-load-to-high-load) [97, 98]

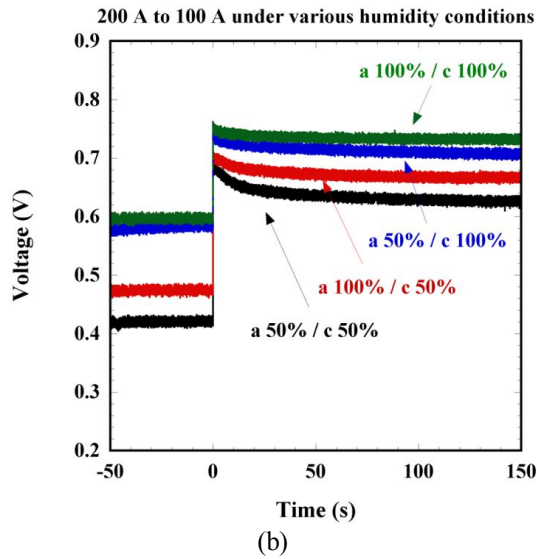
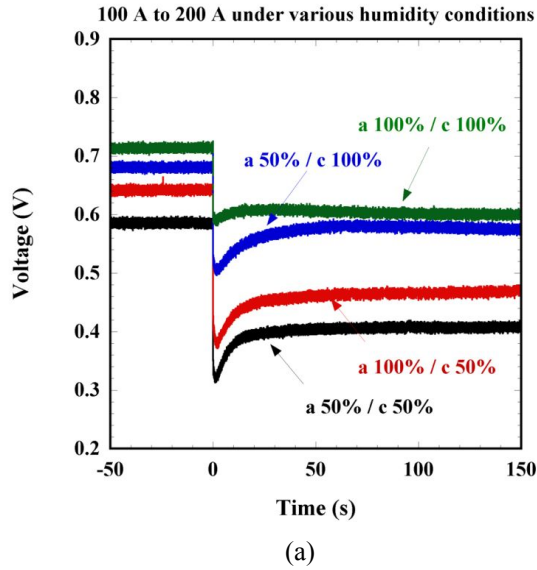


Figure 2.6 The voltage response as current is changed from (a) 100 A to 200 A, (b) 200 A to 100 A under various humidity conditions, temperature of 70 °C, excess-to-normal stoichiometric ratio (1.2/2.0) and pressure of 1 bar [97, 98]

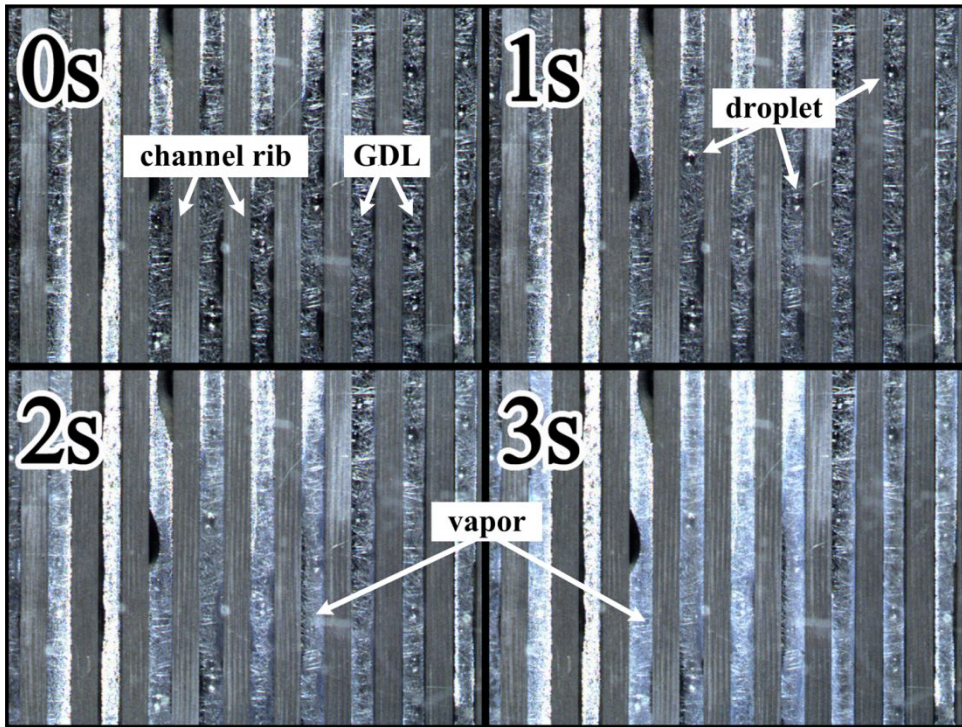


Figure 2.7 Images of cathode channel flooding at cathode stoichiometric ratio of 1.6, temperature of 40 °C, humidity of 100 / 100 %, and pressure of 1 bar [97, 98]

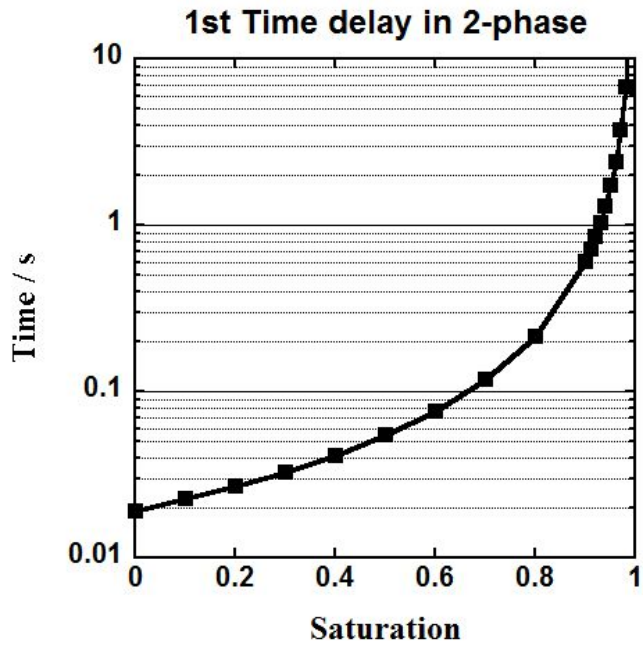


Figure 2.8 The modified 1<sup>st</sup> time delay of undershoot as a saturation level of the GDL

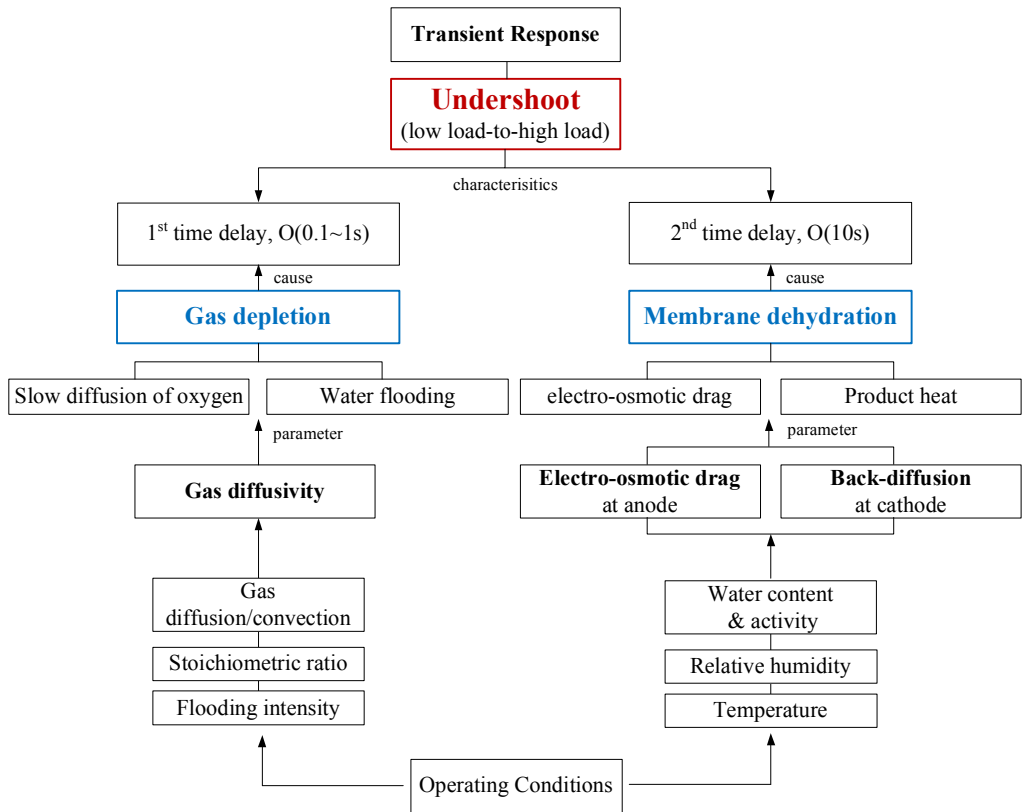


Figure 2.9 Characteristics of transient response of the PEM fuel cell

# **Chapter 3. Transient response of a PEM fuel cell related with structure design of the gas diffusion layer**

## **3.1 Design parameters of GDL structure**

Hydrophobicity of the substrate and the MPL which is represented by weight percent of PTFE have been reached at optimal point through wide researches [42-47]. Recently, studies about designing various types of the GDL have been reported but they overlooked its effects on dynamic behavior of the PEM fuel cell. To enhance cell performance in a wide operation range, investigation of GDL characteristics and effects of its design parameters on transient response of the fuel cell as well as steady-state performance have to be preceded.

Since the GDL has hydrophobic characteristics to remove produced water from the catalyst layer to gas channels, and the membrane conductivity is function of membrane water content, the GDL has trade-off relation depending on humidification conditions which occur diversely in automotive application as shown in Figure 3.1. Dried condition occurs at start-up condition because water production rate is low due to low load and water supply is low due to warm-up time delay of humidifier. Saturated condition is occurred at acceleration and full-load condition due to lots of production of water. In general, at low humidification condition, since water supply from reactant gases is smaller than fully humidification condition, the membrane becomes dehydrated easily, so cell performance decreases. On the other hand, flooding occurs in highly saturated condition, thereby hinders mass transport through the GDL. Then, if more hydrophobic GDL which is controlled by increment of weight percent of PTFE is

used, performance at high load and high humidification condition will increase. However it induces severe dry out of the membrane. In contrast, hydrophilic GDL will induce extreme flooding in high humidification condition instead of performance increase due to enhancement of water holding in low humidification condition. Thus, water holding/removal ability of the GDL is important, and this characteristic can be controlled by amount of PTFE or structure of the GDL.

In this research, effects of design parameters of GDL structure on dynamic behavior of the PEM fuel cell are investigated and basic amount of the PTFE is fixed.

The target samples are summarized in Table 3.1 and schematics are presented in Figure 3.2. As mentioned in introduction chapter, a GDL consists of substrate, MPL and MPL penetration part. Since the GDL can be divided to three parts, design issues have to be investigated respectively to clarify the effects of each design parameter.

At first, design of substrate was varied as shown in Figure 3.2-(a). In the substrate, there are two types of the macro-pores due to structure of the carbon fiber and carbon additives. Where carbon fibers are crossed, carbon fillers and resins are well agglomerated at these intersections, thereby making relatively small macro-pores. On the other hand, along the carbon fibers which are distant from the intersections, large empty spaces are made between carbon fibers. This empty space makes relatively large macro-pores.

To control structure of substrate, the activated carbon fiber (ACF) was adopted. Since the ACF has a large surface area, the carbon fillers, the resins and the PTFEs which are components of the substrate tend to attach around the ACF. Therefore structure of substrate can be varied as changing the amount of the ACF and components. To evaluate role of pore size in the substrate, amount of the ACF was increased to reduce size of relatively large macro-pores. 5 % and 10 % of the

carbon fibers were substituted to the ACF. Areal weight of the substrate was fixed through these samples. Thus, carbon additives were well agglomerated even in large macro-pore regions as portion of the ACF increased, thereby size of large macro-pores decreased, consequently uniform macro pore size distribution is obtained. Notation of ACF-0, ACF-5 and ACF-10 was designated.

And then, to evaluate effect of relatively small macro-pores in the substrate, areal weight was reduced from 80 gsm ( $\text{g}/\text{m}^2$ ) to 70 and 60 gsm, and the ACF was added by 10 % of entire carbon fiber. Thus, relatively small macro-pores are diminished and only relatively large macro-pores exist. Also, when areal weight is decreased, consequently number density of the large macro-pores is increased. Then, role of large macro-pores can be evaluated. Notation of ACF10-80, ACF10-70 and ACF10-60 was designated. ACF10-80 is the same with ACF10 in previous paragraph. All samples have the same MPL.

Second, MPL penetration thickness was varied as shown in Figure 3.2-(b) to investigate effect of MPL penetration part on transient response of the PEM fuel cell. In MPL coating process, it is important design problem how MPL has to penetrate to the substrate to have better mass transport, strength and durability. Thus, three samples which have different MPL penetration thickness (thin/medium/thick) were made. Notation of MP which comes from 'M'PL 'P'enetration was designated to the samples. MP-A has few MPL penetration part, in contrast, MP-C has deep penetration part. The same paper type of substrate was used for all samples.

Third, two MPL design parameters were selected. The first one is MPL slurry density. The carbon black which is a kind of carbon powder is dissolved in solvent to make MPL slurry, and slurry is coated on the top of the substrate so that makes a micro porous layer. In making slurry process, variation of density of the MPL slurry affect pore size of the MPL which can induce different water balance characteristics of the GDL. In addition, capillary pressure profile through the GDL was controlled

by making a double layer which consists of two different MPL slurry densities. Notation of MD which comes from 'M'PL 'D'ensity is designated to the samples. MD-A has dense MPL, in contrast, MD-B has coarse MPL. In special, MD-C has double MPL. The first layer which attached on the substrate is dense, and the second layer which coated on the first MPL layer, thereby contacts with a catalyst layer is coarse expecting enhancement of performance in low humidification condition.

In addition, functional structures were designed inside the MPL. To enhance water holding ability of the GDL, a less hydrophobic layer (LHL) was added in the first MPL which attached on the surface of the substrate. The LHL is made by adding a novel carbon binder in the MPL. The LHL is not a hydrophilic because it has still a contact angle above  $90^\circ$ . A contact angle of the LHL is lower than the second MPL. Notation of MF which comes from 'M'PL 'F'unctional structure was designated to the samples. MF-A has a one normal layer as a reference and MF-B has double layer which LHL is the first layer and normal layer is the second layer. In MF-C, artificial mass transport passage was applied intending enhancement of water removal from the catalyst layer by leading product water moves to path formed inside the MPL. The same paper type of substrate was used for all MPL varied samples.

## 3.2 Experimental setup

### 3.2.1 Fuel cell and test station

As shown in Figure 3.4, a 25 cm<sup>2</sup> unit cell with a parallel serpentine channel (1 mm × 1 mm) flow pattern was used to investigate effects of structural difference of the GDL on the cell performance. The same GORE™ PRIMEA® 5710 MEA catalyst coated membrane was used for each test. The designed GDLs were attached to both side of the anode and cathode. All test protocols including activation just after assembling the cell and purge process were maintained in the same way for every cases. Humidified high purity hydrogen and air were supplied to the cell. The membrane humidifiers were used in both cathode and anode side, and all gas lines were covered by heating lines to maintain exact temperature of reactant gases. Nitrogen gas was used to purge the cell for each experimental case to obtain the same experimental conditions. A cooling fan was also used to remove product heat from the cell. The electric loader was used to control the load changes, and a data acquisition board (USB6009) from National Instrument was used to obtain fast and reliable voltage responses during the load changes.

In addition, to evaluate characteristics of the designed GDL, water permeability was measured as shown in Figure 3.5. A diameter of 5.0 cm of the GDL sample was inserted facing the MPL side is upward into the chamber made of a stainless steel cell. The chamber was 12 cm high and two Teflon tubes (1/2 inch diameter) were connected to the top of the chamber. 0.2 LPM of water was continuously added to the chamber using a pump until water passed through the GDL sample. The change in the hydrostatic head which corresponds to pressure and amount of water drained were recorded every second. Water permeability was evaluated mass flow rate as a function of pressure [54].

The pore distribution of the GDL was also measured using a mercury porosimetry (Autopore IV 9500, Micromeritics USA). Under constant pressure, filled pore diameter by the mercury is inverse proportional to pressure. Thus, pore volume, pore distribution, surface area and so on can be calculated if the volume of filled mercury is measured as an increment of pressure:

$$D = -\left(\frac{1}{P}\right)4\sigma \cos \theta \quad (3.1)$$

where  $D$  is the diameter of pore,  $P$  is the imposed pressure,  $\sigma$  is the surface tension of the mercury and  $\theta$  is the contact angle.

### 3.2.2 Experimental conditions

As shown in Table 3.2, the voltage response was investigated at a sudden load current change from 15 A to 30 A, which corresponds to 0.6 A/cm<sup>2</sup> to 1.2 A/cm<sup>2</sup> in current density, and then from 30 A to 15 A. Voltage data were obtained with a data acquisition rate of 100 Hz. Since it takes about one minute for PEM fuel cell to reach a new steady-state after load change, the cell was operated for three minutes at a prior load before load change. To investigate the effects of the relative humidity, 30 %, 50 % and 100 % RH conditions were used. The SR of the hydrogen and air was fixed at 1.5 and 2.0 respectively for the standard condition. Due to the physical limitation of the response of the gas flow, the flow rates were fixed at the SR of the high load condition. A temperature of 65 °C and a pressure of one bar were maintained for all cases. Steady-state performance and standard deviation of the voltage as a current density were also basically obtained in the same condition.

## 3.3 Experimental results

### 3.3.1 Effects of pore structure of the substrate on transient

#### response of the PEM fuel cell

As shown in Figure 3.6 which is FESEM image and in Figure 3.7 which is pore size distribution by mercury porosimetry, five GDLs were designed by using the ACF. The ACF-0 has size variation of macro pores in the substrate. FESEM image of the ACF-0 shows that there are relatively small macro pores (SMP) and relatively large macro pores (LMP). Figure 3.7-(b) shows pore size distributions of ACF-0/ACF-5/ACF-10. The ACF-0 has the meso-pores around pore diameter of 1  $\mu\text{m}$  and two peaks in macro-pore region. The ACF-0 has the largest macro-pores among all samples. As the ACF is added, the number of SMP decreased because components such as the carbon filler, the resin and the PTFE agglomerate around the ACF as shown in Figure 3.8. Therefore macro pores have uniform pore size such as the ACF-10 shown in Figure 3.6. Pore size distribution of the ACF-10 shows that mean macro-pores exists dominantly in the substrate, thereby macro-pore size variation decreases. Also the size of pore diameter of the largest macro-pores is lowered than that of ACF-0 due to agglomeration of components on the carbon fibers which make a LMP.

As reducing components, the number of macro-pores is increased in ACF10-70 and ACF10-60 as shown in Figures 3.6 and 3.7. As the amount of components decrease, size of the LMP was also increased, thereby uniform macro pore structure was obtained.

At first, the steady-state performances of ACF-0/ACF-5/ACF-10 are shown in Figure 3.9 at an RH of 100 %/50 %/30 %. The performance at low current density

region is same for all three samples, thereby it is concluded that there is no additional electric resistance increment due to the ACF. At fully humidification, there are severe mass transport losses in the ACF-5 and ACF-10. The ACF-5 becomes shut-down after current density of  $0.8 \text{ A/cm}^2$  and the ACF-10 becomes shut-down after  $0.6 \text{ A/cm}^2$ . These results indicate mass transport resistance increases as the pore size variation of the macro-pores decreases. At RH 50 % condition, the ACF-10 also shows severe performance loss, but the ACF-5 shows better performance than that of at RH 100 % condition. At RH 30 % condition, the ACF-10 shows the best performance of three GDLs at low current density region. This result indicates ACF-10 experiences severe saturation in the substrate, thereby large water content of the GDL hydrates the membrane at low humidification condition. However excessive water saturation induces severe flooding when the fuel cell operates at high current density which means water production increases in the cell.

Figure 3.10 shows the transient response of the ACF-0 and ACF-5 at various RH conditions. Since the ACF-10 was shut-down before current density of  $0.6 \text{ A/cm}^2$ , voltage response result could not be obtained. Figure 3.10-(a) shows that voltage of the ACF-5 is cannot maintained just after load change and voltage goes to zero which indicates shut-down after about 60 seconds. In addition, fluctuation of the voltage is larger than that of the ACF-0. It means that there are many blocked pores by liquid water, thereby gas diffusivity decreases in the saturated GDL. On the other hand, the ACF-0 shows that voltage is maintained its steady-state level with slight decrease of performance due to mass transport limits induced by flooding. From this result, it is also concluded that the ACF-5 has larger mass transport loss which indicates that even size distribution of macro-pores induces mass transport resistance in the substrate. This investigation is also observed in Figure 3.10-(b) and (c) which are results at low humidification condition. Since the ACF-5 has high liquid water saturation before load change, thereby backward water concentration gradient exists from the GDL to the membrane which means

enhancement of back-diffusion consequently hydrates dehydrated membrane just after sudden load change. Therefore performance gap between the ACF-0 and the ACF-5 becomes smaller at low humidification condition. However, there are still large liquid water saturation inside the GDL, thereby interferes gas supply to the catalyst layer. Therefore unstable voltage response is still shown at low humidification condition.

Figure 3.11 shows the steady-state performance of ACF10-80/ACF10-70/ACF10-60 with the ACF-0 which areal weight was controlled by changing the amount of components to change the number density of macro-pores. The ACF10-70 shows better performance than the ACF10-80 in high current density region at RH 100 % condition. This indicates that increasing the number density of macro-pores enhances mass transport ability, thereby severe flooding is mitigated. As a result, performance of the ACF10-70 exceeds performance of the ACF-0 at very high current density region. However, the ACF10-70 shows less performance than the ACF-0 at low humidification condition as shown in Figures 3.11-(b) and (c). The polarization curve of the ACF10-70 seems to be shifted downward than the ACF-0 in low humidification condition. This result indicates that ohmic loss of the fuel cell is increased when the ACF10-70 was used because main overpotential in the medium current density region is ohmic loss due to membrane resistance determined by membrane water content, therefore it is concluded that the ACF10-70 has low water holding ability. In addition, the ACF10-60 shows lower performance than the ACF10-70 at both fully and low humidification condition.

Figure 3.12 also shows the performance of ACF10-70 and the ACF10-60 were improved than the ACF10-80. However, they show severe low voltage at RH 30 % condition because they cannot hold water, thereby membrane experience severe dehydration. The ACF10-60 is worse than the ACF10-70. In contrast, at RH 100 % condition, the ACF10-70 and the ACF10-60 shows improved performance than that of the ACF10-80 which induced shut-down after load change. Nevertheless,

performance of the ACF10-70 is lower than that of the ACF-0. It means that increase of number density of the macro-pores induced excessive water removal.

The structure of the substrate severely affects both the steady-state and transient performance of the PEM fuel cell as observed through a series of experimental results. In special, transient response characteristics of the PEM fuel cell was definitely changed in comparison to the results that discussed in Chapter 2. This phenomenon can be explained by water and gas balance through the GDL.

Since performance of the PEM fuel cell dominantly related to water content of the membrane, water supply and water removal process in the PEM fuel cell is dominant factor to the performance. Especially, the transient response at low humidification condition is definitely influenced by water holding/removal ability of the GDL, because harsh membrane dehydration occurs due to sudden large osmotic-drag and product heat. Thus, the mass transport characteristics of the GDL which is attached both sides of the membrane is important to water content of the membrane.

The water flux in Nafion membrane is the calculated by two terms: electro-osmotic drag and back diffusion as below [4]:

$$J_{H_2O} = 2n_{drag}^{SAT} \frac{j}{2F} \frac{\lambda}{22} - \frac{\rho_{dry}}{M_m} D_\lambda(\lambda) \frac{d\lambda}{dz} \quad (3.2)$$

where  $n_{drag}^{SAT}$  is the electro-osmotic drag coefficient,  $j$  is the current density,  $\lambda$  is the water content of the membrane,  $\rho_{dry}$  is the dry membrane density,  $M_m$  is the membrane equivalent weight (EW),  $D_\lambda$  is the diffusivity of water in the membrane, and  $z$  is the direction through the membrane thickness.

Since the membrane experiences severe dehydration at sudden load increases, enhancement of membrane water content recovery is major factor of the transient response. The fact that cathode humidity is dominant to recovery of membrane water content as discussed in the Chapter 2, back diffusion process to the membrane is dominant factor. Thus, as shown in Figure 3.13, if the cathode GDL holds water so that water concentration at the cathode interface between the GDL and catalyst layer (CL) is high, the amount and the velocity of the back diffusion increases toward the membrane. Besides, if the anode GDL also holds water, then high water concentration at anode interface between the GDL and CL mitigates dehydration of anode side of the membrane induced by large electro-osmotic drag. Thus, it is concluded that water content of the membrane is determined by mass transport flux from the GDL if other conditions are the same.

Then, mass transport flux from the GDL corresponds to water holding/removal ability of the GDL is determined by water transport through the GDL.

Two-phase liquid water transport in the GDL [22] is driven by the capillary pressure which is calculated by:

$$P_c = \tau \cos(\theta_c) \left( \frac{\varepsilon}{K} \right)^{1/2} J(s) \quad (3.3)$$

$$J(s) = 1.417s - 2.120s^2 + 1.263s^3 \quad (3.4)$$

$$s = \begin{cases} 0 & C_w \leq C_{sat} \\ \frac{C_w - C_{sat}}{\rho^{(l)} / M_w - C_{sat}} & C_w > C_{sat} \end{cases} \quad (3.5)$$

$$\rho = s\rho^{(l)} + (1-s)\rho^{(g)} \quad (3.6)$$

where  $P_c$  is the capillary pressure,  $\tau$  is the surface tension,  $\theta_c$  is the contact angle,  $\varepsilon$  is the porosity,  $K$  is the permeability,  $J(s)$  is the Leverett J-function,  $s$  is the liquid water saturation,  $\rho^{(l)}$  is the density of liquid water,  $\rho^{(g)}$  is the density of gas,  $M_w$  is the molar mass of the water,  $C_w$  is the water concentration, and  $C_{sat}$  is the saturation concentration of the water.

Then the water flux in the GDL is calculated by:

$$\vec{j}^{(l)} = \frac{\lambda^{(l)}\lambda^{(g)}}{\nu} K \left[ \nabla P_c + (\rho^{(l)} - \rho^{(g)})\vec{g} \right] \quad (3.7)$$

where  $\lambda^{(l),(a)}$  are relative mobilities of individual phases and  $\nu$  is the dynamic viscosity. Consequently, water transport in the GDL is dominantly determined by capillary pressure gradient,  $\nabla P_c$ .

$\nabla P_c$  can be divided into capillary pressure gradient of the MPL and the substrate through the GDL as shown in Figure 3.14. Since the GDL has different size of pores and structures along the through plane direction, capillary pressure is different. When the water is produced in the catalyst layer (CL), capillary pressure  $P_{C,CL}$  increases until the capillary pressure of the interface between the CL and the MPL,  $P_{C,CL-MPL}$ . When  $P_{C,CL}$  exceeds  $P_{C,CL-MPL}$ , the water is capillary driven to the MPL with the pressure of  $P_{C,CL-MPL}$ . Since  $P_{C,MPL-Sub}$  is lower than

$P_{C,CL-MPL}$  because the substrate's macro-pore size is 100 times larger than the micro-pores in the MPL, capillary pressure gradient,  $\nabla P_{C,MPL}$  occurs toward the substrate.

$$\nabla P_{C,MPL} = \frac{P_{C,CL-MPL} - P_{C,MPL-Sub}}{\delta_{MPL}} \quad (3.8)$$

Thus, water moves to substrate by the force of  $\nabla P_{C,MPL}$ . Then, water moves to the gas channel (GC) by the force of  $\nabla P_{C,Substrate}$ .

$$\nabla P_{C,Substrate} = \frac{P_{C,MPL-Sub} - P_{C,Sub-GC}}{\delta_{substrate}} \quad (3.9)$$

Thus, structure design determines capillary pressure of each component, capillary pressure gradient determines water transport mechanism of the GDL.

Back to performance results due to substrate design, schematic of formation of capillary pressure in the substrate is presented in Figure 3.15. Since all operating conditions were the same for all samples, capillary pressure of CL-MPL interface is the same for all cases. In this schematic, for better understanding, simple number which corresponds to the capillary pressure of each position is introduced. Since the substrate's macro-pore size is 100 times larger than the micro-pores in the MPL, capillary pressure gradient,  $P_{C,CL-MPL}$  is designated to 100. And all thickness of the layers are assumed as the same value.

In case of the ACF-0, there are relatively large macro pore (LMP) and relatively small pore (SMP) in the GDL. Figure 3.16 shows difference of capillary

pressure between LMP and SMP. Since the SMP is surrounded by hydrophobic carbonized resin and PTFE, hydrophobicity is higher than the LMP. In addition, since pore diameter of SMP is smaller than the LMP, capillary pressure of the SMP is higher than that of the LMP. Thus, the capillary pressure gradient from the MPL to the SMP is lower than that of LMP. Therefore water passage is possible to be formed to the LMP as shown in Figure 3.15. If it is assumed that  $P_{C,SMP}$  is 10,  $P_{C,LMP}$  is 1 and  $P_{C,MPL-Sub}$  is 50, then assuming thickness of layer as 1,  $\nabla P_{C,MPL}$  becomes 50 and  $\nabla P_{C,Substrate}$  becomes 49. Consequently product water is removed by the pressure gradient force of 50 and 49 at the MPL and the substrate respectively.

In case of the ACF-5, as mentioned before, components are well agglomerated on the ACF, the number of the SMP decreases and the size of LMP decreases. It means that blocked spaces increases, thereby saturation of liquid water increases. Also increase of capillary pressure in the LMP induces lower capillary pressure gradient to the substrate, also induces increase of saturation in the substrate due to lowered driving force. Saturated water increases capillary pressure of the substrate like that back pressure is imposed. Then  $\nabla P_{C,MPL}$  decreases as well as  $\nabla P_{C,Substrate}$  as shown in Figure 3.15. This phenomenon is repeated and worsened as time goes by after load change, then accumulated water induces severe flooding as presented in Figure 3.10.

In case of the ACF-10, enormous back pressure effect imposed to substrate, thereby extreme flooding occurs even in medium current density region as reported in Figure 3.9-(a).

On the other hand, in case of the ACF10-60 and the ACF10-70, coarse substrate extremely lowered capillary pressure of the substrate, thereby increase of  $\nabla P_{C,Substrate}$  induces extreme water removal. Therefore the GDL cannot maintain hydration of the membrane, hence severe voltage drop occurs and voltage cannot be recovered after load change at low humidification condition as presented in Figure 3.12-(b). In addition, extreme water removal ability of the these samples induce low water content of the membrane even though in fully humidification condition, however it prevents water flooding, thereby voltage response is maintained after load change in contrast to the voltage of the ACF-0 as presented in Figure 3.12-(a).

Through these experimental results and analysis using concept of capillary pressure gradient in the GDL, it is concluded that existence of pore size variation in the macro-pores is important in substrate design for wide range of operation because the LMP works as a water removal passage due to high capillary pressure gradient and the SMP works as a water holding passage due to low capillary pressure gradient.

Then, to determine size range of small macro pore, an extreme case is assumed. Although, the meso-pores in the MPL penetration part are dehydrated and macro-pores in substrate are fully saturated, water has to be driven to substrate by positive  $\nabla P_C$ . Thus, an inequality has to be satisfied.

$$P_{C,meso} \Big|_{dehydrated} > P_{C,macro} \Big|_{saturated} \quad (3.10)$$

Then, revisiting equations (3.3) and (3.4), and permeability,  $K$  is substituted to pore diameter,  $d_p$  [99],

$$K = \frac{\varepsilon^3 \left( \frac{1}{4} \sqrt{\frac{4}{\pi}} d_p \right)^2}{96(1-\varepsilon)^2} \quad (3.11)$$

Then, capillary pressure is expressed as like:

$$P_c = \tau \cos(\theta_c) \left( C \frac{(1-\varepsilon)}{\varepsilon d_p} \right) J(s) \quad (3.12)$$

Eventually, an inequality is obtained like below:

$$\cos(\theta_c) \left( C \frac{(1-\varepsilon)}{\varepsilon d_p} \right) J(s) \Big|_{meso} > \cos(\theta_c) \left( C \frac{(1-\varepsilon)}{\varepsilon d_p} \right) J(s) \Big|_{macro} \quad (3.13)$$

, and with general constant value,  $\varepsilon_{meso} = 0.5$ ,  $\theta_{C,meso} = 150^\circ$ ,

$J(s) \Big|_{meso} = 0.1$ ,  $\varepsilon_{macro} = 0.6$ ,  $\theta_{C,macro} = 140^\circ$ ,  $J(s) \Big|_{macro} = 0.5$ , size of the macro-pore has to be at least 3 times larger than size of the meso-pores.

$$\frac{d_{p,macro}}{d_{p,meso}} > 3 \quad (3.14)$$

### 3.3.2 Effects of MPL penetration thickness on transient response of the PEM fuel cell

Three samples that have different MPL penetration thicknesses as shown in Figure 3.17 are made. Same substrate (or expressed as a GDBL: Gas diffusion backing layer) which has a thickness of 280  $\mu\text{m}$  was used for all samples. Thickness of 110  $\mu\text{m}$  MPL was coated on the substrate. MP-A has little penetration part. MP-B was controlled to have medium penetration thickness of 100  $\mu\text{m}$  and MP-C has thick penetration into the substrate. About 50 % of substrate was filled with MPL.

Figure 3.18 shows pore distribution of three samples. There are three peaks describing three parts of the GDL. Less than 1  $\mu\text{m}$ , micro-pore peak was observed. Since three samples have the same MPL, peaks coincide with each other for all samples. Meso-pore and macro-pore shows structural difference between three samples. The meso-pore was more developed in case of MP-C than MP-A due to thicker MPL penetration part.

Figure 3.19 shows start-of-penetration pressure and relation between pressure drop and water flow rate. Although, three samples have the same MPL which means that they have same contact angle and pore size, values of start-of-penetration pressure were different due to difference of water transport characteristics induced by structure. MP-A has the highest penetration pressure of 16181 Pa and MP-C has the lowest pressure of 15004 Pa. In addition, slope of graph ( $\frac{\Delta\dot{m}}{\Delta P}$ ) which means ratio of water flow rate over pressure also indicates water transport characteristics. Slope of MP-A is lower than the slope of MP-C which means MP-A needs larger driving force than MP-C to push the same amount of water through the GDL.

Figure 3.20 shows voltage response at an RH of 100 % after load change as a time. Since the MP-B shows medium performance between MP-A and MP-C, results of MP-A and MP-C are shown in the paper. Figure 3.20-(b) is for standard flow rate condition which stoichiometric ratio of cathode is 2.0. Figure 3.20-(a) is

for starved condition which is SR of 1.6. Figure 3.20-(c) is for excess condition, SR of 4.0. MP-A and MP-C shows different shape of transient response. In case of MP-A, voltage decreases continuously after load change as shown in Figures 3.20-(a) and (b). It means low water management ability of MP-A induces flooding. As SR of cathode decreases, continuous voltage loss after load change increases. At excess air condition, the effect of large flow rates exceed loss due to flooding, thus performance of MP-A and MP-C is similar.

Figure 3.21 shows voltage response at an RH of 50 %. Like as results of Figure 3.20, MP-C shows better performance than MP-A in all SR conditions. In special, Figure 3.20-(c) shows that the 2<sup>nd</sup> time delay of MP-A, which is due to membrane hydration recovery, is longer than that of MP-C although gas supply is enough at SR of 4.0 condition. This information indicates MP-A has demerit in water holding ability at low humidification condition.

In addition, voltage instability was estimated by standard deviation of voltage as current density increased. Large standard deviation means voltage is unstable due to mass transfer loss. Figure 3.22 shows that voltage instability of MP-C is lower than MP-A at fully humidification condition. This result also supports that water removal of MP-C is better than MP-A in fully humidification condition.

Through a series of experimental results, it is concluded that MP-C which has a deep MPL penetration thickness is better than MP-A which has a thin thickness for both high and low humidification conditions. This result can be also analyzed by capillary pressure gradient through the both GDL as shown in Figure 3.23.

Since the MPL slurry is the same for both samples,  $P_{C,CL-MPL}$  is the same for both samples. The capillary pressure of 100 is assumed to  $P_{C,CL-MPL}$  because pore size of micro-pore is about 100 times larger than that of macro-pore. Since MP-A

has a little MPL penetration part, small portion of substrate is filled with a MPL. This interface consequently has a low capillary pressure due to large pore size of the substrate. Thus, 10 of  $P_{C,MPL-Sub}$  is assumed. On the other hand, MP-C's MPL penetrates to the substrate, thereby makes meso-pores which is smaller than macro-pores. Thus,  $P_{C,MPL-Sub}$  increases, 50 of  $P_{C,MPL-Sub}$  is assumed by averaging 1 and 100. The  $P_{C,Sub-GC}$  is assumed as the same value of 1 for both samples. In conclusion,  $P_{C,MPL-Sub}$  is varied due to MPL penetration part. Then, considering thickness,  $\nabla P_{C,MPL}$  of MP-A is 90 and of MP-C is 25. Consequently  $\nabla P_{C,Substrate}$  of MP-A becomes 4.5 and of MP-C becomes 49. This capillary pressure gradient in the substrate drives water to move to the gas channel. Since  $\nabla P_{C,MPL}$  of MP-A is large, almost entire water rapidly penetrates to the substrate, and then, water meets the large pores in the substrate. Since lower  $\nabla P_{C,Substrate}$  of MP-A drives water to move to the gas channel in longer distance than MP-C, water tends to be accumulated in the substrate. As time goes by, continuously accumulated water increases capillary pressure of the substrate, it works as a back pressure which makes an additional pressure to the MPL. In addition, accumulated water in the substrate works as a long capillary pressure barrier between the MPL and the substrate, so more mass transport resistance occurs. This investigation is supported by study of Kang [100], which also presented numerical investigation of this phenomenon by using a pore-network model that a thin MPL increases saturation of the entrance of the substrate. Therefore, the penetration pressure and mass transport resistance of MP-A is higher than that of MP-C as also shown in water permeability results in Figure 3.19. Thereby, in case of MP-A at sudden load increase and at high

humidification condition, water flooding occurs in the substrate, thereby deteriorated mass transport causes lower transient response than MP-C as reported in Figure 3.20.

Although the substrate is saturated in case of MP-A, the MPL is relatively dehydrated due to large capillary pressure gradient through the MPL. This phenomenon affects performance loss in low humidification condition because water concentration of the MPL is low, thereby water flux is small to the catalyst layer and the membrane. Accumulated water in the substrate is hard to move back to the MPL because large capillary pressure barrier exist at the interface. In contrast, MP-C which has a thick MPL penetration part shows balanced capillary pressure gradient through the GDL water removal is better at high humidification. In addition, water exists in the MPL due to relatively low driving force determined by pressure gap between inlet and outlet of the MPL. Thus, water can be accumulated in the MPL at low humidification condition, which induces increase of back diffusion from the GDL to the catalyst layer and the membrane, thereby induces performance enhancement.

This capillary pressure analysis is presented following chapters to explain causes of experimental results of the transient response characteristic in the diverse MPL structure.

### **3.3.3 Effects of MPL density on transient response of the PEM fuel**

#### **cell**

Three samples which have different MPL density structure were made as shown in Figure 3.24. Since MD-A has a dense MPL, there is few cracks on the surface of the MPL. In contrast, MD-B and MD-C have a coarse MPL, there is lots of cracks on the surface of the MPL.

Figure 3.25 shows the transient response of MD-A/MD-B/MD-C at various RH conditions. Figure 3.25-(a) shows MD-A which has a double dense MPL is the best at fully humidification condition. Figure 3.25-(b) shows MD-B which has a double coarse MPL is the worst at low humidification condition. Figure 3.25-(c) shows MD-C which has a dense-coarse MPL is the best at extremely low humidification condition. These results indicate MD-A has the best water removal ability as well as proper water holding ability, MD-B is worse both for high and low humidification conditions, and MD-C has the best water holding ability as well as proper water removal ability. MPL density varied double layer show quite difference in the transient response at both high and low humidification conditions. In special, MD-C shows distinguishing performance in wide range of humidification condition. MD-C shows very short the 2<sup>nd</sup> time delay of 5 seconds and small amount of undershoot at RH 30 % although this is an extremely low humidification, which is compared to 15 seconds of MD-A and more delayed time of MD-B and large amount of undershoot.

In Chapter 2, it was concluded that undershoot characteristic is due to gas depletion and membrane dehydration, and these parameters are influenced by operating conditions. In special, revisiting equation of (2.2),

$$\tau_m = \frac{(\rho\delta_m\Delta\lambda)/EW}{I/2F} \quad (3.10)$$

the order of 10 seconds 2<sup>nd</sup> time delay which corresponds to time delay of water content recovery of the dehydrated membrane, which is induced by sudden enormous increase of electro-osmotic drag and low back-diffusion water transport at low humidification condition, was enhanced in MD-C. This means that high water concentration of the both the anode and the cathode GDLs compensate dehydration of the membrane as discussed with equation (3.2) and Figure 3.13, and eventually reduces 2<sup>nd</sup> time delay of undershoot by reducing required membrane water content,  $\Delta\lambda$  as presented in equation (3.10).

It is concluded that water holding GDL reduces membrane water content recovery time, thereby fast transient response is obtained despite of low humidification conditions like as a MD-C.

This observation also can be analyzed capillary pressure gradient through the GDL as shown in Figure 3.26. MD-A has smooth capillary pressure gradient from the MPL inlet to the gas channel outlet. As discussed in case of MP-C this capillary pressure gradient is good for both high and low humidification condition. In case of MD-B, the coarse density MPL decreases capillary pressure due to enlarged pore size in the MPL. Therefore the initial capillary pressure,  $P_{C,CL-MPL}$  is lowered than MD-A. Capillary pressure of 80 is assumed. In addition,  $P_{C,MPL-Sub}$  is also lowered due to combination of the coarse MPL with the substrate as a pressure of 40. Then, considering a thickness,  $\nabla P_{C,MPL}$  becomes 20 and  $\nabla P_{C,Substrate}$  becomes 39 in MD-B. Since driving force through the substrate of MD-B is lower than that of MD-A, MD-B has higher water saturation in the substrate, thereby more mass transport resistance exists, which induces performance decrease at high humidification condition. This analysis is shown in transient response results of Figure 3.25-(a).

On the other hand, since  $P_{C,CL-MPL}$  of MD-B is lowered to 80, water is accumulated under the MPL until  $P_{C,CL}$  reaches 80 which is compared to 100 of MD-A. This means that water concentration under the MPL decreases, thereby back diffusion water flux to the membrane decreases. Consequently, performance decreases at low humidification condition as observed in Figure 3.25-(b).

In contrast, in case of MD-C reverse capillary pressure gradient is formed due to combination of the dense 1<sup>st</sup> layer and the coarse 2<sup>nd</sup> layer.  $P_{C,CL-MPL}$  of MD-C is same like as MD-B. Since upper layer has high capillary pressure of 90, reverse capillary pressure of 10 is imposed through the coarse 2<sup>nd</sup> layer. This induces water accumulation in the coarse 2<sup>nd</sup> layer. When capillary pressure of the coarse 2<sup>nd</sup> layer exceeds  $P_{C,Coarse-Dense}$ , then water moves to next dense layer. Consequently, water exists in the coarse 1<sup>st</sup> layer which induces better water flux to the CL and membrane, thereby enhances performance of the fuel cell even at extremely low humidification condition as observed in Figure 3.25-(c). However, this accumulation brings a little side effect which is mass transport resistance at high humidification condition as observed in Figure 3.25-(a).

Through this chapter, it is figured out that the density of the MPL affects the transient response of the PEM fuel cell. In special, a high capillary pressure of the MPL surface induces good performance at both high and low humidification conditions because capillary pressure gradient increases and water concentration under the MPL increases. However, if extremely dense MPL is used, gas permeability decreases and too large amount of water accumulation under the MPL causes CL flooding. Therefore optimal design of MPL density is required.

### **3.3.4 Effects of functional structure of the MPL on transient response of the PEM fuel cell**

MF-B has a less hydrophobic layer (LHL) in the 1<sup>st</sup> layer MPL and MF-C has a LHL and an artificial pore path which is made by adding relatively large size of carbon particles as shown in Figure 3.27.

Figure 3.28 shows the transient response of MF-A/MF-B/MF-C at RH of 100 % and 50 % conditions. Figure 3.28-(a) shows MF-A which has a normal MPL is the best at fully humidification condition. Figure 3.28-(b) shows MF-B which has a LHL in the 1<sup>st</sup> layer is the best and MF-C is better than MF-A at low humidification condition. These results indicate MF-B and MF-C have better water holding ability than MF-A as an effect of LHL, however, water holding induces slight flooding as observed in Figure 3.28-(a). In special, MF-B has the best water holding ability so that the 2<sup>nd</sup> time delay is very short as 5 seconds. On the other hand, MF-C shows less water holding ability than MF-B because of pore path through the MPL. Although MF-C has low water holding ability, performance at fully humidification condition is also lower than that of MF-B. This observation indicates that pore path in the MPL is disadvantage at both high and low humidification conditions, in contrast to simple idea that if there is a pass to transport, water can easily move along the path.

This observation also can be analyzed capillary pressure gradient through the GDL as shown in Figure 3.29. MF-A has smooth capillary pressure gradient from the MPL inlet to the gas channel outlet. In case of MF-B, the LHL decreases capillary pressure due to decreased hydrophobicity in the MPL like a coarse MPL discussed in previous chapter. Although the initial capillary pressure,  $P_{C,CL-MPL}$  is same with MF-A,  $P_{C,HL-LHL}$  and  $P_{C,LHL-Substrate}$  are changed due to low capillary pressure of LHL. 20% decrease of pressure is assumed. Capillary pressure of 90  $(=(100+80)/2)$  and 40  $(=(1+80)/2)$  can be calculated for  $P_{C,HL-LHL}$  and  $P_{C,LHL-Substrate}$  respectively by averaging pressure of each layer. Then  $\nabla P_{C,MPL}$  becomes 30  $(=(10+50)/2)$  and  $\nabla P_{C,Substrate}$  becomes 39 in MF-B. Since driving

force through the substrate of MF-B is lower than that of MF-A, MF-B has higher water saturation in the substrate, thereby more mass transport resistance exists which induces performance decrease at high humidification condition. However, the difference of  $\nabla P_{C,Substrate}$  is slight, small amount of mass transport resistance occurs in MF-B. This analysis is shown in transient response results of Figure 3.25-(a).

On the other hand, since  $\nabla P_{C,HL}$  is small, momentum of water removal decreases in the hydrophobic layer (HL), which means water is possible to exist in the HL. In addition, lowered  $\nabla P_{C,Substrate}$  induces water saturation in the substrate, thereby accumulated water in the substrate also reduces driving momentum of the LHL by working as a back pressure. This means that it is possible for water to exist in the LHL. In contrast to case of MP-A discussed in previous chapter which has a severe back pressure due to thin MPL penetration, the LHL is the MPL penetration part by itself which meets with the substrate. Therefore, water can move back from the substrate to the LHL. These two effects induce enhancement of water holding at low humidification.

In case of MF-C, the pore path, whose diameter is larger than that of micropores, decreases capillary pressure of HL and LHL. It means the LHL has the much lower capillary pressure. Eventually, combination of LHL and pore path induces low  $\nabla P_{C,Substrate}$  of 29. This increases more water saturation as explained in case of MF-B, thereby water removal ability is deteriorated eventually causes performance decrease at fully humidification condition as presented in Figure 3.28-(a).

In addition, due to decreased  $P_{C,CL-MPL}$  of 80, water is accumulated under the MPL until  $P_{C,CL}$  reaches 80 which is compared to 100 of MF-B. This means that water concentration under the MPL decreases, thereby back diffusion water flux to the membrane decreases. Consequently, performance decreases although it has more water saturation in the substrate at low humidification condition as observed in Figure 3.28-(b).

Through this chapter, it is figured out that the functional structure of the MPL affect capillary pressure gradient through the GDL, eventually affect the transient response of the PEM fuel cell. In special, a LHL of the MPL induces better water holding ability of the GDL. However, a pore path is unfavorable because it reduces capillary pressure of the MPL. This observation coincides with the fact that the MPL was developed to have large capillary pressure on the surface and to have large capillary pressure gradient through the GDL.

Through a series of experimental results of various GDLs which have diverse structures in each part, it is concluded that capillary pressure gradient can be designed by diverse methods in the substrate, the MPL penetration part and the MPL, and diverse capillary pressure gradients determines water flux through the GDL. Water flux affects water removal at high humidification condition, and affects electro-osmotic drag compensation and additional back diffusion from the GDL to the membrane. Then, transient response is affected by gas and water balance in the GDL and the membrane.

Figure 3.30 shows suggested design of pore size distribution of the GDL from consideration of this chapter. In the micro-pore size region, reverse-multiple MPL showed best performance for wide humidity conditions due to extremely enhanced water holding ability at low humidity condition. In the meso-pore size region, thick MPL penetration was better for both high and low humidity conditions. In macro-

pore region, large pore size variation has to be obtained because relatively large macro-pore plays a role as water removal passage and small macro-pore works as water holding passage. However, small macro-pore has to be at least 3 times larger than meso-pore. In case of large macro-pore, size of pore cannot be unlimitedly increased because mechanical strength has to be considered as a part of fuel cell. Finally, combination of the MPL and the substrate is also important.

After investigating design of capillary pressure through the GDL, then the question that “How the transient response is changed when the characteristics of the GDL is changed due to long term operation?” comes up. The solution is the change of capillary pressure gradient of the GDL because it dominates the gas diffusivity and water balance which are main causes of the transient response.

Table 3.1 Target boundary of the GDLs

Structure	Design Parameter	Target Point	Notation
Substrate	Uniform pore size distribution	ACF 0 %, 80gsm	ACF-0
		ACF 5 %, 80gsm	ACF-5
		ACF 10 %, 80 gsm	ACF-10
	Number density of uniform pores	ACF 10 %, 80 gsm	ACF10-80
		ACF 10 %, 70 gsm	ACF10-70
		ACF 10 %, 60 gsm	ACF10-60
<u>M</u> PL Penetration	<u>P</u> enetration Thickness	Shallow	MP-A
		Medium	MP-B
		Deep	MP-C
<u>M</u> PL	Slurry <u>D</u> ensity	Dense	MD-A
		Coarse	MD-B
		Double layer	MD-C
	<u>F</u> unctional Structure	Reference	MF-A
		Less hydrophobic layer	MF-B
		LHL + Pore path	MF-C

Table 3.2 Experimental cases.

Case	Current step	Relative Humidity (%)	Stoichiometric Ratio (H <sub>2</sub> /Air)	Temperature (°C)
1-1	15 A to 30 A	100	1.5/2.0	65
1-2	(0.6 to 1.2	50		
1-3	A/cm <sup>2</sup> )	30		
2-1	30 A to 15 A	100	1.5/2.0	
2-2	(1.2 to 0.6	50		
2-3	A/cm <sup>2</sup> )	30		

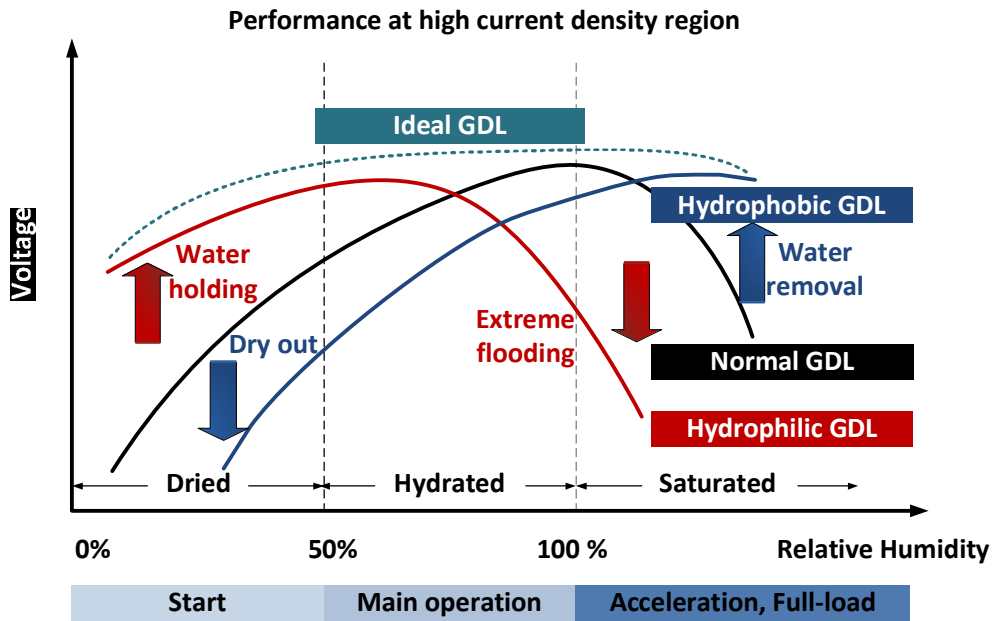
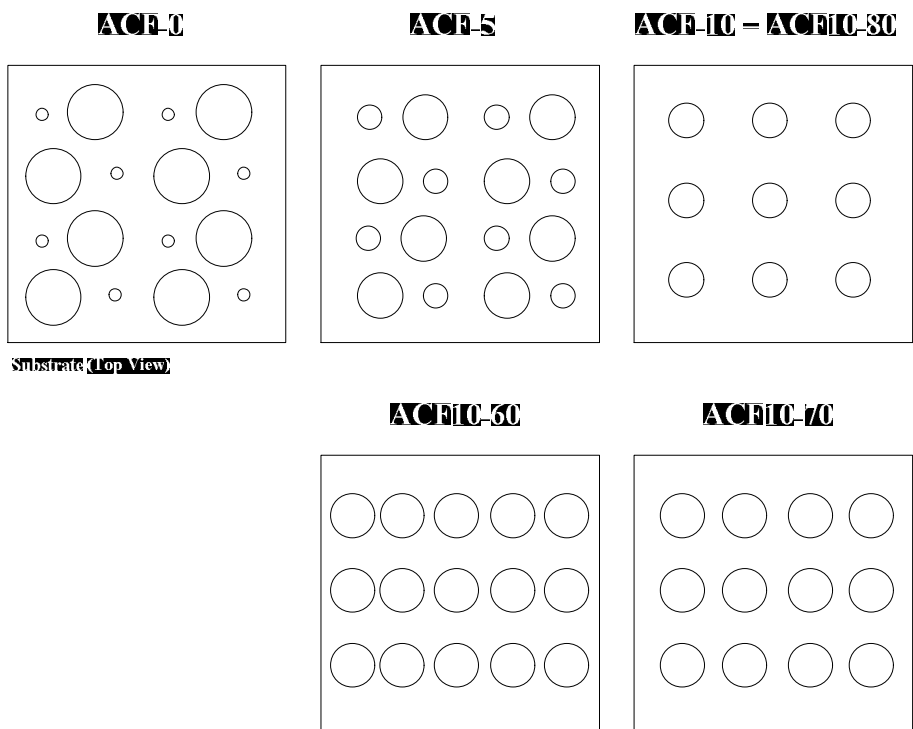
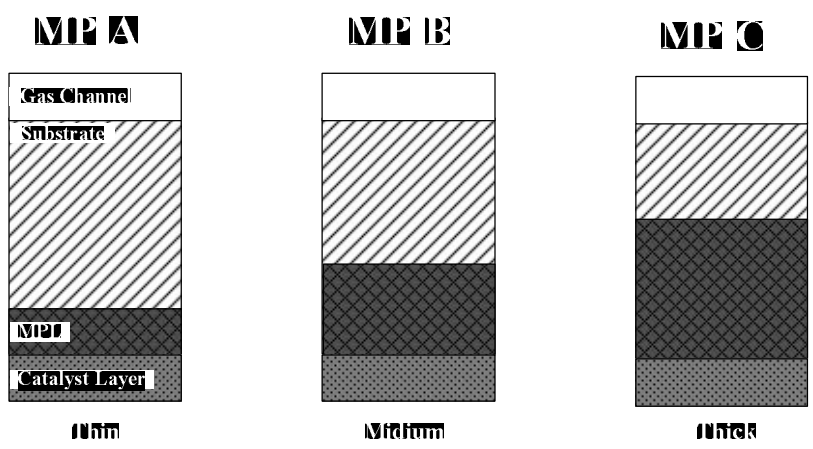


Figure 3.1 Trade-off relation of the GDL as a humidification conditions



(a)



(b)

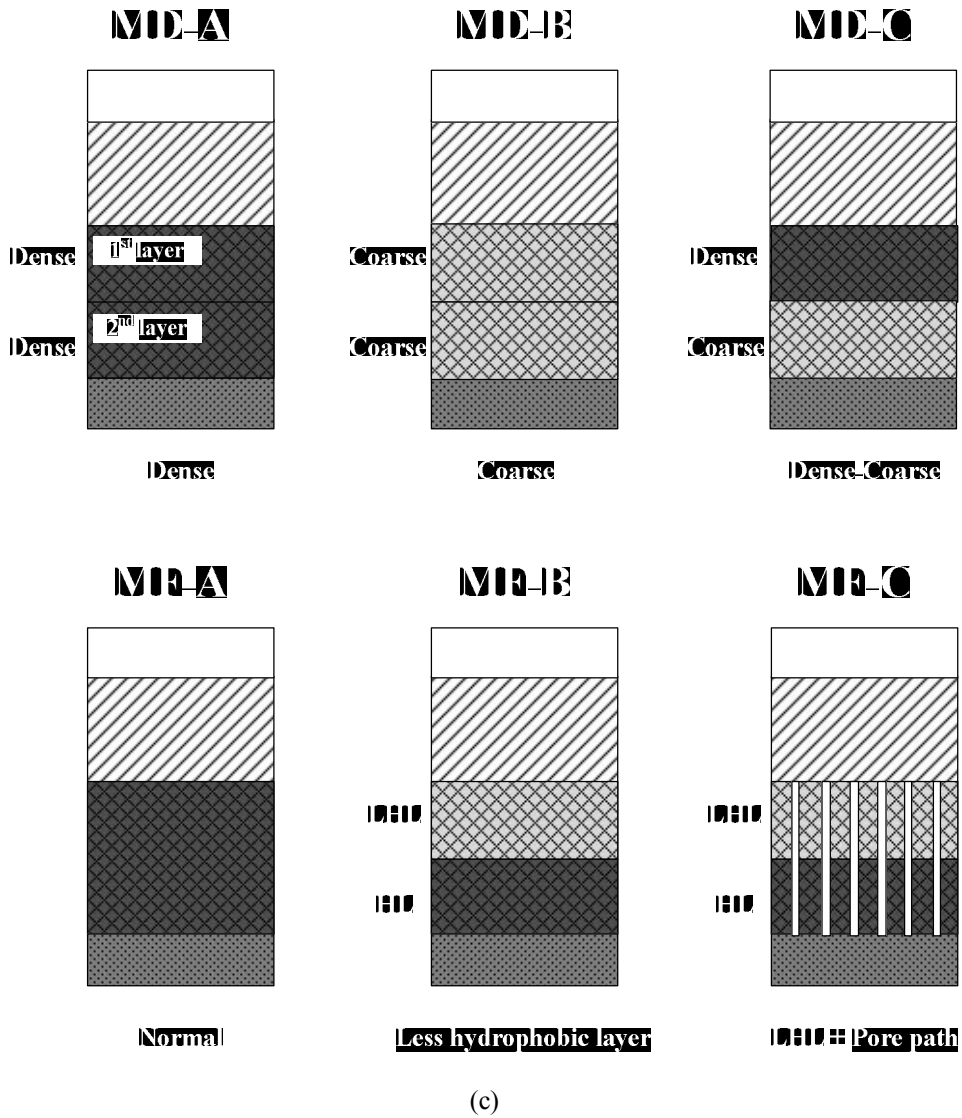


Figure 3.2 Schematic of target boundary of the GDL as design parameters in (a) the substrate, (b) the MPL penetration part and (c) the MPL

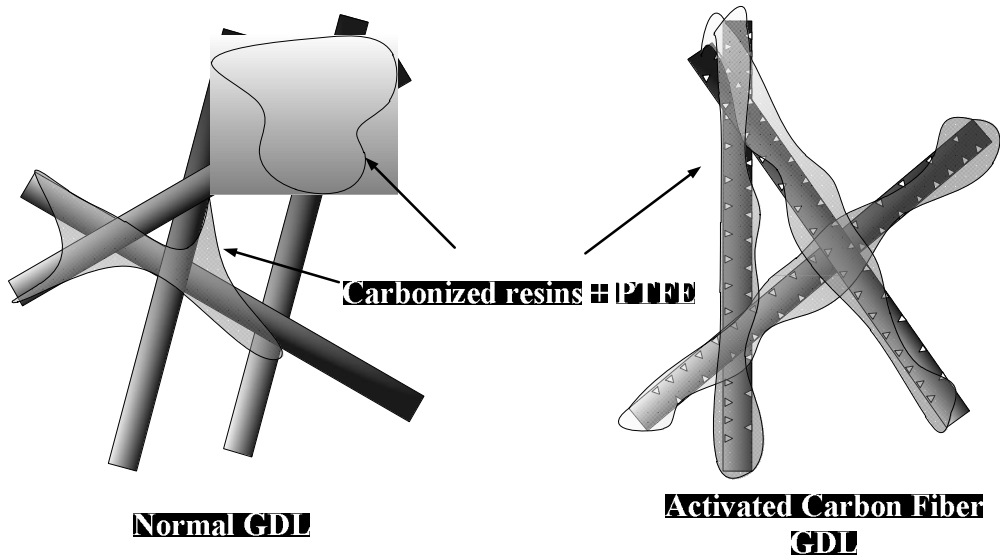


Figure 3.3 The activated carbon fiber (ACF)

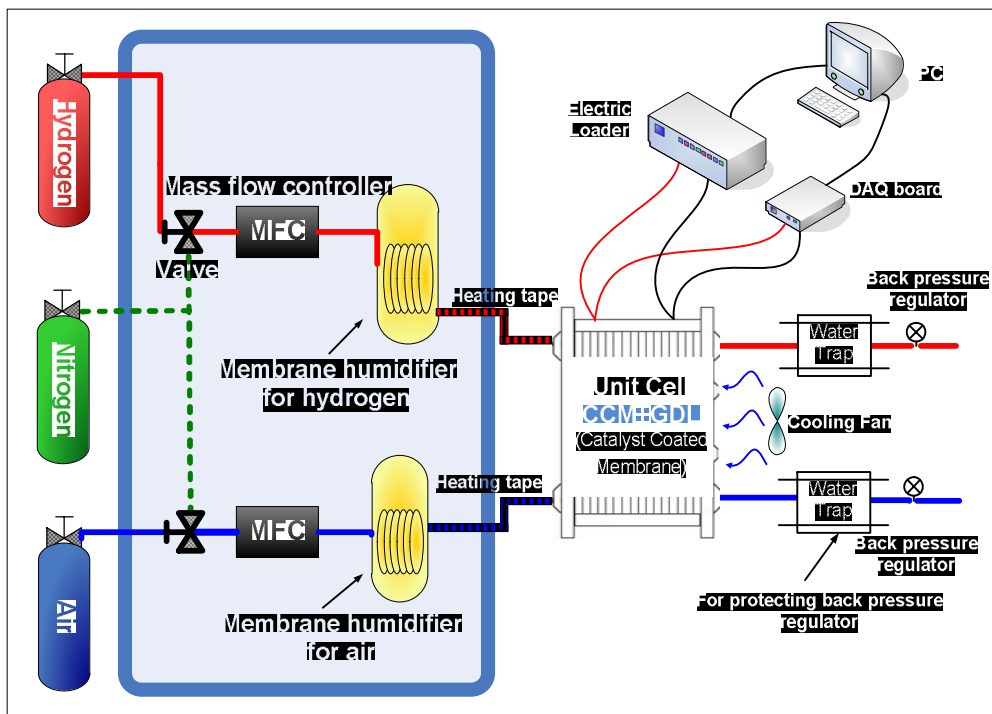


Figure 3.4 Experimental apparatus for testing various types of the GDL

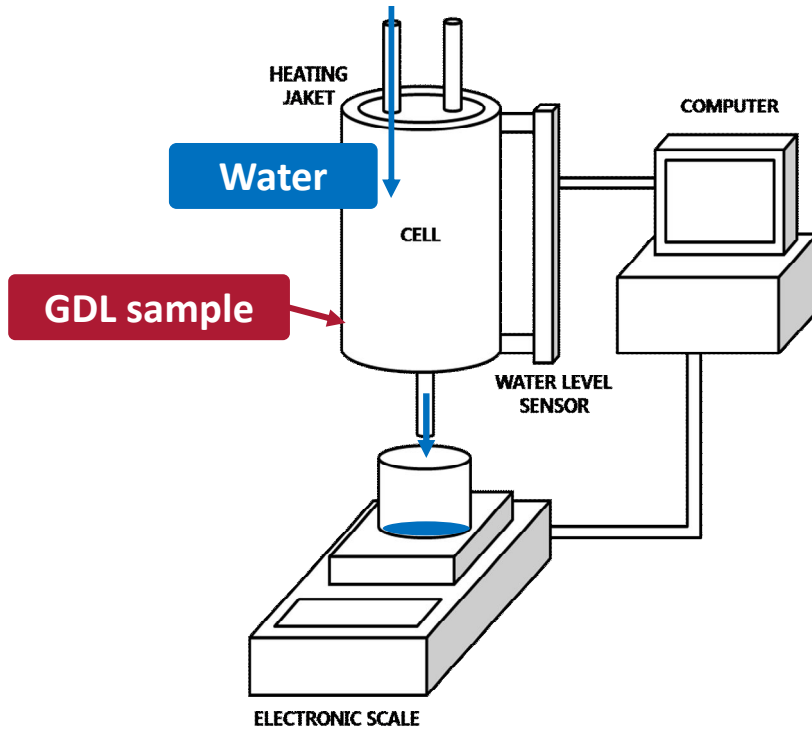


Figure 3.5 Experimental apparatus for measuring water permeability of the GDL [53]

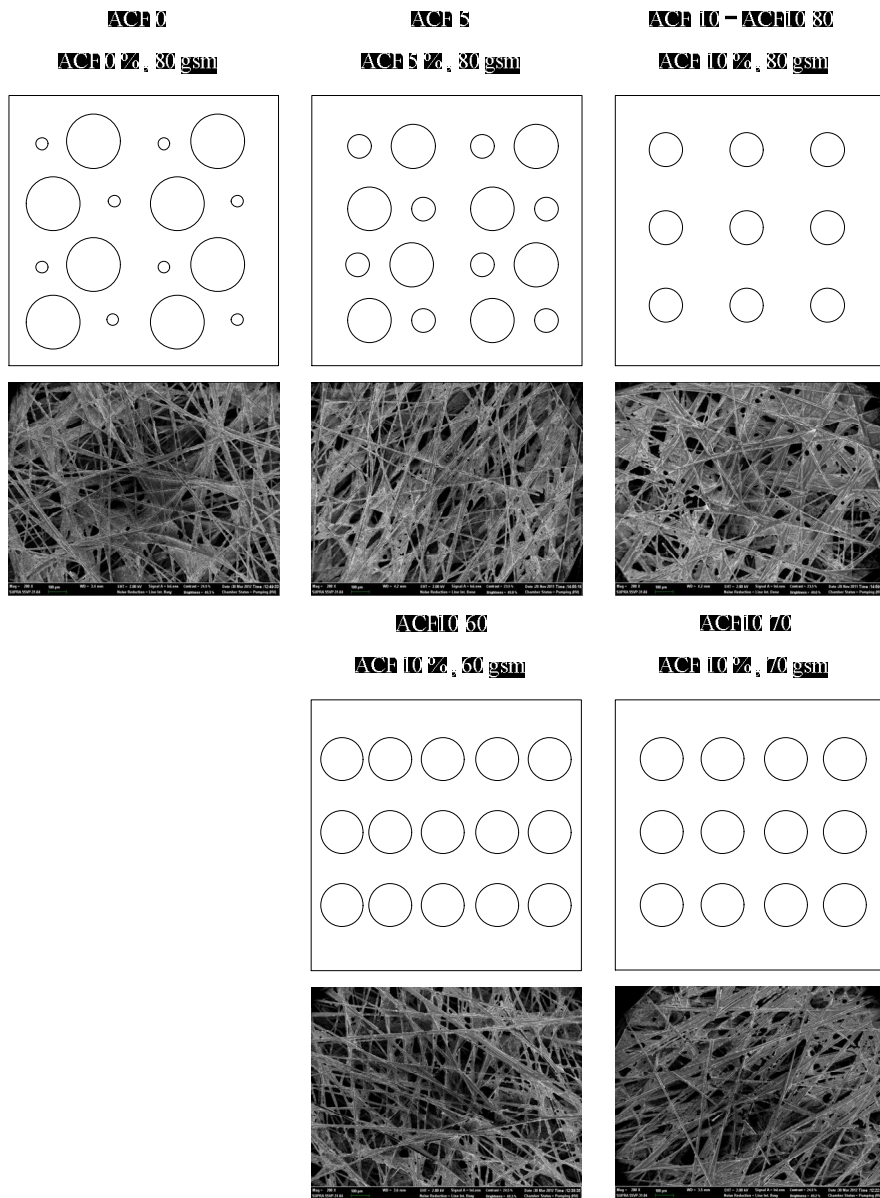
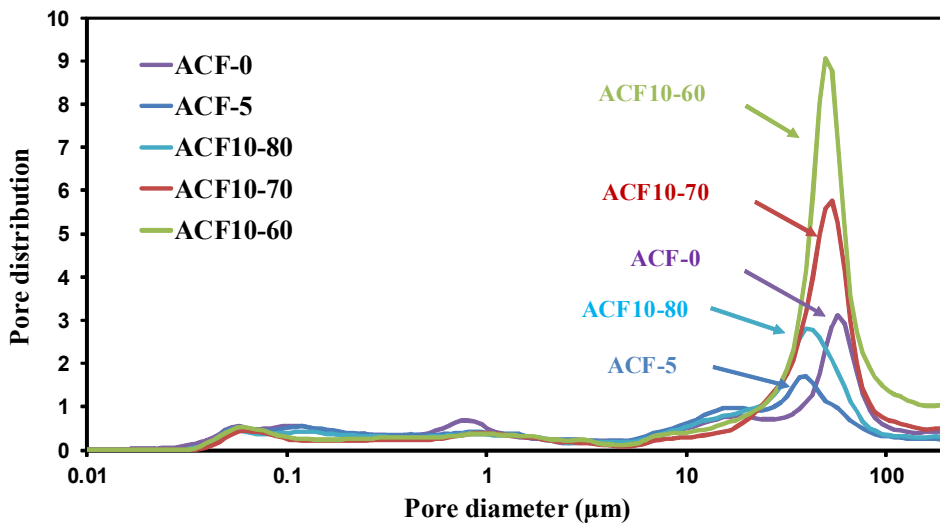
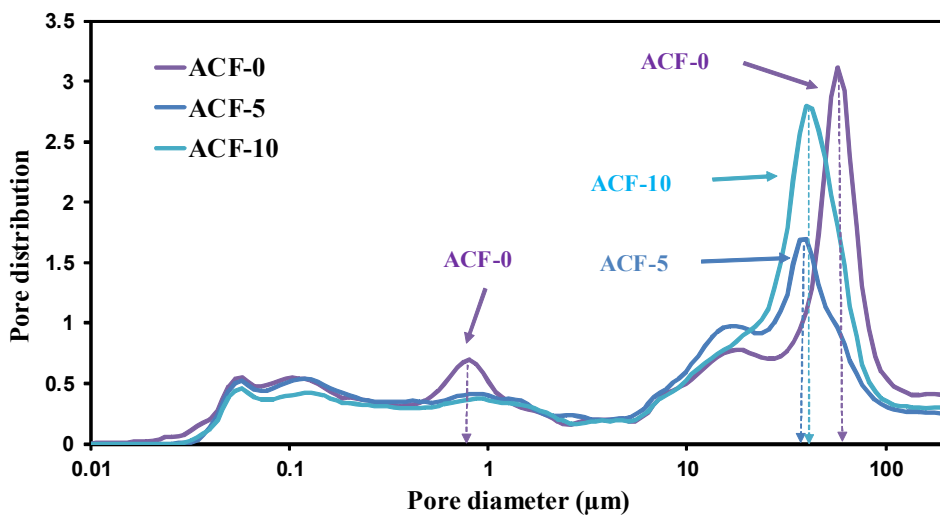


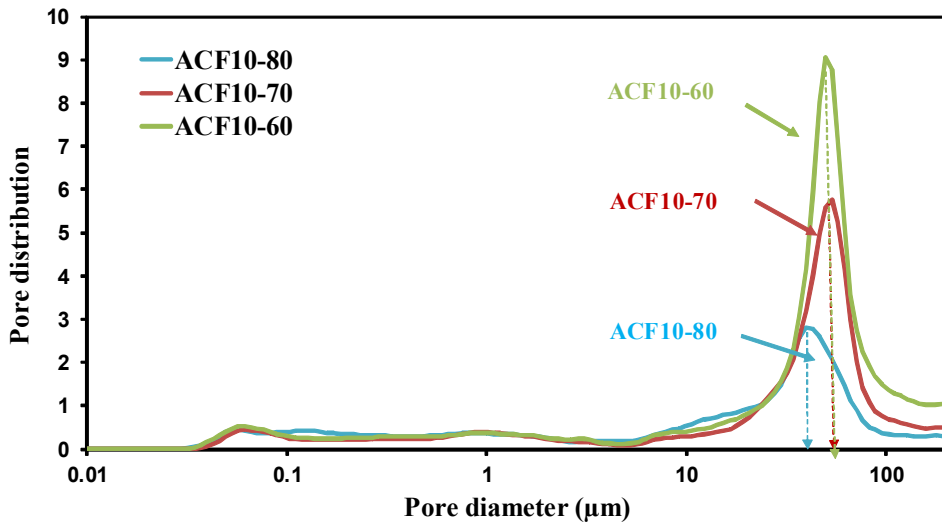
Figure 3.6 Schematic and FESEM images (200 x magnifications) of GDL which have different pore structure in the substrate



(a)



(b)



(c)

Figure 3.7 Pore size distributions of substrate designed samples: (a) all samples, (b) ACF-0/ACF-5/ACF-10, and (c) ACF10-80/ACF10-70/ACF10-60

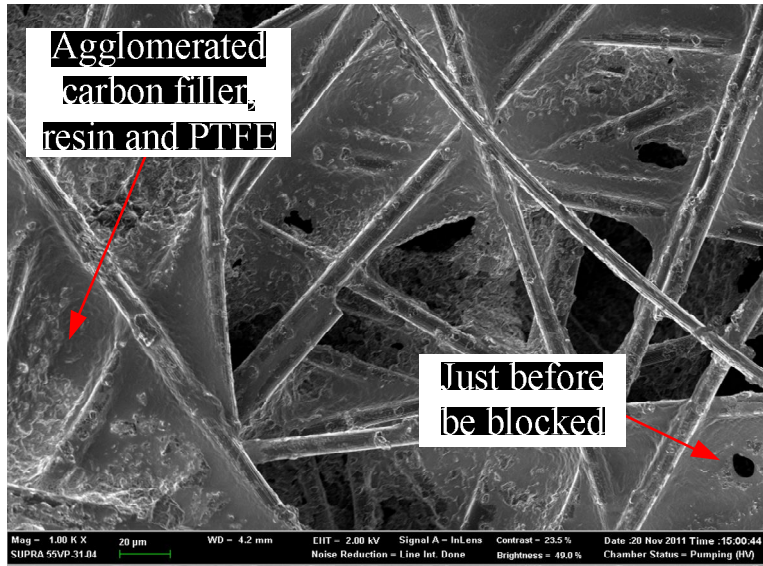


Figure 3.8 FESEM image of the ACF-10 (1000 x magnifications)

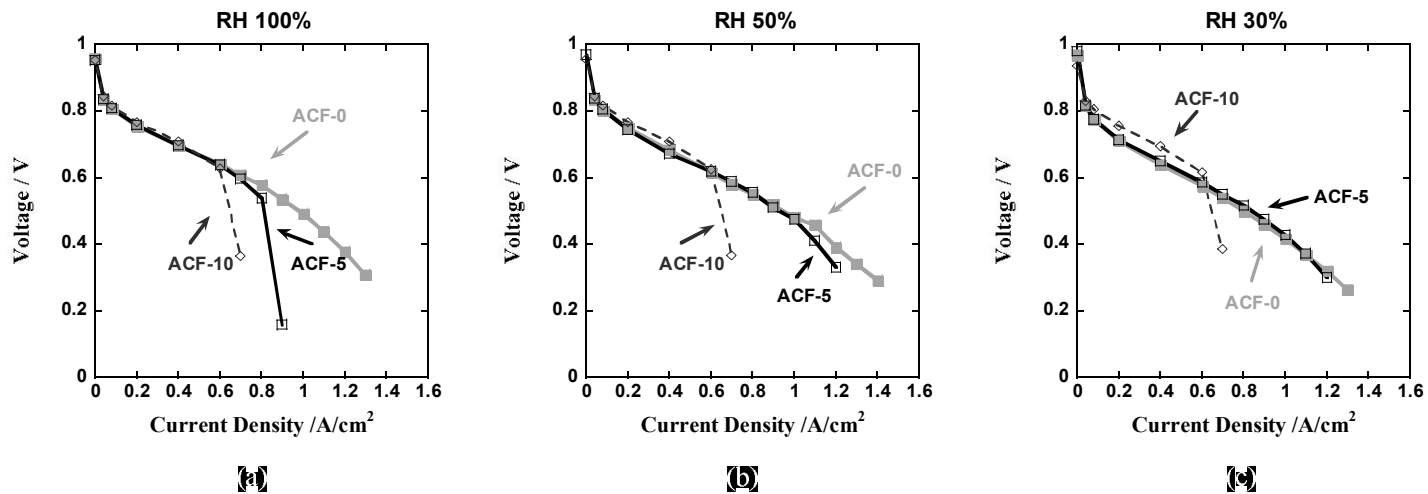


Figure 3.9 The steady-state performance of the ACF-0/ACF-5/ACF-10 at (a) an RH of 100 %, (b) 50 %, and (c) 30 %

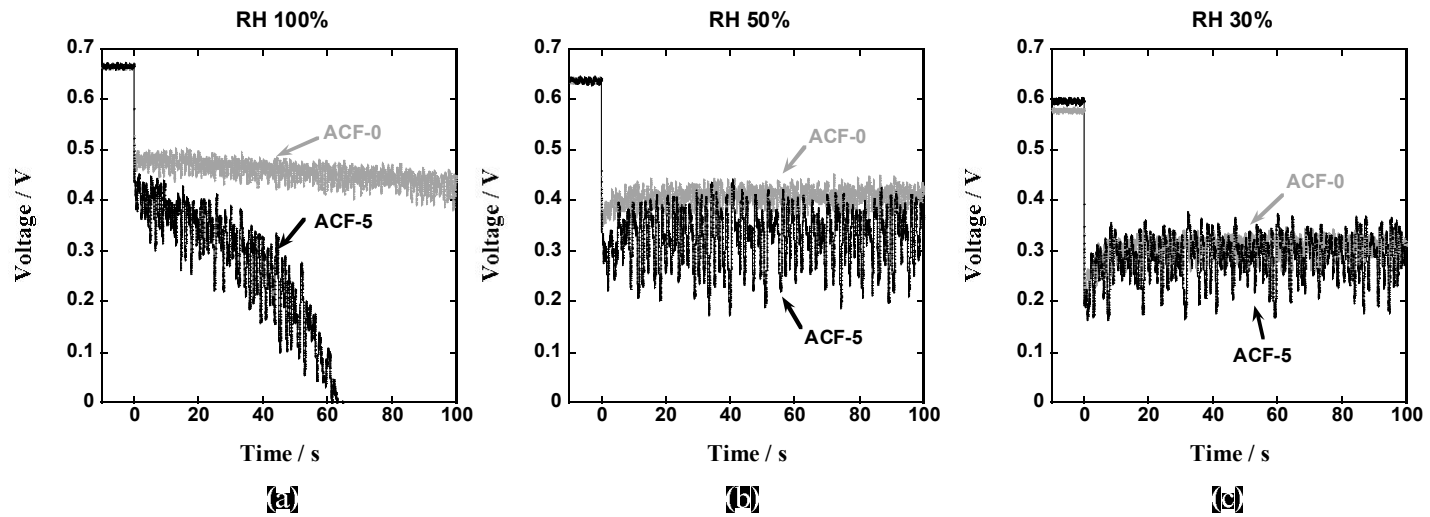


Figure 3.10 The voltage response of the ACF-0/ACF-5 as the current was changed from 15 A to 30 A at (a) an RH of 100 %, (b) 50 %, and (c) 30 %

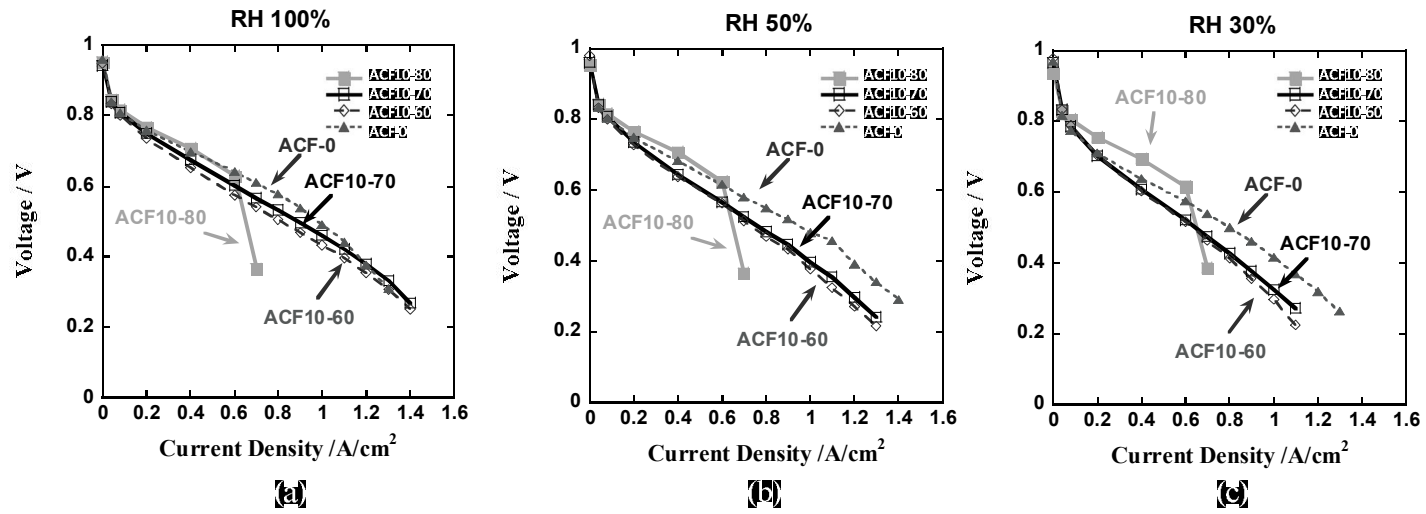


Figure 3.11 The steady-state performance of the ACF10-80/ACF10-70/ACF10-60/ACF-0 at (a) an RH of 100 %, (b) 50 %, and (c) 30 %

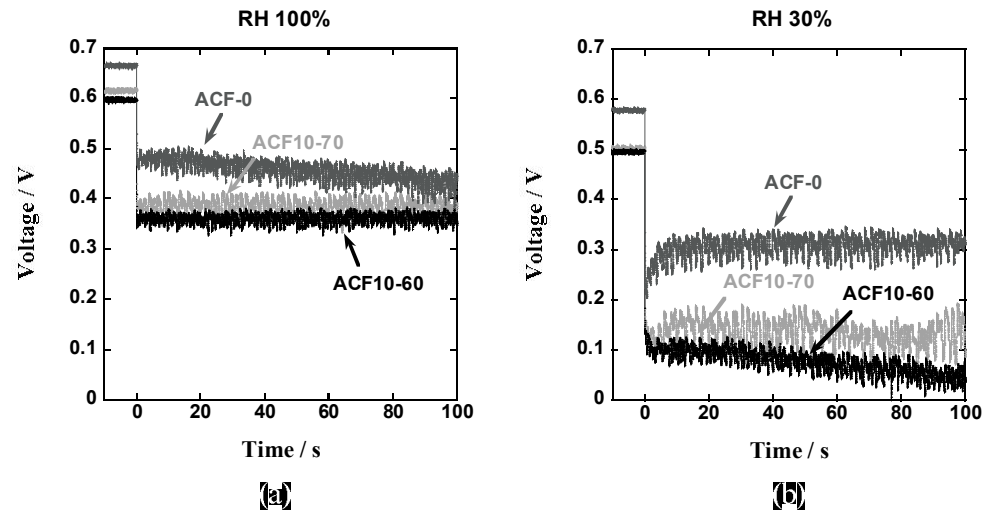
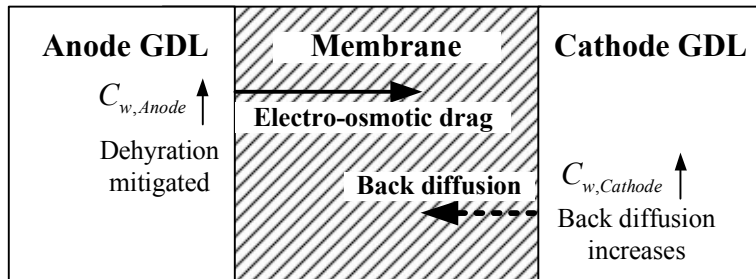
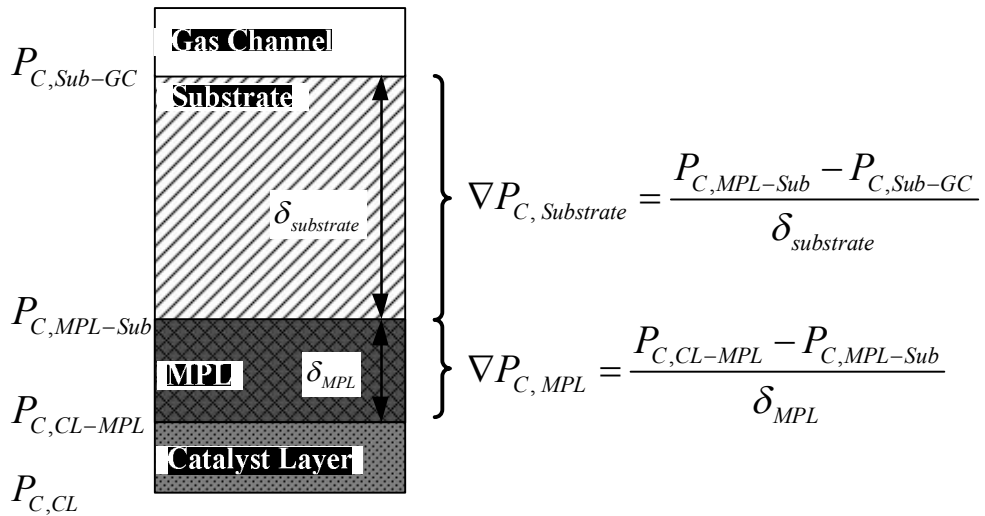


Figure 3.12 The voltage response of the ACF10-70/ACF10-60/ACF-0 as the current was changed from 15 A to 30 A at (a) an RH of 100 %, and (b) 30 %



$$J_{H_2O} = \underbrace{2n_{drag}^{SAT} \frac{j}{2F} \frac{\lambda}{22}}_{\text{Electro-osmotic drag}} - \underbrace{\frac{\rho_{dry}}{M_m} D_{\lambda}(\lambda) \frac{d\lambda}{dz}}_{\text{Back diffusion}}$$

Figure 3.13 Schematic of relation between GDL water content and membrane hydration



*if  $P_{C,CL} \geq P_{C,CL-MPL}$*

*then water moves to the MPL with  $P_{C,CL-MPL}$*

*if  $P_{C,CL} \leq P_{C,CL-MPL}$*

*then water is accumulated until  $P_{C,CL} = P_{C,CL-MPL}$*

Figure 3.14 Capillary pressure gradient through the GDL

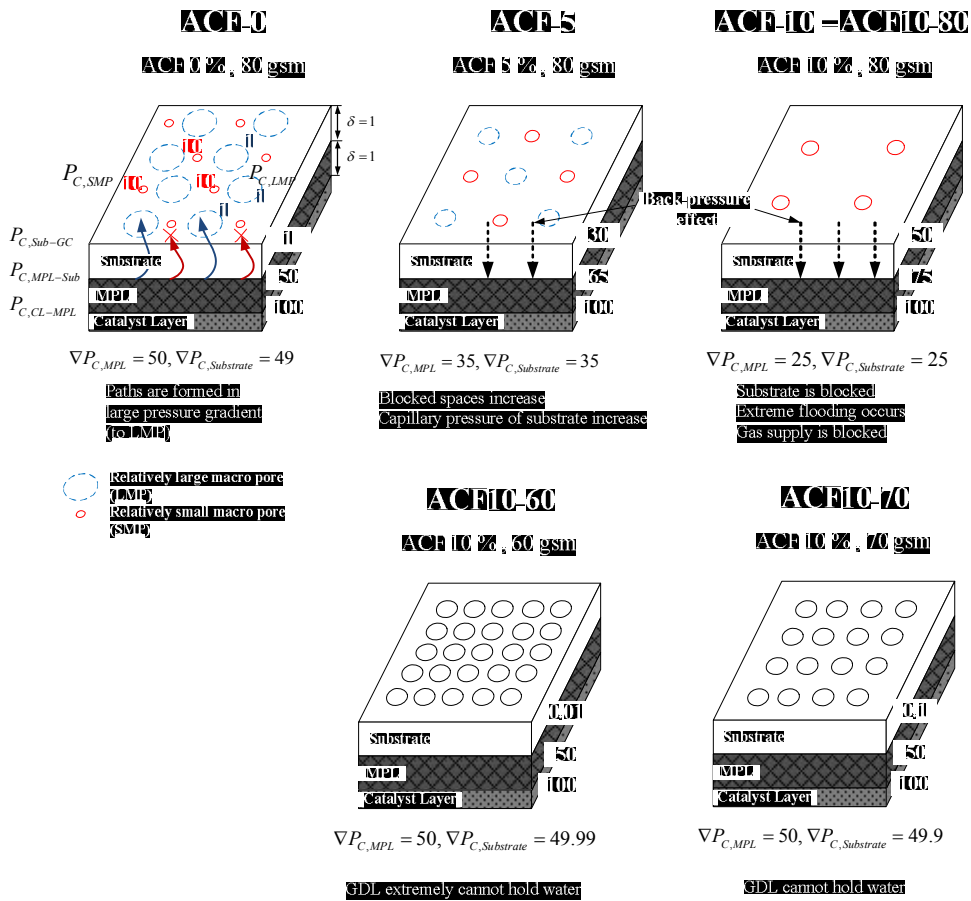


Figure 3.15 Schematic of formation of capillary pressure gradient in the substrate

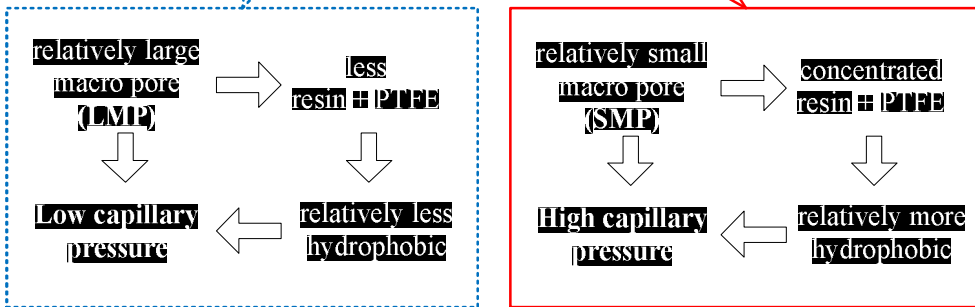
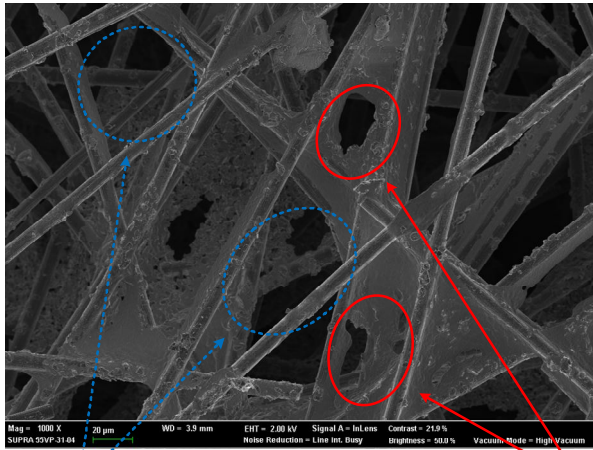
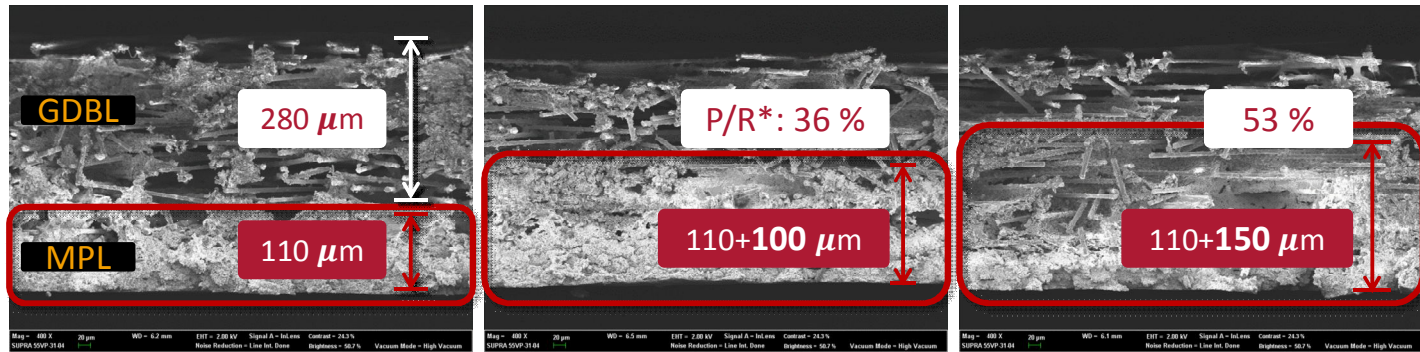


Figure 3.16 Capillary pressure difference between the relatively large macro pore (LMP) and relatively small macro pore (SMP)



\*P/R: Penetration Ratio = (depth of MPL penetration)/(depth of GDBL)

(a)

(b)

(c)

Figure 3.17 Sectional FESEM images of (a) MP-A, (b) MP-B, and (c) MP-C which has different MPL penetration thickness

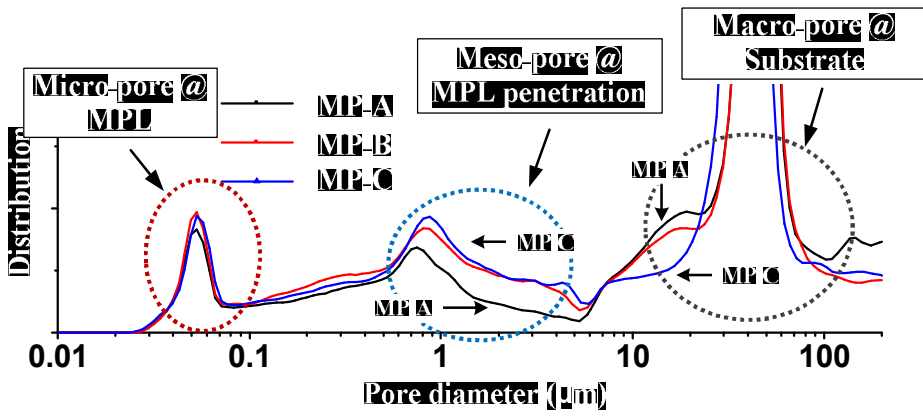


Figure 3.18 Pore distributions of MP-A, MP-B and MP-C which has different MPL penetration thickness

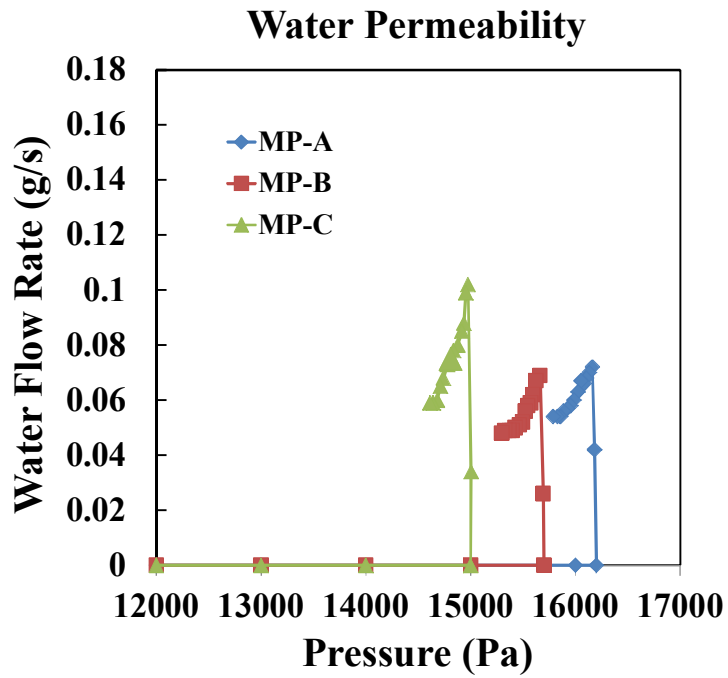


Figure 3.19 Water permeability of MP-A, MP-B and MP-C which has different MPL penetration thickness

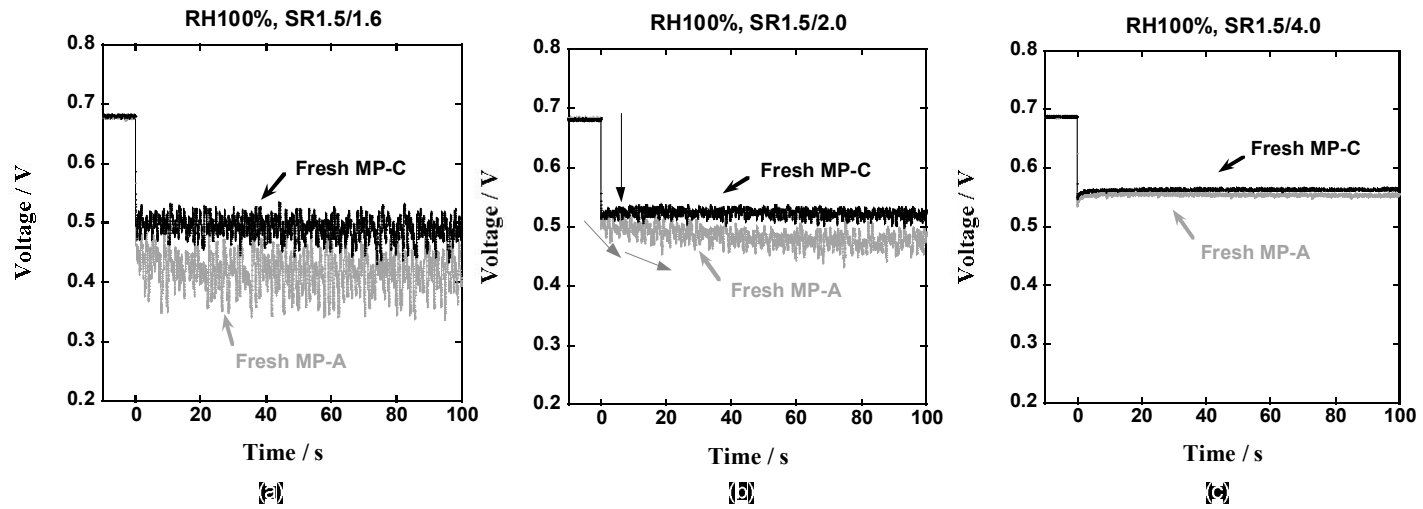


Figure 3.20 The voltage response of MP-A and MP-C as the current was changed from 15 A to 30 A at an RH of 100 % and an SR of H<sub>2</sub>/Air of (a) 1.5/1.6 (starved), (b) 1.5/2.0 (standard), and (c) 1.5/4.0 (excess)

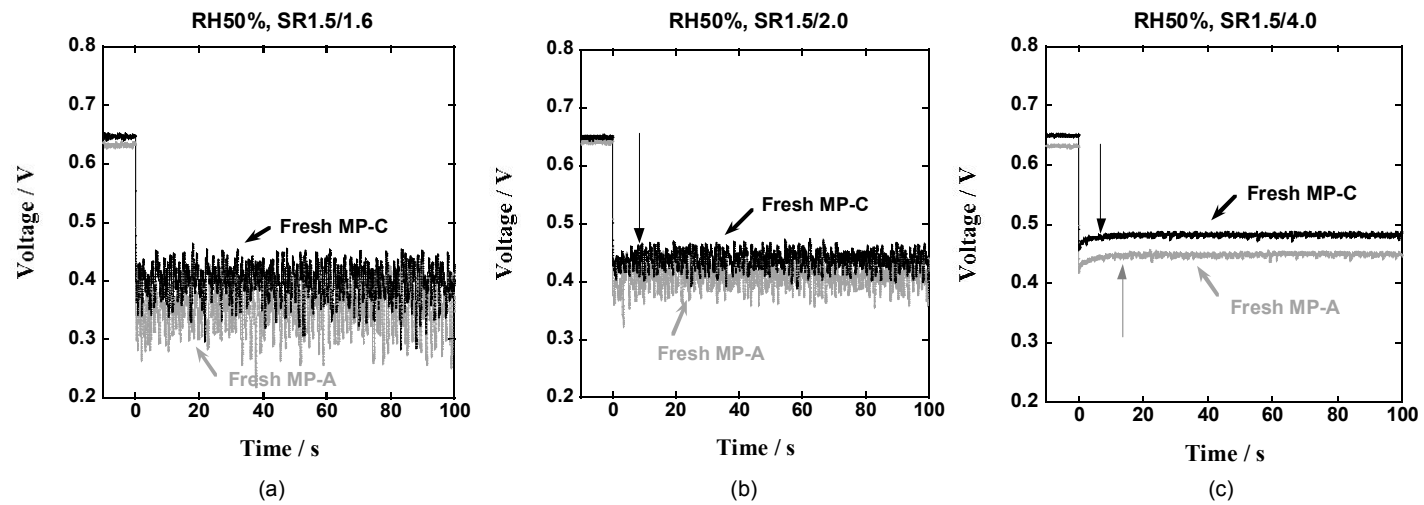


Figure 3.21 The voltage response of MP-A and MP-C as the current was changed from 15 A to 30 A at an RH of 50 % and an SR of H<sub>2</sub>/Air of (a) 1.5/1.6 (starved), (b) 1.5/2.0 (standard), and (c) 1.5/4.0 (excess)

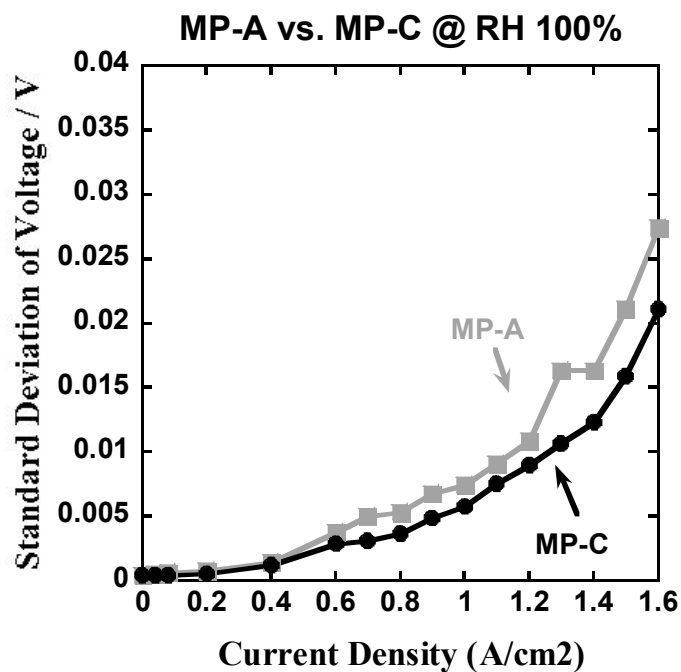


Figure 3.22 Standard deviation of the voltage as the current density was varied from 0.6 A/cm<sup>2</sup> to 1.6 A/cm<sup>2</sup> with MP-A and MP-C at an RH of 100 % and an SR of H<sub>2</sub>/Air 1.5/2.0

**(Not scaled)**

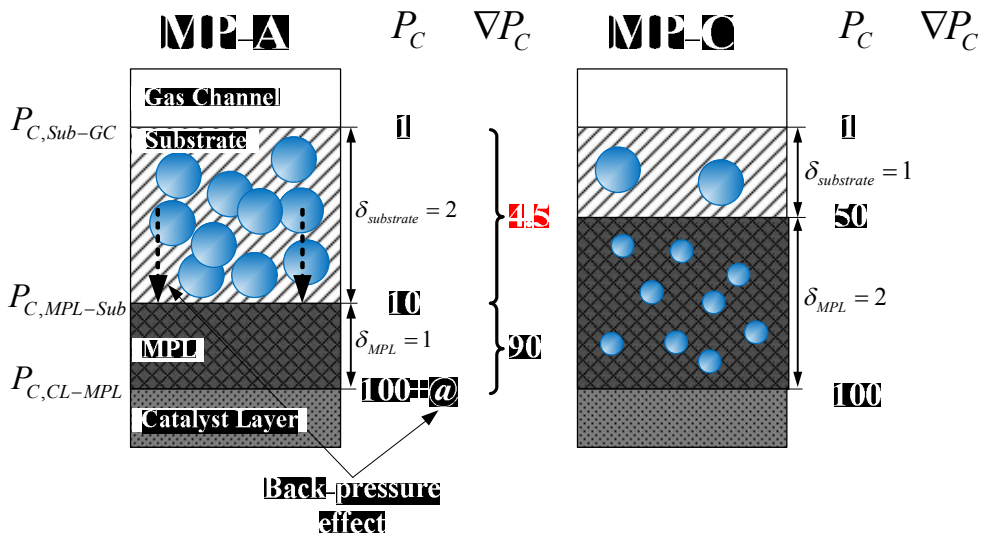


Figure 3.23 Schematic of formation of capillary pressure gradient in the MP-A and MP-C

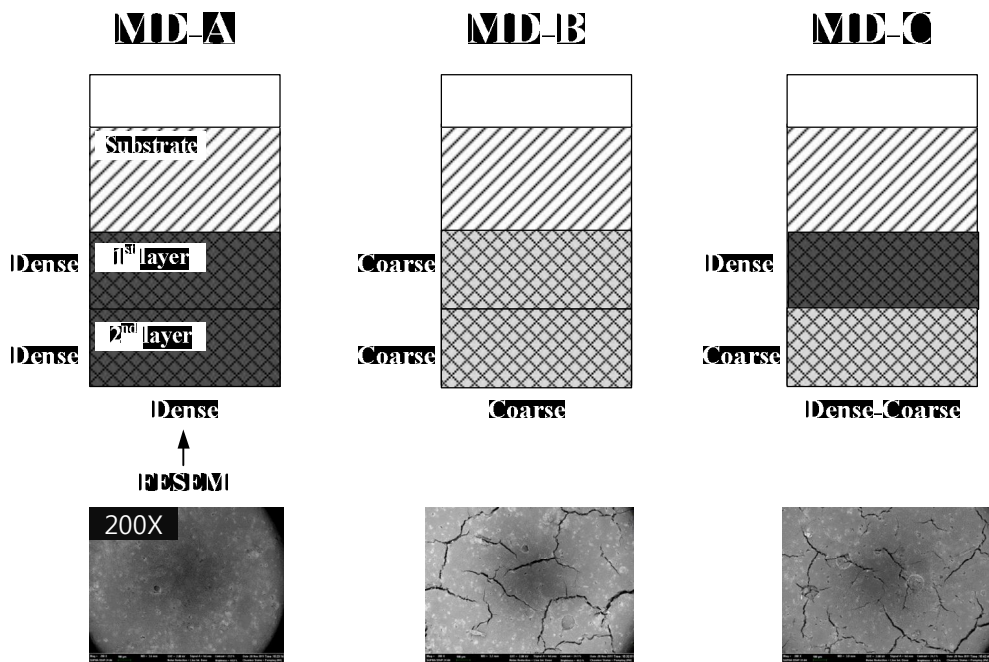


Figure 3.24 Schematic and FESEM images of MD-A,B and C

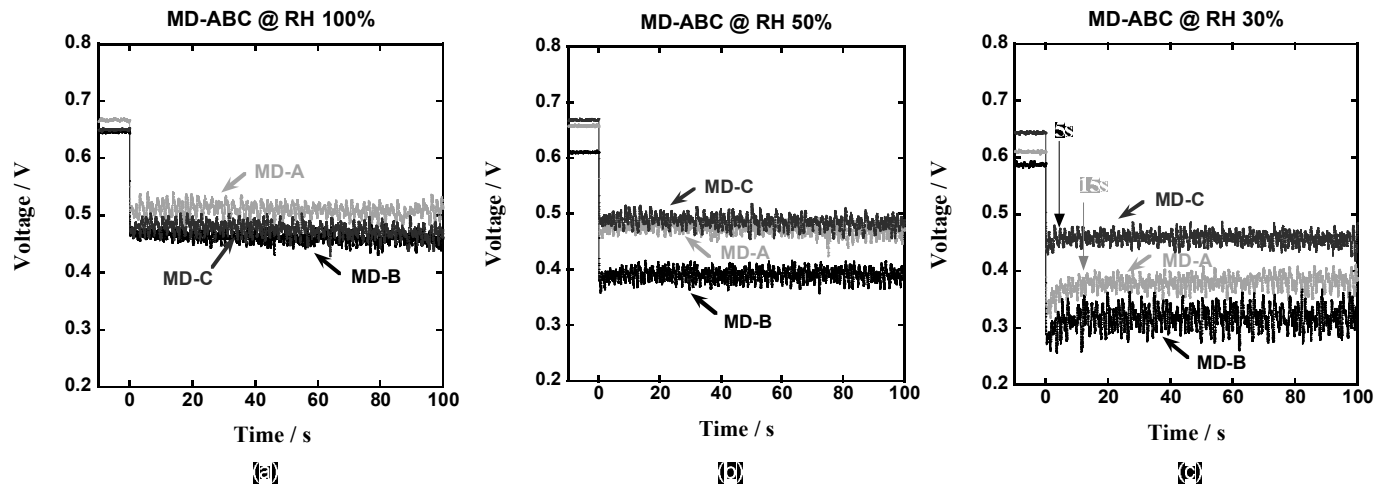


Figure 3.25 The voltage response of the MD-A/MD-B/MD-C as the current was changed from 15 A to 30 A at (a) an RH of 100 %, (b) 50 %, and (c) 30 %

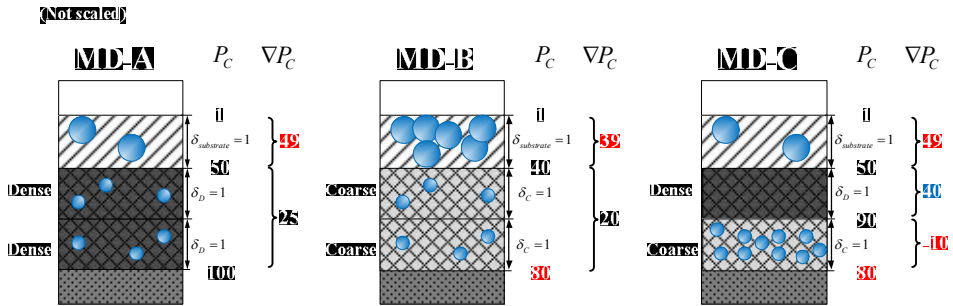


Figure 3.26 Schematic of formation of capillary pressure gradient in the MD-A, MD-B and MD-C

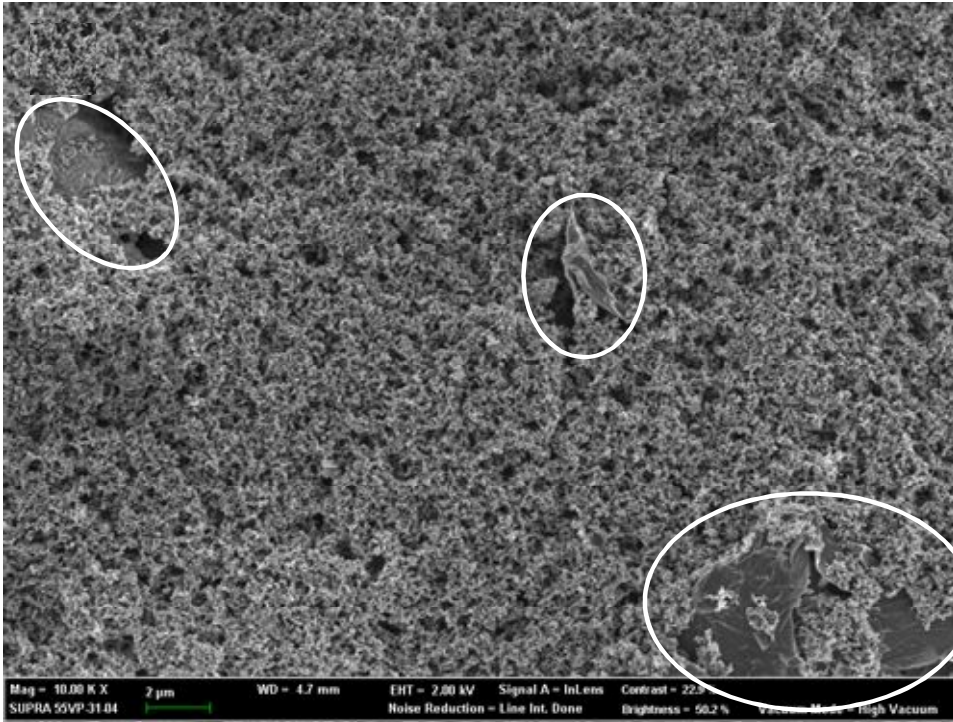


Figure 3.27 FESEM image of the MPL surface of MF-C

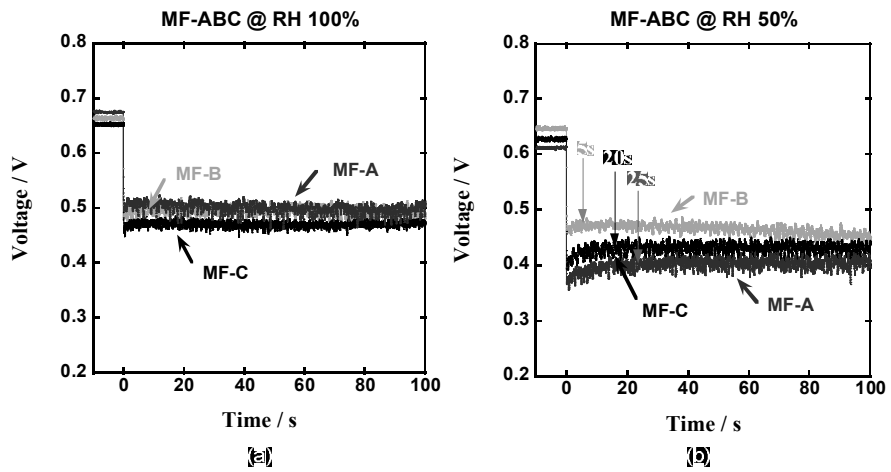


Figure 3.28 The voltage response of the MF-A/MF-B/MF-C as the current was changed from 15 A to 30 A at (a) an RH of 100 % and (b) 50 %

(Not scaled)

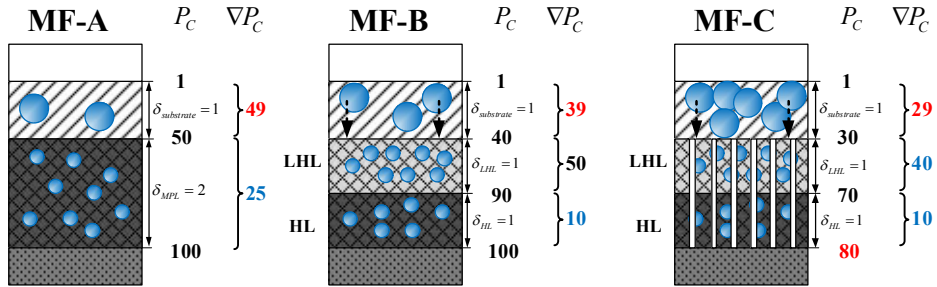


Figure 3.29 Schematic of formation of capillary pressure gradient in the MF-A, MF-B and MF-C

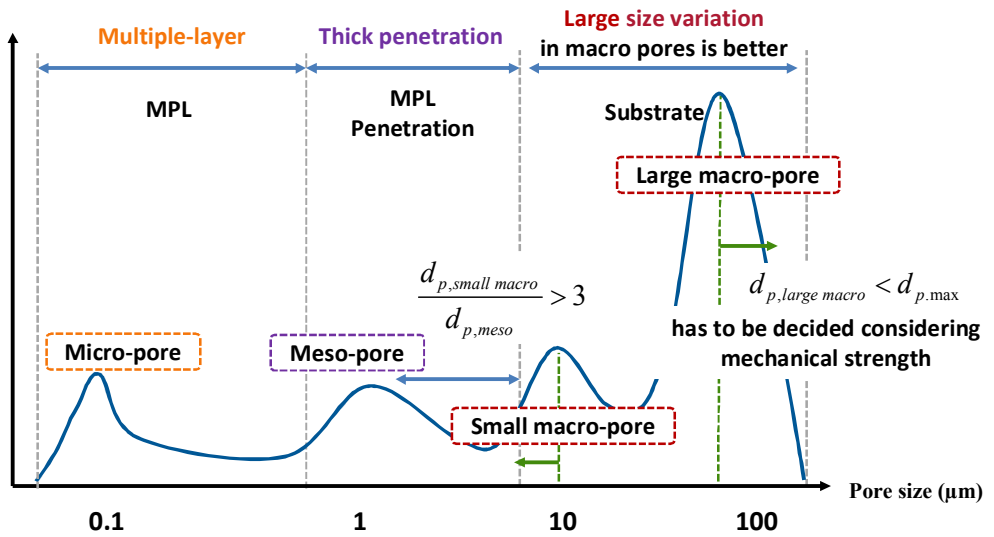


Figure 3.30 Design of pore size distribution of the GDL

## **Chapter 4. Transient response of a PEM fuel cell with a degraded gas diffusion layer**

Previous chapters showed that voltage performance loss occurs with two different transition modes when the fuel cell suddenly operates at a high load. This phenomenon is related to the mass transport deterioration through the GDL due to slow oxygen diffusion and inactive water transport. It is also shown that water holding/removal capability of the GDL has influence on transient response of the PEM fuel cell. It means that the degraded GDL, which has a different hydrophobicity and structural characteristics, changes the dynamic performance characteristics. However, there are no studies on the effects of GDL aging on the transient response of PEM fuel cells.

Therefore, the objective of this chapter is to analyze the effects of GDL degradation on the transient response of PEM fuel cells. Using two accelerated stress test methods for the GDL which are leaching and carbon corrosion tests, the GDL is aged independently. Using transient voltage response analysis as a current step change, the dynamic performance change due to degradation of the GDL was determined. Numerical investigation of mass transport change in the aged GDL also studied using pore network modeling (PNM). Furthermore, this methodology is effective as an in-situ diagnostics of GDL degradation by monitoring the transient response during sudden load changes.

## **4.1 Experimental setup**

### **4.1.1 Aging of the GDL**

GDL degradation is divided into two categories: mechanical degradation and chemical degradation. Mechanical degradation is physical damage resulting from dissolution in water from humidification and production by electrochemical reaction, and erosion by gas flow which contact the GDL's surface directly and pass through to the inside [93]. Chemical degradation of the GDL occurs due to carbon corrosion. Since the GDL is a carbon material, GDL is exposed to corrosion aging environment during cell operation as well as catalyst layer. Under start-up, shut-down and local fuel starvation conditions, the carbon reacts with the water and is washed away as a form of the carbon dioxide [80, 94]. In this study, the GDL were degraded by applying both dissolution and carbon corrosion aging mechanisms.

#### **4.1.1.1 Degradation of the GDL due to dissolution**

To age the GDL independently of the other components of PEM fuel cells and to reduce the aging time corresponding to the real operating time, an accelerated stress test, known as the leaching test, was used [93, 101]. As shown in Figure 4.1, the paper type of commercial GDL which has a thickness of 325  $\mu\text{m}$ , a porosity of 80 % and a 5 wt % PTFE loading for both substrate and MPL coating was used. Samples 6 cm  $\times$  6 cm in size were used, and 8 samples were immersed in a 1-L bottle of deionized (DI) water, and then the bottles were maintained in a vacuum chamber for 12 hours to remove micro-air bubbles located inside the GDL, especially inside the MPL, to enhance the penetration of the leaching solution. In a constant temperature oven, the samples were maintained in a free-standing condition for 2160 hours at a temperature of 80  $^{\circ}\text{C}$ .

During the test, changes in the properties were observed using various methods. The contact angles of both sides of the gas diffusion medium (GDM) and MPL were investigated at 0, 168, 336, 720, 1440 and 2160 hours. To measure the static contact angle, a water droplet was made with a micro syringe pump (Harvard Apparatus Pump 11), and a SUGITOH zoom lens (TS-93001) and halogen lamp (150 W) were used. The measurement of droplet height and contact angle was performed with NEX MEASURE software. Theoretically, the contact angle is defined as the static contact angle when the droplet height equals zero because the static contact angle increases as the droplet height increases [14, 93]. Thus, extrapolation of various contact angle points as various heights of droplet must be performed to obtain the static contact angle of one GDL. However, this process requires too much time and effort, so the height of the water droplet was kept constant at 1.3 mm, and the contact angle was measured at that point. In addition, the change of the structure was captured using field-emission scanning electron microscopy (FESEM, Carl Zeiss SUPRA 55VP), and the change of the components of the GDL was observed using thermo gravimetric analysis (TGA, TA Instruments Q-5000 IR).

#### **4.1.1.2 Degradation of the GDL due to carbon corrosion**

Carbon corrosion highly occurs when 1.45 V of potential is imposed in the PEM fuel cell under start-up, shut down and local fuel starvation conditions [80, 94]. Three-electrode corrosion kit was established to enable exact impose of potential on the GDL independently as shown in Figure 4.2. The GDL is a working electrode, Pt mesh and Ag/AgCl was used for counter electrode and reference electrode respectively. 0.5 M of sulfuric acid was used as an electrolyte. The potentiostat (Solatron analytical 1255B LF Frequency Response Analyzer and 1480A Multistat) was used to impose potential in this system. 96 hour of corrosion time was determined which corresponding for 5000 hours of PEMFC operation [80, 94].

The GDL samples were selected expecting carbon loss in the MPL penetration parts because our research team has reported that carbon corrosion of the GDL occurs mainly in the MPL penetration part [80, 94]. The GDLs which have different MPL penetration thickness used in the chapter 3: MP-A and MP-C were tested. These are the paper type of GDL which has a thickness of 380  $\mu\text{m}$ , a 10 wt % and 23 wt % PTFE loading for substrate and MPL, respectively. MP-A has a thin MPL penetration in contrast MP-C has a thick MPL penetration reminding in Figure 3.4.

After corrosion, various properties of the GDL were assessed by investigating contact angle, weight, thickness, pore distribution, FESEM image and water permeability change.

#### **4.1.2 Fuel cell and test station**

As shown in Figure 3.2, a 25  $\text{cm}^2$  unit cell was used to investigate the effect of the aged GDL on the cell performance. The same GORE™ PRIMEA® 5710 MEA catalyst coated membrane was used for each test. The aged GDL and the fresh GDL were tested separately. The aged GDLs were attached to both side of the anode and cathode. All test protocols were maintained in the same way for both GDLs. Humidified high purity hydrogen and air were supplied to the cell. Nitrogen gas was used to purge the cell for each experimental case to obtain the same experimental condition. The electric loader was used to control the load changes, and a data acquisition board from National Instrument was used to obtain fast and reliable voltage responses during the load changes. A more detailed description of the fuel cell test station is presented in previous chapters.

#### **4.1.3 Experimental conditions**

As shown in Table 4.1, the voltage response was investigated at sudden load current change from 15 A to 30 A, which corresponds to 0.6  $\text{A}/\text{cm}^2$  to 1.2  $\text{A}/\text{cm}^2$  in

current density, and then from 30 A to 15 A. Voltage data were obtained with a data acquisition rate of 100 Hz. Because it takes about one minute for PEM fuel cell to reach a new steady-state after load change, the cell was operated for three minutes at a prior load before the load change. To investigate the effect of the relative humidity, 50 % and 100 % RH conditions were used. To study the effect of the flow rate of air, three cases for each RH condition were used based on a stoichiometric ratio (SR), of the air: 1.6 for the “starved” condition, 2.0 for the “standard” condition and 4.0 for the “excess” condition. Because the SR of the air is a dominant factor in high load operating conditions, the SR of the hydrogen was fixed at 1.5 for the standard condition. Due to the physical limitations of the response of the gas flow, the flow rates were fixed at the SR of the high load condition. A temperature of 65 °C and a pressure of one bar were maintained for all cases.

## 4.2 Experimental results

### 4.2.1 Transient response of a PEM fuel cell with an aged GDL

#### degraded by dissolution

##### 4.2.1.1 Change of GDL properties due to dissolution

Figure 4.3 shows the change of the contact angle of the GDL during the leaching test. The solid line shows the decrease of the contact angle of the substrate face, and the dotted line shows the data for the MPL face. After about 2000 hours, the contact angles of the substrate and MPL faces decreased by 6.8 and 7.7 degrees, respectively, corresponding to a decrease of the hydrophobicity. The contact angle sharply decreased at early aging stage then went to steady state as a time passed. Changes in the carbon structure for both substrate and MPL after the leaching test are shown in Figure 4.4. Figure 4.4-(a) shows fresh GDL which is composed of carbon fibers and carbon fillers. The carbon fillers combine each carbon fiber and fill empty space. The carbonized resins and PTFEs cover carbon fillers and carbon fibers. After aging, Figure 4.4-(b) shows that carbonized resins are washed out, thus carbon fillers are exposed to atmosphere. Thus, the loss of hydrophobicity is directly related to the loss of hydrophobic carbonized resins, determined by analyzing the TGA results shown in reference [93]. Eventually, the hydrophobicity loss is dominant inside the substrate. In addition, loss of the carbon part in the MPL face was also observed. In the MPL, as a macro view, there are no big structural changes. However, as shown in Figures 4.4-(c) and (d), there are some losses of carbon particles in the crack which is the weakest part of the MPL and surface of the MPL is smoothened.

To explain the following experimental results, it is necessary to discuss the relationship between the contact angle and the capillary pressure. In this accelerated

aged GDL, the contact angle decreased after the leaching test. The contact angle is related to the capillary pressure of the GDL, and the capillary pressure is the driving force for water removal through the GDL. Revisiting the general relationship between the contact angle and capillary pressure is expressed below:

$$P_c = \tau \cos(\theta_c) \left( \frac{\varepsilon}{K} \right)^{1/2} J(s) \quad (4.1)$$

where  $P_c$  is the capillary pressure,  $\tau$  is the surface tension,  $\theta_c$  is the contact angle,  $\varepsilon$  is the porosity,  $K$  is the permeability and  $J(s)$  is the Leverett J-function. The Leverett J-function is expressed below [22, 93]:

$$J(s) = 1.417s - 2.120s^2 + 1.263s^3 \quad (4.2)$$

where  $s$  is the liquid water saturation.

If other properties are the same, the cosine function of the contact angle is directly related to the capillary pressure. In this study, the contact angle of the aged sample decreased from  $151^\circ$  to  $144^\circ$ , and thus the amount of capillary pressure decreased by 7.5%. This change of capillary pressure inside the GDL is a key factor in the explanation of the following results for the transient response of the PEM fuel cell.

#### 4.2.1.2 Transient response change due to dissolution

Figure 4.5 and Table 4.2 show the voltage response results for case 1-1, in which the current was changed from 15 A to 30 A at an RH of 100 % under a variety of SR, including (a) an SR of 1.6 representing starved conditions, (b) an SR of 2.0 for standard conditions and (c) an SR of 4.0 for excess conditions. These

figures show that a slight performance loss occurs in the case of an aged GDL at fully humidified conditions. Voltage losses of 8.2 % and a 4.9 % occur under starved and standard air flow rate conditions, respectively. These results indicate that property change of both substrate and MPL deteriorate voltage response. However, the effect of an aged GDL under fully hydration condition is smaller than that of low humidified condition which is shown in following results in this paper. Specifically, if the ion conductivity of the membrane is maintained at a high level, the deterioration of the mass transport properties in the GDL is not dominant at the moment of load change. Under low flow rate conditions, where the importance of mass transport ability becomes dominant, worse voltage response is observed due to the change of surface morphology induced by damage in the MPL. At high air flow rate conditions, almost the same voltage response is shown.

Voltage response results for 15 A to 30 A cases at RH 50 % conditions are shown in Figure 4.6 and Table 4.2. In contrast to the fully humidified condition, there are significant voltage losses after the load change in the case of the aged GDL. Voltage losses of 18.6 %, 13.6 %, and 17.0 % occur under starved, standard and excess air flow rate conditions, respectively. It may be confused why the trend of voltage loss is not consistent as air flow rate is increased, which amount of voltage loss at an excess condition is higher than that of a standard condition. In the case of the excess conditions for a fresh GDL, because of high mass transport to the catalyst layer due to sufficient convection and diffusion process through the GDL, the performance of a cell was highly enhanced at low RH condition. Thus, reference voltage for a fresh GDL was highly increased at SR of 4 than the SR of 2, consequently the difference between fresh and aged case at SR of 4 was increased than the SR of 2. Thus, voltage difference trend seems to be broken as SR increases at 50 % RH condition.

With voltage loss, voltage fluctuation phenomena existed in the case of an aged GDL, and the voltage response was more unstable when the air flow rate decreased.

Figure 4.7 presents the previous results from – 1 s to 5 s, showing the moment of load change more clearly. In the case of an aged GDL, a larger undershoot occurred when the SR of the air decreased than in the case of a fresh GDL.

The fact that transient voltage response of the PEM fuel cell shows two different time delays until it reaches a new steady-state was presented in a previous chapter. Reminding the schematic of voltage response shown in Figure 2.6, the first stage time delay is the time that the voltage decreases continuously until it reaches the minimum level. It occurs due to time delay to penetrate the GDL for gas. The second stage time delay is due to membrane water content recovery. As the load changes to a high current density, the membrane dehydrates and the membrane resistance correspondingly increases, inducing a voltage loss. In time, due to the supply of humidified gas and internal hydration from electro-osmotic drag and back diffusion, the membrane becomes hydrated, resulting in voltage recovery.

In Figure 4.6, the second-stage undershoot, which indicates voltage loss due to membrane dehydration, was larger and the voltage recovery time was longer than those for a fresh GDL. These results indicate that when the GDL is degraded, its effects are more dominant under low humidification conditions.

In Figure 4.7 there was an approximately 0.1 s time delay, which indicates a continuous voltage drop after load change. All these results support a mass transfer loss due to low capillary pressure induced by the hydrophobicity change in the aged GDL.

Based on this experimental study, the voltage response fluctuation occurred under low humidity conditions. For further investigation, the standard deviation of the voltage level in the high current density region was investigated at an SR of 1.5/2.0. As shown in Figure 4.8, the standard deviation of the voltage increased as the current density increased, which means that the effect of mass transfer loss increased at low humidity when the GDL was degraded.

This phenomenon can be explained by Figure 4.9. The change of the GDL properties induces an uneven local capillary pressure distribution corresponding to uneven mass transport motion through the GDL. Then, water moves to a passage that has a lower energy level than other passages. Given that there are only a few selective water passages through the GDL [102], the number of water passages decreases. In addition, water tends to stay in lower capillary energy spots, forming a water-lake inside the GDL. Then, the possibility of local flooding not at a channel but at the GDL substrate becomes high, which induces uneven membrane hydration and oxygen depletion. This process eventually causes an unstable and lower voltage response at high loads. This effect is more dominant under more harsh conditions, such as low humidity conditions, because when there is enough water inside the GDL, water overcomes the resistance of the water-lake that is a bottleneck point for water supply and removal.

In the case of the transient response, with a sudden load change in special, low load to high load operation, the membrane becomes dehydrated instantly because a large number of protons move to the cathode side suddenly, which causes a large electro-osmotic drag motion. Before the back diffusion motion induced by the accumulation of water produced at the cathode side occurs, the membrane is dehydrated, such that ion conductivity becomes worse. Reacting gases are also consumed rapidly. Therefore, the supply of water carried by the humidified gas is very important. Under fully humidified conditions, after a sudden load change, more stable water supply to the dehydrated membrane can be obtained regardless of the loss of hydrophobicity in the GDL. However, under low humidification conditions, there is significant lack of water with the loss of water passages and local GDL flooding due to a spatial loss of hydrophobicity. Thus, the transient voltage response of the fuel cell becomes worse under low humidification conditions where degradation effects of the GDL are dominant. Therefore, it is necessary to conduct transient response analysis to investigate the mass transport characteristics of PEM fuel cells.

The results presented in Figure 4.10, when the current was changed from 30 A to 15 A corresponding to high load to low load operation at 50 % RH at various SR conditions, also support this analysis. Because the flow rates were fixed at the SR of the high load condition, the SR of the low load condition is an excess flow rate condition, which means that the membrane is sufficiently hydrated after the load change. Therefore, overshoot occurs at the moment of load change. Interestingly, though the voltage level at high load operation was lower, the overshoot becomes larger when an aged GDL was used contrast to the case of a fresh GDL because water that remains inside the GDL helps to hydrate the membrane continuously for several minutes before reaching the steady state. This result is in agreement with the hypothesis that a water-lake was formed inside the GDL due to a spatial loss of the hydrophobicity. This hypothesis also investigated in following sub-chapter by numerical simulation of the GDL using pore network modeling (PNM).

## **4.2.2 Transient response of a PEM fuel cell with an aged GDL**

### **degraded by carbon corrosion**

#### **4.2.2.1 Change of GDL properties due to carbon corrosion**

After corrosion, basic characteristics changes of GDL were measured. As shown in Figure 4.11, after 96 hours corrosion, both MP-A and MP-C shows about 2.4 % of weight decrease. Weight change is similar for both cases because the corrosion time is the same. This result indicates that carbon corrosion rate is the same because the same materials were used for both GDLs though structure is different.

Also thickness of GDL was measured at nine points. In average, 6.31 % and 4.26 % of thickness decreases in case of MP-A and MP-C respectively. The result that thickness decrease of MP-A is larger than MP-C indicates that carbon corrosion

occurs at the penetration parts. Figure 4.12 shows schematic of carbon corrosion process in the MPL penetration part. When the GDL is manufactured, the MPL slurry is attached onto the substrate as a surface coat and MPL slurry penetrates into the substrate. In this MPL penetration part which is the center layer of the GDL, carbon particles which have high surface area are attached on the carbon fibers. Since different two components (carbon fibers and carbon particles) are bonded by impregnation process, binding forces consequently weak. In contrast, carbon particles are well agglomerated in the MPL. Thus, the MPL penetration part between the substrate and MPL is the most probable part which can be corroded by electrochemical attack. As a result, the MP-A shows less thickness decrease than the MP-C because carbon particles in the penetration parts were mainly corroded.

This hypothesis is also verified by pore distribution change measured by mercury porosimetry. The MP-A and MP-C show different shape change of pore distribution as shown in Figure 4.13. For both cases, pore size of the MPL increased after aging because carbon particles in MPL were corroded. In case of MP-C, meso-pore which was formed in MPL penetration part disappeared after aging and macro-pore increased. As a result, shape of pore distribution of aged MP-C is similar to that of fresh MP-A. All these results indicate that MPL penetration parts were corroded after electrochemical aging. This conclusion also verified by SEM images. Figure 4.14 shows FESEM images of MP-A and MP-C before/after aging. MPL layers were damaged for both cases, in special, in case of MP-C, there are many empty spaces in the middle layer of the GDL by carbon corrosion. Through series of experimental results, it is concluded that MPL penetration part of the GDL is attacked by carbon corrosion in PEM fuel cell.

Figure 4.15 shows the change of contact angle after aging. The amount of decrease was not opened but result of commercial GDL was added to show similar hydrophobicity loss. Decreasing tendency of contact angle of MP-A and MP-C is the almost same. In special, hydrophobicity of the MPL side decreased significantly because MPL side was corroded than the substrate side. As carbon disappeared,

PTFE attached on the carbon particles was disappeared too. In addition, when carbon oxidized, hydrophilic radicals like OH- might be made on the surface of the MPL side inducing contact angle decrease.

Water permeability is also changed after aging as shown in Figure 4.16. At first, pressure of start-of-penetration decreased after aging from 16181 Pa to 14289 Pa and from 15004 Pa to 13533 Pa for MP-A and MP-C respectively due to increment of micro pore size in the MPL. Second, the slope of penetration  $\frac{\Delta\dot{m}}{\Delta P}$  of MP-C decreased after aging, and became like that of fresh MP-A. This result indicates larger driving force is required to push the same amount of water through the GDL. Consequently, deterioration of water removal ability occurs and the flooding may be occurred at fully humidification condition.

#### **4.2.2.2 Transient response change due to carbon corrosion**

At first, Figure 4.17 shows steady-state performance of MP-A and MP-C before/after aging at fully humidification condition. Actually, after 96 hours corrosion, performance of both GDLs was deteriorated seriously due to enormous decrease of hydrophobicity on the surface, so it is hard to distinguish structural aging effect of the GDL. Thus, about 20 hours corrosion results are shown in this section in order to investigate performance difference after aging due to MPL penetration thicknesses. Performance decreased at fully humidification condition for both cases due to decrease of hydrophobicity, which means decrease of capillary pressure gradient. In case of MP-C, effect of structural change induced deterioration of water removal ability as shown in water permeability results, consequently mass transfer loss increased at fully humidification condition, thus performance loss is larger than MP-A.

Results of transient response are also support this phenomenon shown in Figure 4.18. Results of MP-C that show harsh deterioration of transient response

are shown with cathode SR. In case of MP-C, at relative humidity of 100 %, larger undershoot occurs and voltage instability increased after load change. Voltage was more unstable as stoichiometric ratio of cathode decreases because product water cannot be easily removed and reactant gases cannot be supplied enough. As shown in the SEM analyses, the empty spaces are generated in the penetration part of the GDL. These empty spaces make water accumulation, thus large amount of suddenly produced water at the catalyst layer can be trapped in this region and remain stayed because of a lack of capillary pressure as shown in water permeability results. As a result, diffusion of reactant gases is interfered due to severe flooding.

This phenomenon also detected in results of 50 % RH condition as shown in Figure 4.19. Although the properties of the GDL were deteriorated, trapped water causes increase of water concentration in the GDL consequently induces increase of back diffusion from the GDL to the membrane. Thus, performance decrease is small in this case. Through series of results, it is concluded that mass transport loss through the GDL due to carbon corrosion aging induces decrease of steady-state and transient response of PEMFC.

However, deterioration appearance of transient response after carbon corrosion is somewhat different from results of dissolution degradation as shown in the section of 4.2.1.2. Figures 4.5 and 4.6 show that transient response became worse at low humidification condition after leaching aging test. In contrast, Figures 4.18 and 4.19 show that transient response became worse at fully humidification condition after carbon corrosion aging test. It is because that each degradation mechanism induced different structure and hydrophobicity change characteristics consequently caused different water accumulation location in the GDL. This hypothesis is described in Figure 4.20.

Dissolution aging induced water-lake formation in the substrate of the GDL as revealed in the SEM analysis and transient response investigations as shown in

Figure 4.20-(a). Thus, water tends to accumulate in the local less hydrophobic spots because  $\nabla P_{C,MPL-aged\ substrate}$  is high and  $\nabla P_{C,aged\ substrate-GC}$  is low. This means water concentration of the MPL is lower than that of the substrate. As a result, near the catalyst layer, back diffusion transport of water from GDL to catalyst layer is weakened. In addition, there are only a few roots of water passages in the catalyst layer, which decreases water concentration of the catalyst layer.

On the other hand, carbon corrosion induced empty layer between the MPL and the substrate due to loss of carbons in the MPL penetration part. In addition,  $P_{C,aged\ MPL}$  also decreased, thereby  $\nabla P_{C,CL-aged\ MPL}$  and  $\nabla P_{C,MPL\ P.-substrate}$  decreased too, then water tends to trapped along this region as shown in Figure 4.20-(b). This water layer formed through lots of region of the GDL deteriorates water removal from the catalyst layer in fully humidification which consequently induces large undershoot and unstable voltage response as shown in Figure 4.18, however, induces positive effects in low humidification condition resulting increase of back diffusion from the GDL to the membrane.

## 4.3 Numerical study using pore network modeling

### 4.3.1 Simulation of the degraded GDL

To verify water accumulation effects in the degraded GDL, numerical analysis by using pore network modeling (PNM) was conducted by Sang Gun Lee, Jung Ho Kang and Charn-Jung Kim at computer aided thermal design laboratory of Seoul National University.

At first, a calculation domain of the GDL was established as shown in Figure 4.21. A square shape of the GDL which has a width of 900  $\mu\text{m}$  and a thickness of 300  $\mu\text{m}$  was generated with a contact angle of 150° to have hydrophobicity as shown in Figure 4.3 at fresh condition. Pore-network was generated as shown in Figure 4.22-(a) to have 60 x 60 x 20 cubic cells which correspond to 900 x 900 x 300  $\mu\text{m}$  of the GDL. Thus, 1 cell had a length of 15  $\mu\text{m}$ . To simulate aged GDL which have locally less hydrophobic spaces inside the GDL consequently water-lakes were formed as explained in Figure 4.9, two 20 x 24 x 6 cubic cells regions which has a contact angle of 140° were generated because about a contact angle of 10° was decreased after 2000 hours leaching test as shown in Figure 4.3.

The detailed equations of pore network model were explained in reference [61], so several important relations are included in this research. In PNM, liquid water moves by capillarity-driven process through the GDL which is dominated by the invasion-percolation process with capillary fingering. Capillary pressure is calculated as:

$$p_c = p_w - p_a = \sigma |\cos \theta_w| \left( \frac{1}{R_1} + \frac{1}{R_2} \right) = \frac{2\sigma |\cos \theta_w|}{r_{w/a}} \quad (4.3)$$

where subscript of  $w$  means water, subscript of  $a$  means air,  $\sigma$  is the surface tension,  $\theta_w$  is the contact angle,  $R_1$  and  $R_2$  are two principal radii of curvature;  $r_{w/a}$  is the mean radius of curvature of the water-air interface. This equation is fundamental expression of capillary pressure similar to equation of (4.1) as shown in previous chapter.

The pore-networks are composed of cross-connected box-shaped pores and throats as shown in Figure 4.22-(b). According to the invasion-percolation water transport rule, liquid water preferentially invades the throat with the smallest capillary entry pressure:

$$p_t = \frac{2\sigma |\cos \theta_w|}{r_t} \quad (4.4)$$

$$r_t = \frac{2A_t}{P_t} = \frac{d_{ta}d_{tb}}{d_{ta} + d_{tb}} \quad (4.3)$$

where subscript of  $t$  means the throat,  $r_t$  is the hydraulic radius,  $P_t$  is the perimeter of the throat also shown in Figure 4.22-(c), (d).

Mass conservation:

$$\sum_{j=\text{neighboring six pores}} Q_{i \rightarrow j} = 0 \quad (4.5)$$

where  $Q_{i \rightarrow j}$  denotes the flow rate from a pore  $i$  to its neighboring pore  $j$ .

Constitute equation:

$$Q_{i \rightarrow j} = G_{ij} \left[ \max(p_{c,i}, p_{t,ij}) - \max(p_{c,j}, p_{t,ij}) \right] \quad (4.6)$$

$$G_{ij} = \frac{A_{w,ij} r_{t,ij}^2}{8\mu_w l_{t,ij}} \quad (4.7)$$

where  $G_{ij}$  denotes flow conductance which is derived from the Hagen-Poiseuille equation,  $A_w$  is the flow area of liquid water in a rectangular throat and  $\mu_w$  is the viscosity of the water. This equation expresses the invasion-percolation movement of water to the neighbor pore which has a low energy level in the pore network model. More detailed relations and equations are presented in reference [61].

Calculations were conducted in two cases which whole domain has a uniform contact angle of  $150^\circ$  and domain has a locally degraded region contact angle of  $140^\circ$ . Water was injected on the bottom surface as a constant rate corresponding to  $2 \text{ A/cm}^2$  current density of the fuel cell operation. A temperature of  $78^\circ \text{C}$  and a porosity of 65 % general boundary conditions were imposed in this simulated aged GDL.

### 4.3.2 Simulation results

Simulation results of liquid water saturation distribution are shown in Figure 4.23. The yz-plane section at  $x=210$  and  $x=690$  were selected at the location of partially less hydrophobic regions to plot change of liquid water saturation before/after aging of the GDL. In the first yz-plane section at  $x=210$ , up-left region which has a contact angle of  $140^\circ$  became fully saturated after aging. About entire

pores were filled with liquid water in this locally aged region, and this phenomenon was also obtained in the yz-plane section plot at  $x=690$ . The liquid water was accumulated after aging in right-bottom region of this plane section which means water-lake was formed inside of the GDL as presented in previous chapter.

To investigate this increase of water saturation, quantitative result is shown in Figure 4.24. From bottom surface of the calculation domain, liquid water saturation of the xy-plane along the z-coordinate was presented. A degraded region was placed in z-coordinate from  $z=60$  to  $150\ \mu\text{m}$  and  $z=150$  to  $240\ \mu\text{m}$ . From a height of  $120\ \mu\text{m}$ , liquid water saturation increased in the aged GDL than the fresh GDL. At a height of  $150\ \mu\text{m}$  where both locally degraded regions were located, the maximum of liquid water saturation was obtained as 0.248, and the maximum increase of liquid water saturation was shown at a height of  $165\ \mu\text{m}$  which increase rate is 19.88 %. In average, 10.3 % of liquid water saturation was increased in the simulated aged GDL due to formation of water-lake inside a GDL which water tended to move and be trapped in this region because energy level was lowered caused by loss of hydrophobicity. Then, reactant gas diffusion was lowered due to lowered number of vacant pores, and large water accumulation-drainage movement induced unstable gas supply and water concentration in the GDL which is also connected to back diffusion momentum of water balance of the membrane hydration.

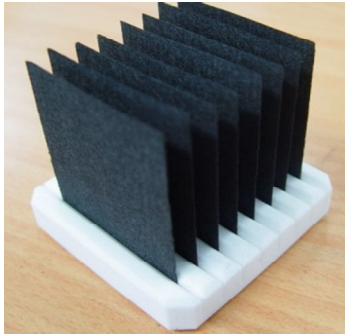
From numerical investigation of the water transport in the simulated aged GDL, it is concluded that aged GDL induces water accumulation inside of the GDL, thus interferes gas and water diffusion in the GDL to the catalyst layer and the membrane consequently induces deterioration of the transient response of the PEM fuel cell. All these interpretations are coincided with series of experimental results reported in the previous chapters.

Table 4.1 Experimental cases.

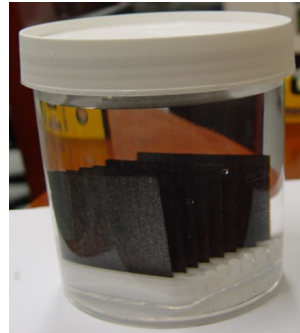
Case	Current step	Relative Humidity (%)	Stoichiometric Ratio (H <sub>2</sub> /Air)	Temperature (°C)
1-1	15 A to 30 A	100	1.5/ <b>1.6</b> (starved)	65
1-2	(0.6 to 1.2 A/cm <sup>2</sup> )	50	1.5/ <b>2.0</b> (standard) 1.5/ <b>4.0</b> (excess)	
2-1	30 A to 15 A	100	1.5/ <b>1.6</b> (excess)	
2-2	(1.2 to 0.6 A/cm <sup>2</sup> )	50	1.5/ <b>2.0</b> (more excess) 1.5/ <b>4.0</b> (most excess)	

Table 4.2 Voltage performance loss using the degraded GDL under various operating conditions.

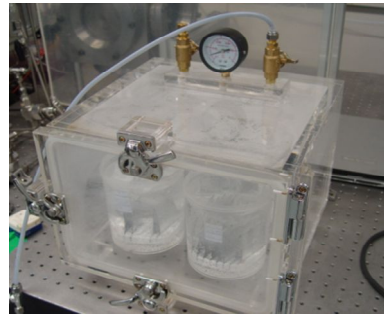
Case	Current step	Relative Humidity (%)	Stoichiometric Ratio (H <sub>2</sub> /Air)	Voltage loss (%)	
1-1	15 A to 30 A	100	1.5/ <b>1.6</b> (starved)	8.16	
			1.5/ <b>2.0</b> (standard)	4.90	
			1.5/ <b>4.0</b> (excess)	1.0	
1-2		15 A to 30 A	50	1.5/ <b>1.6</b> (starved)	18.6
				1.5/ <b>2.0</b> (standard)	13.6
				1.5/ <b>4.0</b> (excess)	17.0



**GDL Samples**



**Leaching solution**



**Vacuum chamber**



**Oven (80°C)**

Figure 4.1 Experimental procedure of leaching test

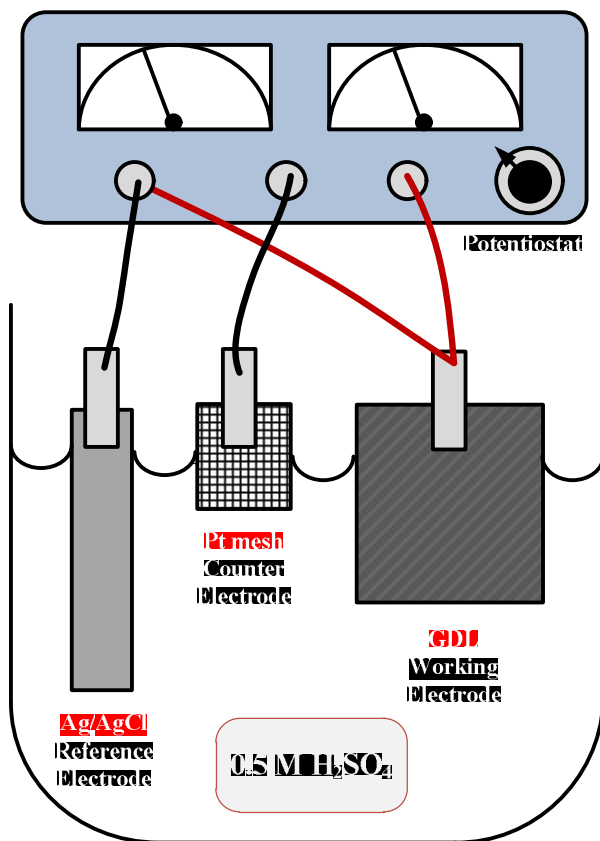


Figure 4.2 Experimental apparatus of three-electrodes carbon corrosion test

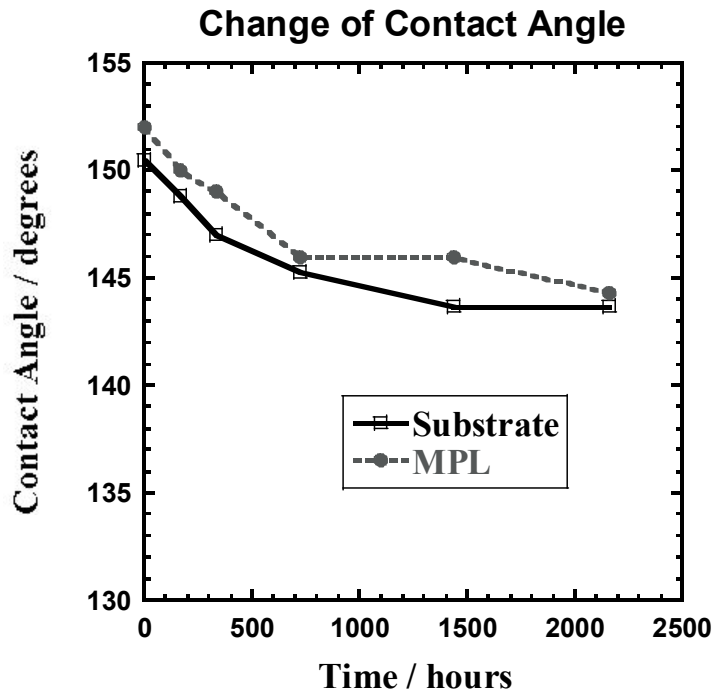


Figure 4.3 Changes in the contact angle of the GDL during the leaching test

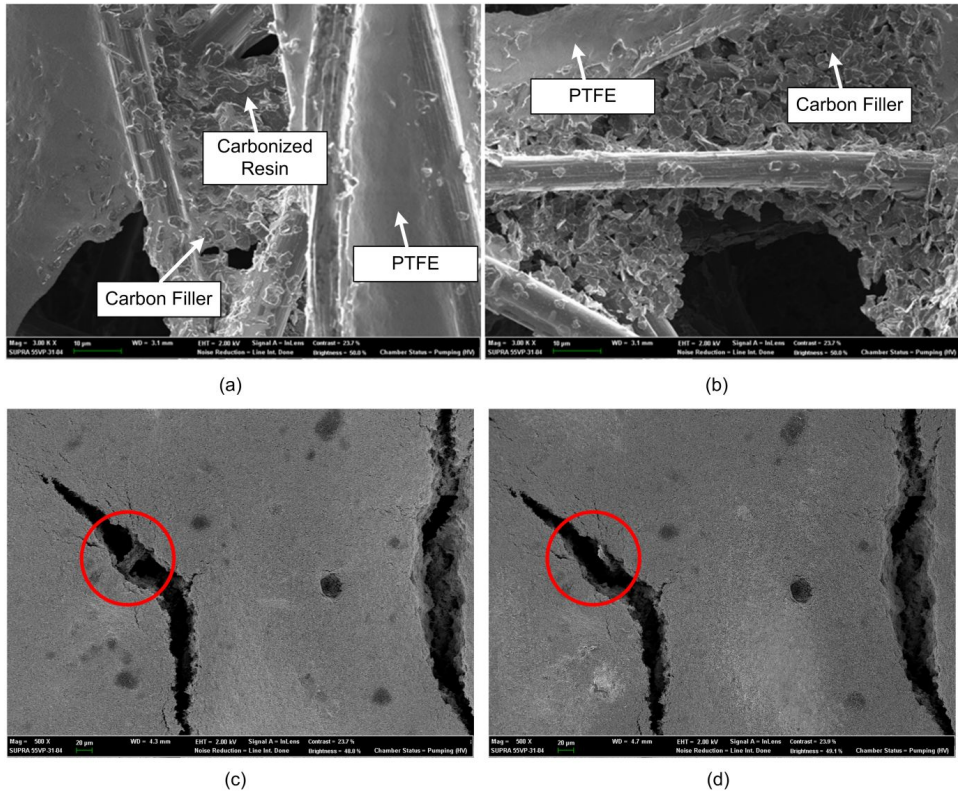


Figure 4.4 SEM image of loss of hydrophobic carbonized resins after the leaching test

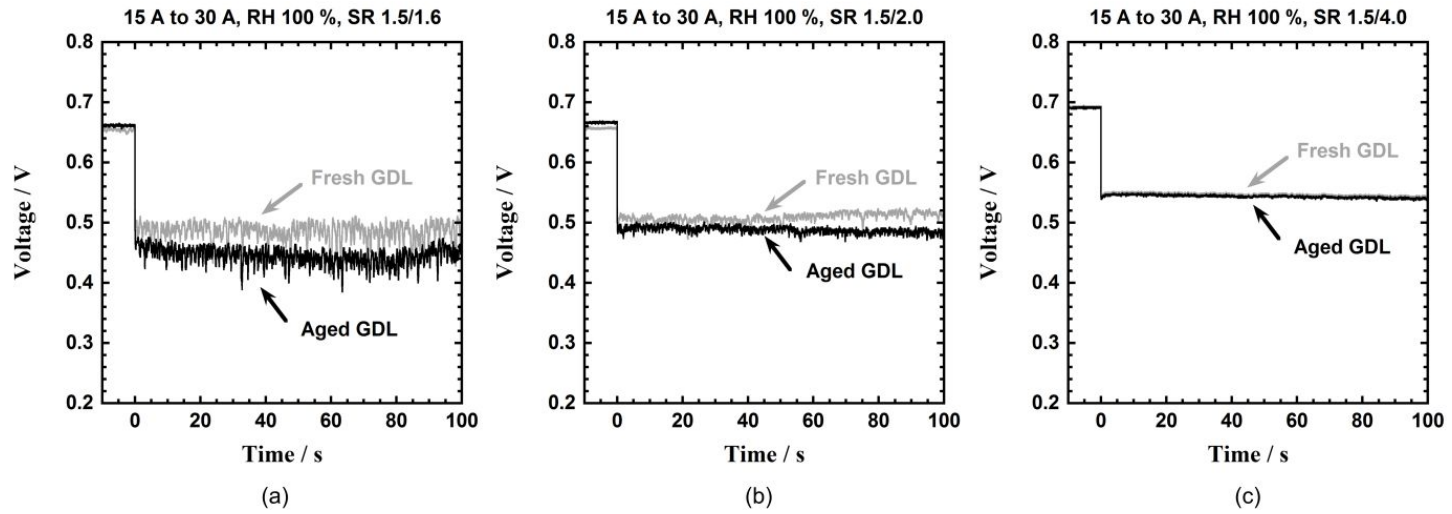


Figure 4.5 The voltage response as the current was changed from 15 A to 30 A at an RH of 100 % and an SR of H<sub>2</sub>/Air of (a) 1.5/1.6 (starved), (b) 1.5/2.0 (standard), and (c) 1.5/4.0 (excess)

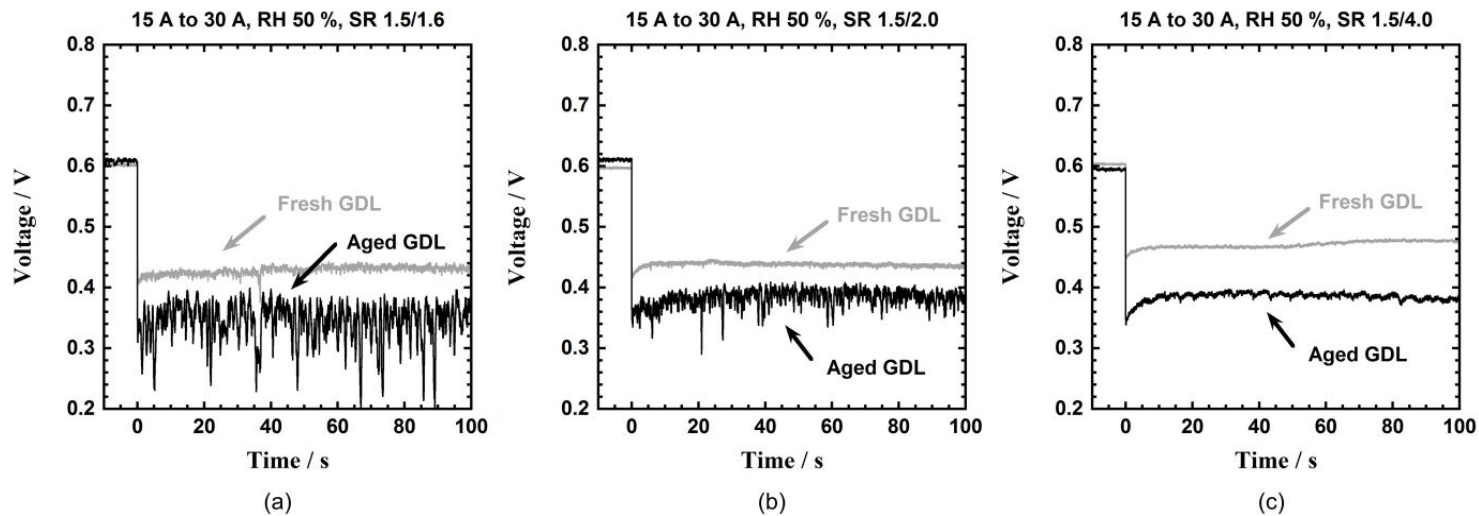


Figure 4.6 The voltage response as the current was changed from 15 A to 30 A at an RH of 50 % and an SR of H<sub>2</sub>/Air of (a) 1.5/1.6 (starved), (b) 1.5/2.0 (standard), and (c) 1.5/4.0 (excess)

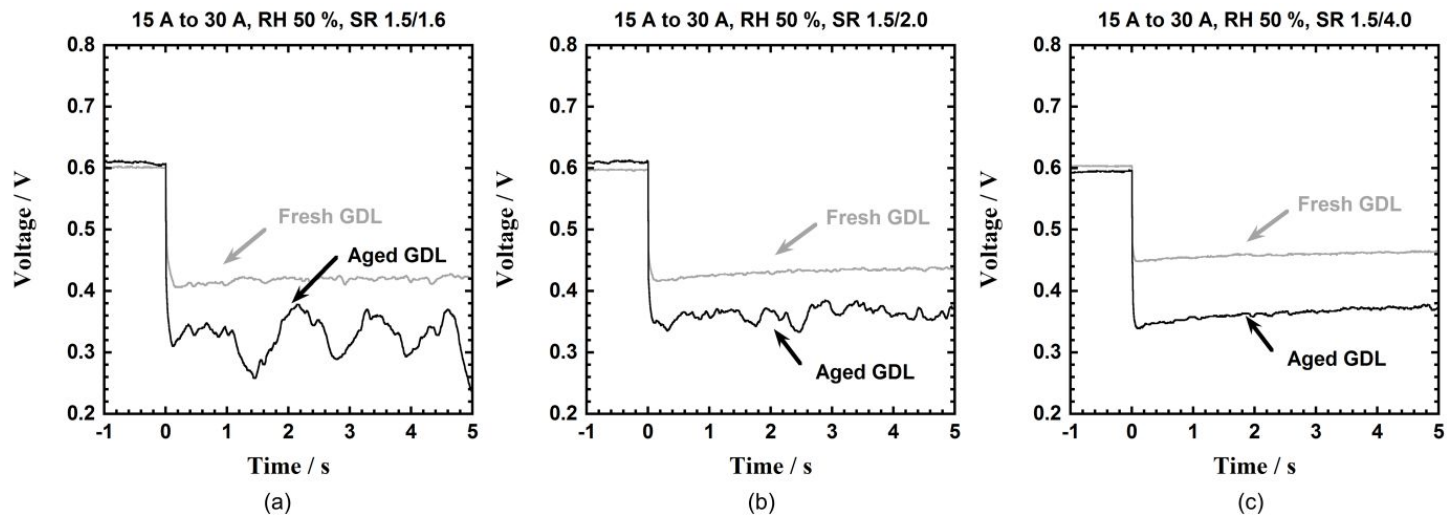


Figure 4.7 Enlarged area of Figure 4.6, which shows the change from 15 A to 30 A at an RH of 50 % and an SR of H<sub>2</sub>/Air of (a) 1.5/1.6 (starved), (b) 1.5/2.0 (standard), and (c) 1.5/4.0 (excess)

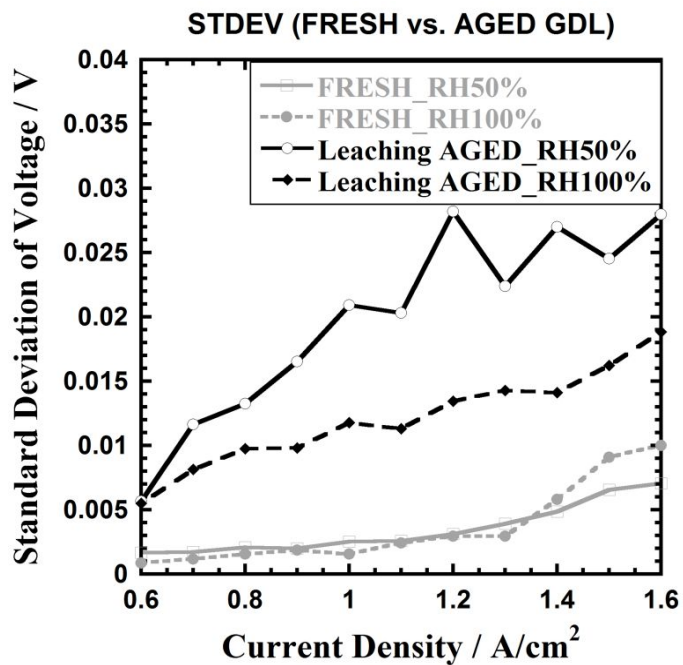


Figure 4.8 Standard deviation of the voltage as the current density was varied from 0.6 A/cm<sup>2</sup> to 1.6 A/cm<sup>2</sup> with fresh and aged GDLs at an RH of 50 and 100 % and an SR of H<sub>2</sub>/Air 1.5/2.0

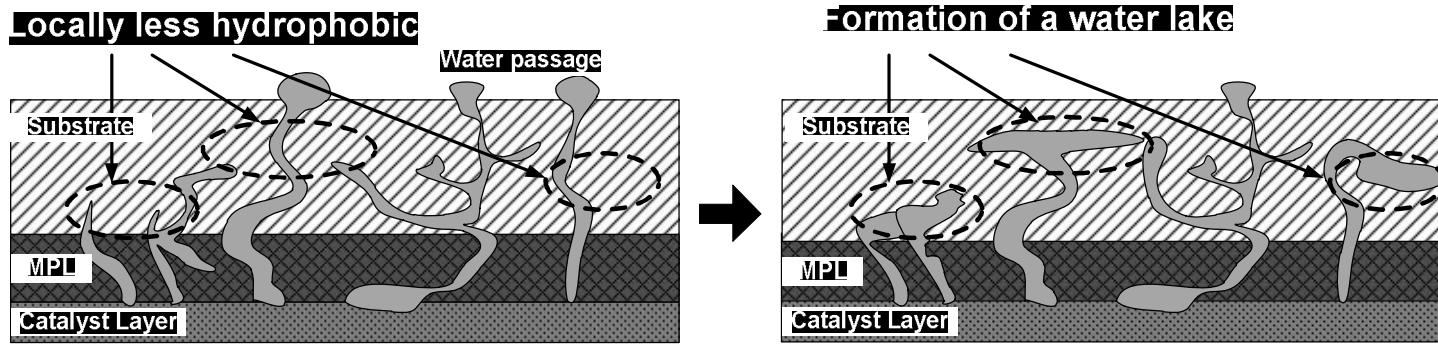


Figure 4.9 Schematic of local flooding in an aged GDL

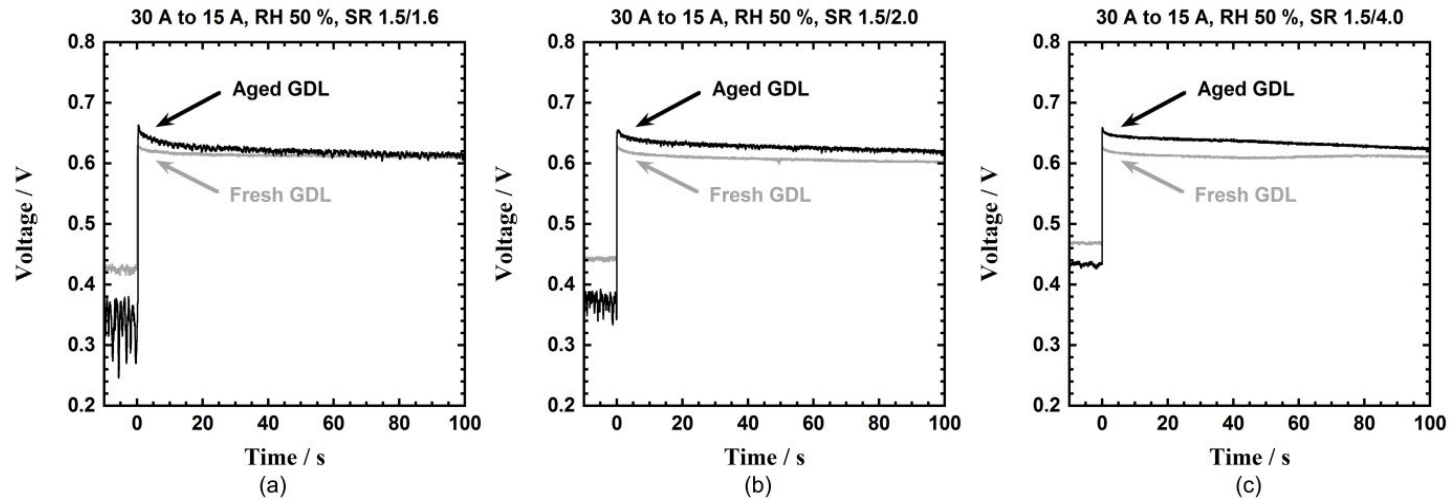
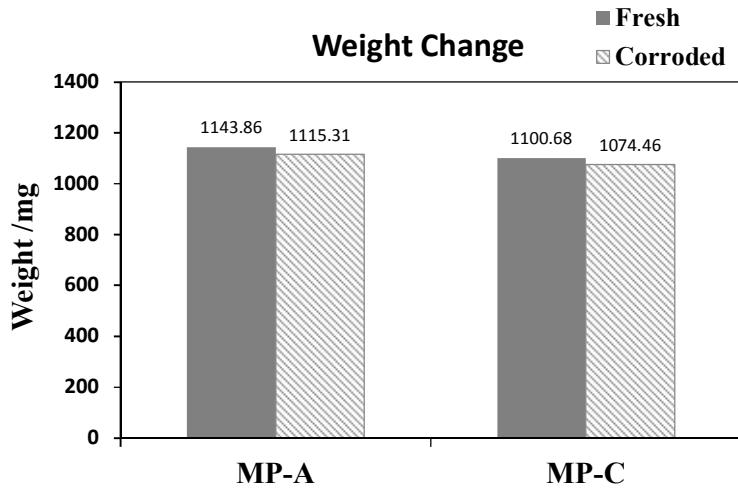
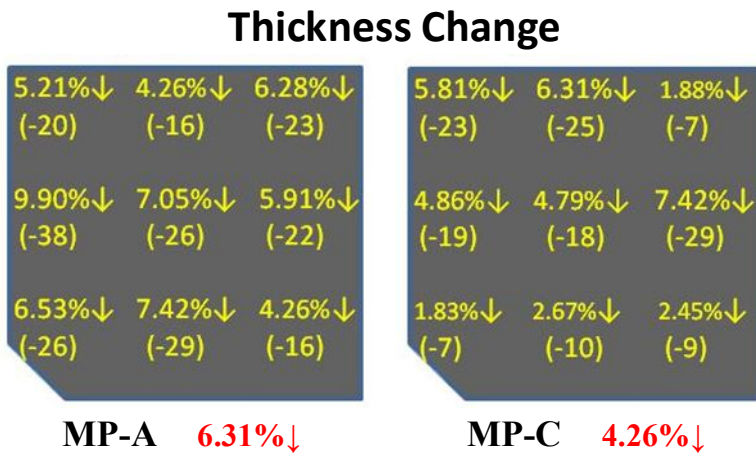


Figure 4.10 The voltage response as the current was changed from 30 A to 15 A at an RH of 50 % and an SR of H<sub>2</sub>/Air of (a) 1.5/1.6 (excess), (b) 1.5/2.0 (more excess), and (c) 1.5/4.0. (most excess)



(a)



(b)

Figure 4.11 Weight (a) and thickness (b) change after carbon corrosion for MP-A and MP-C

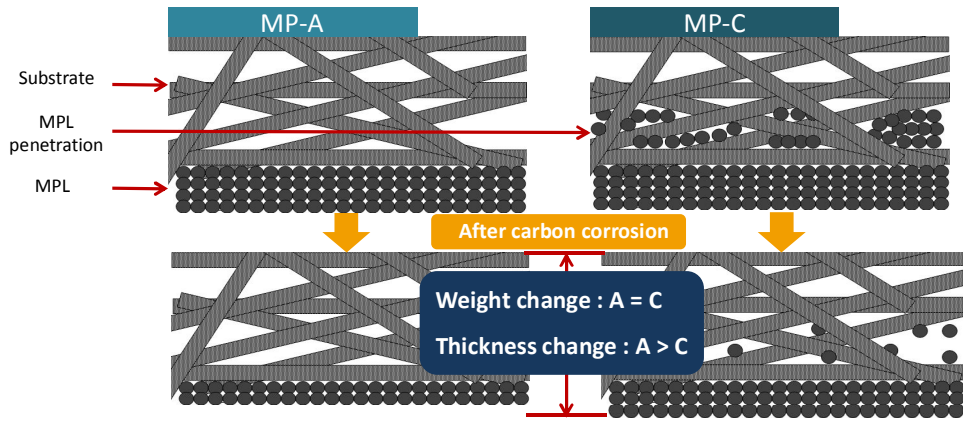
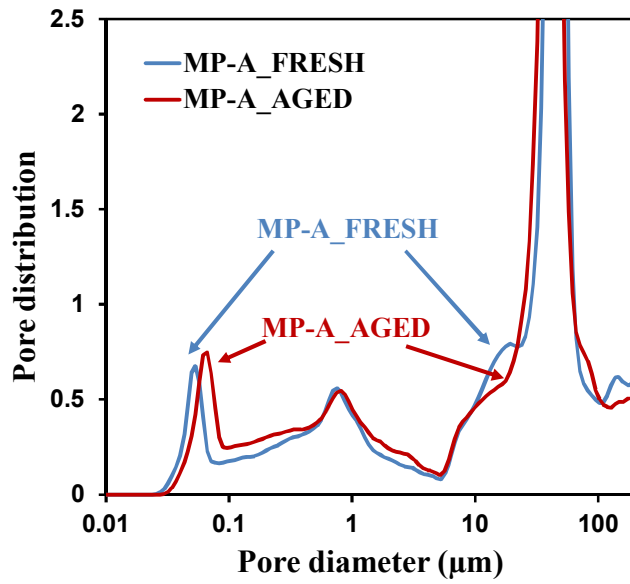
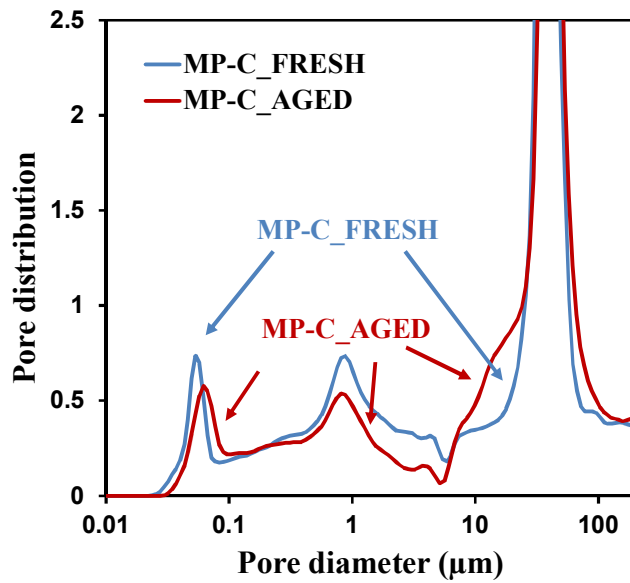


Figure 4.12 Schematic of carbon corrosion in the MPL penetration part



(a)



(b)

Figure 4.13 Pore distributions before/after carbon corrosion of MP-A (a) and MP-C

(b)

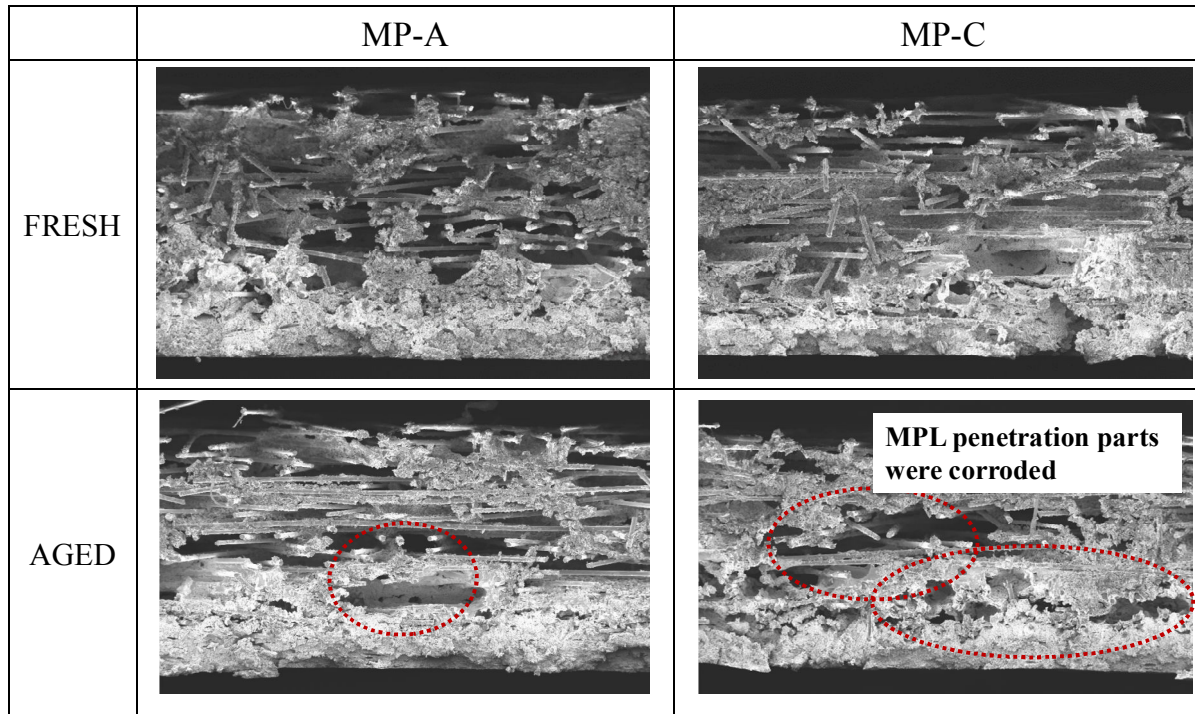
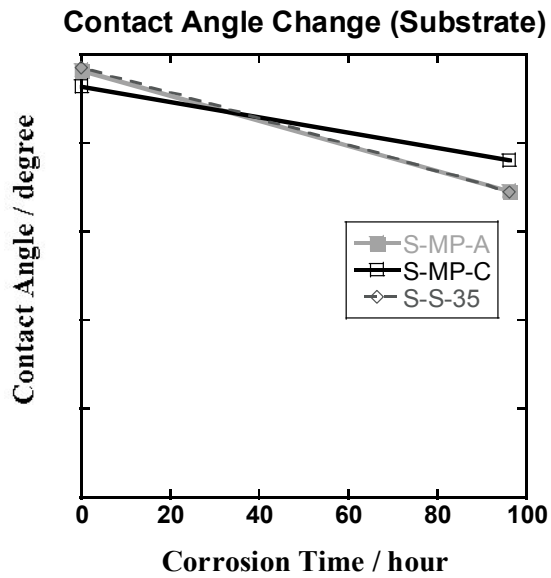
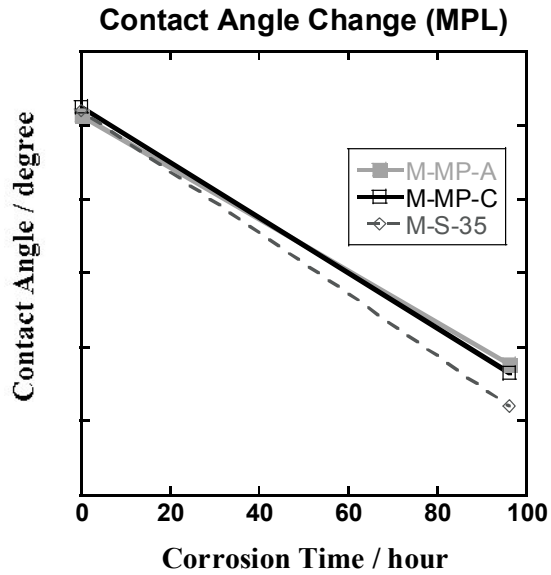


Figure 4.14 FESEM images before/after carbon corrosion of MP-A and MP-C



(a)



(b)

Figure 4.15 Contact angle changes before/after carbon corrosion of MP-A and MP-C on substrate surface (a) and MPL surface (b)

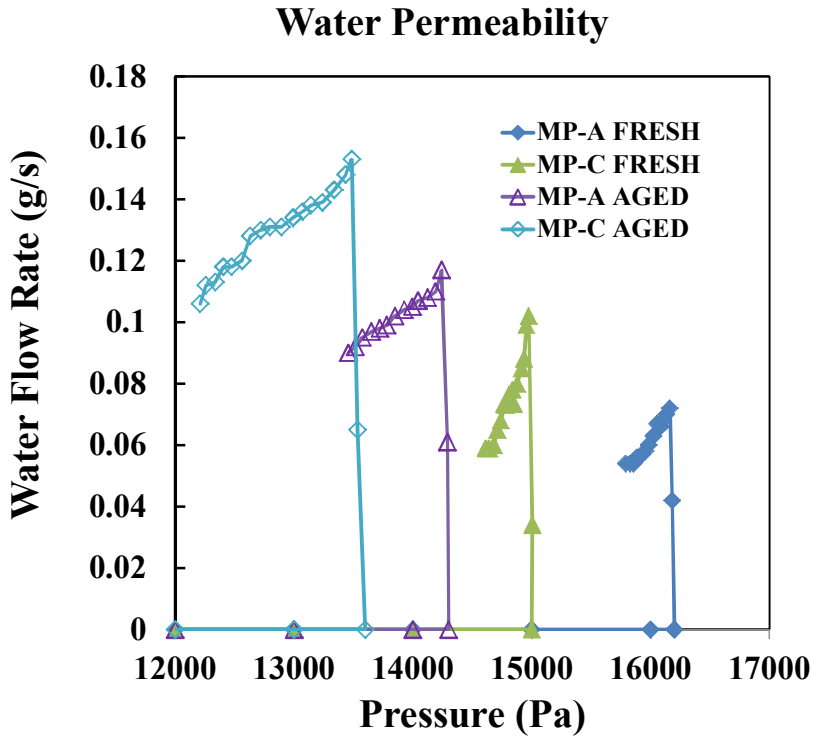
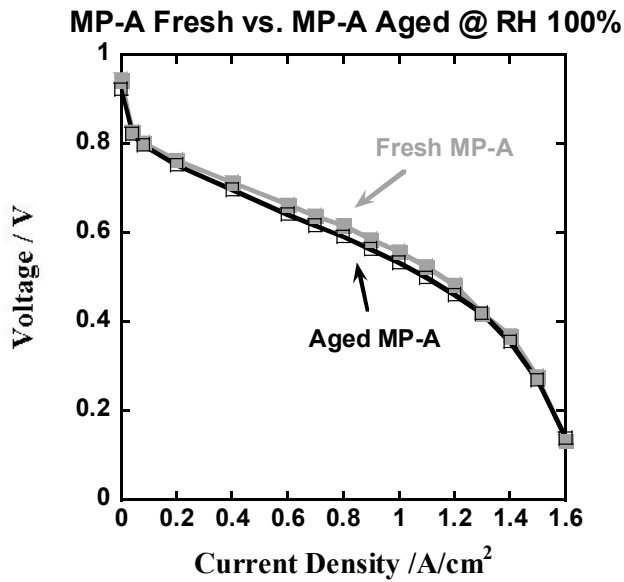
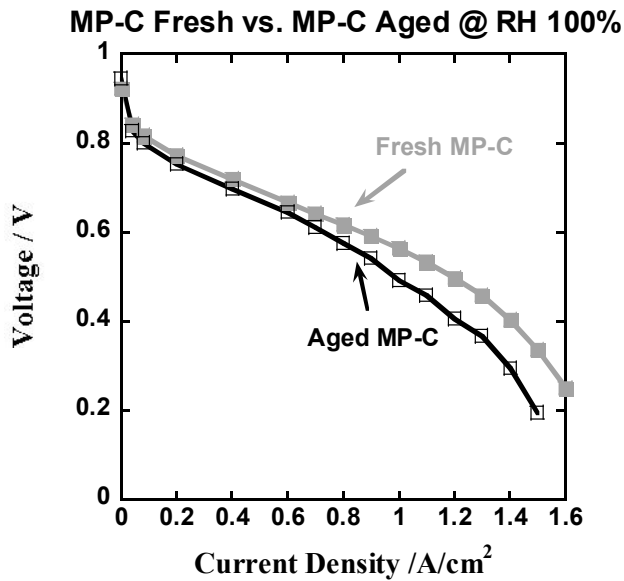


Figure 4.16 Water permeability change before/after carbon corrosion of MP-A and MP-C



(a)



(b)

Figure 4.17 Steady-state performance before/after carbon corrosion of MP-A and MP-C

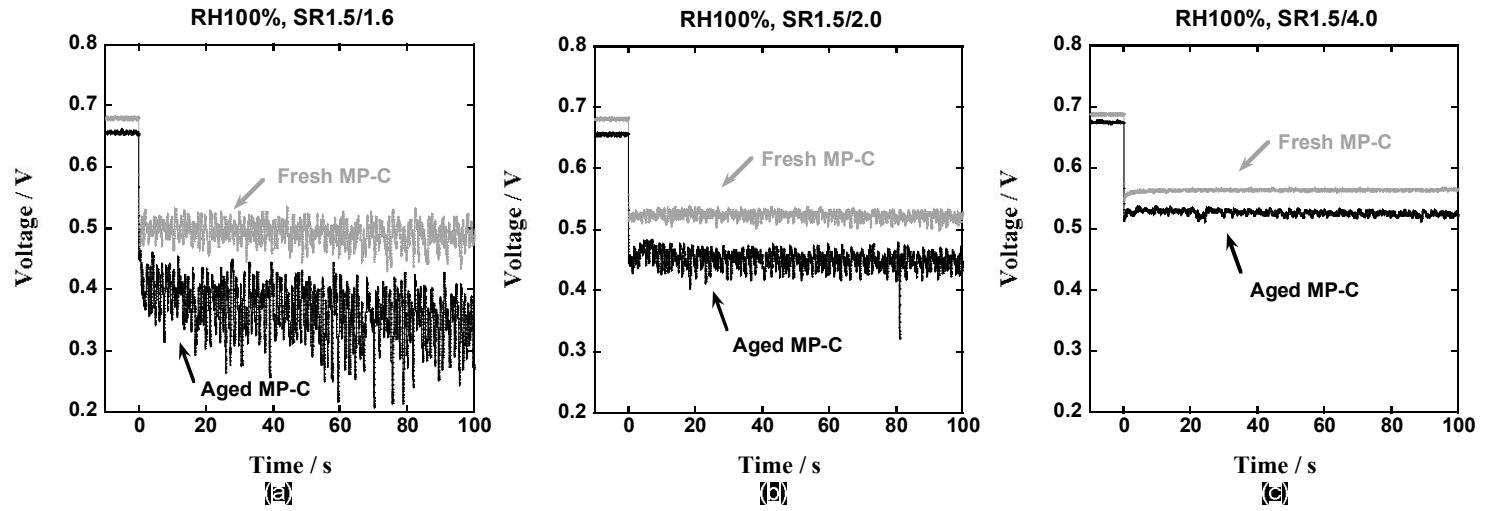


Figure 4.18 The voltage response of fresh MP-C and aged MP-C as the current was changed from 15 A to 30 A at an RH of 100 % and an SR of H<sub>2</sub>/Air of (a) 1.5/1.6 (starved), (b) 1.5/2.0 (standard), and (c) 1.5/4.0 (excess)

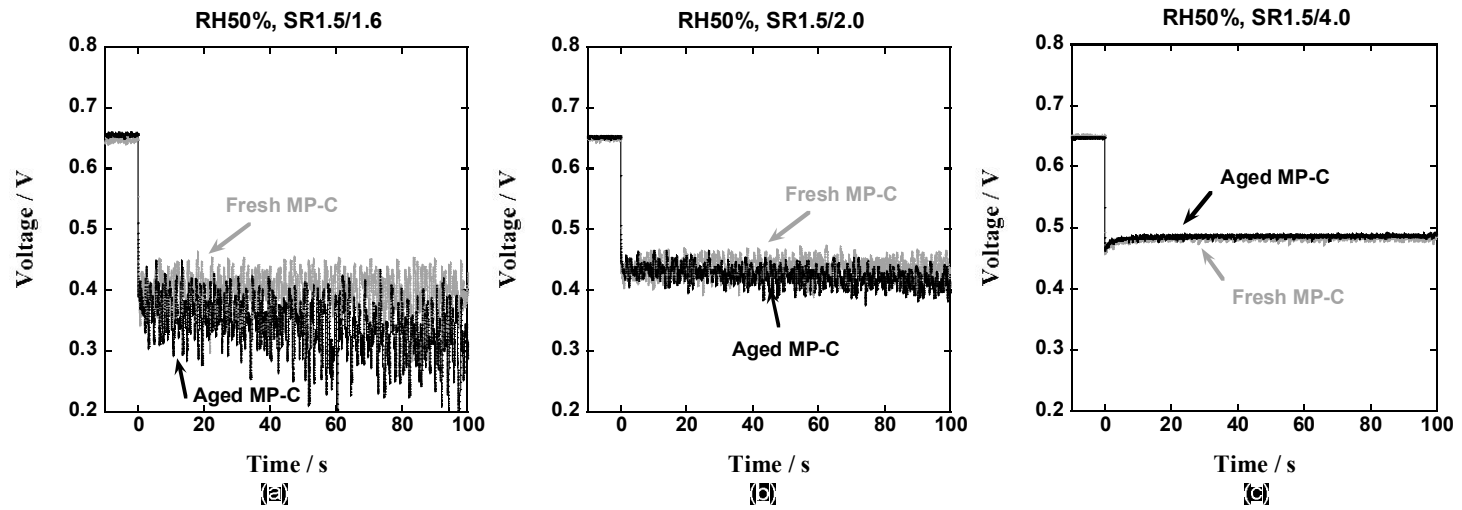


Figure 4.19 The voltage response of fresh MP-C and aged MP-C as the current was changed from 15 A to 30 A at an RH of 50 % and an SR of H<sub>2</sub>/Air of (a) 1.5/1.6 (starved), (b) 1.5/2.0 (standard), and (c) 1.5/4.0 (excess)

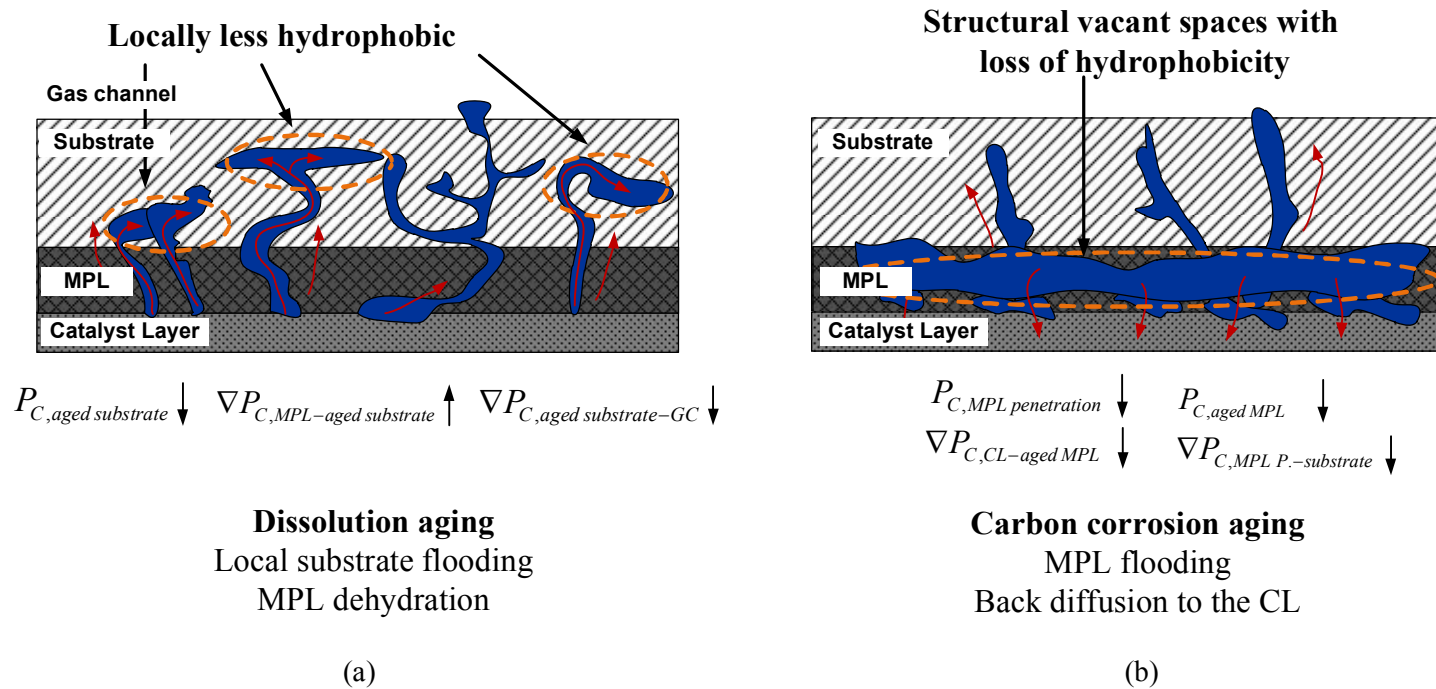


Figure 4.20 Schematic of water accumulation phenomena in the aged GDL due to (a) dissolution effect caused by leaching test and (b) carbon corrosion effect

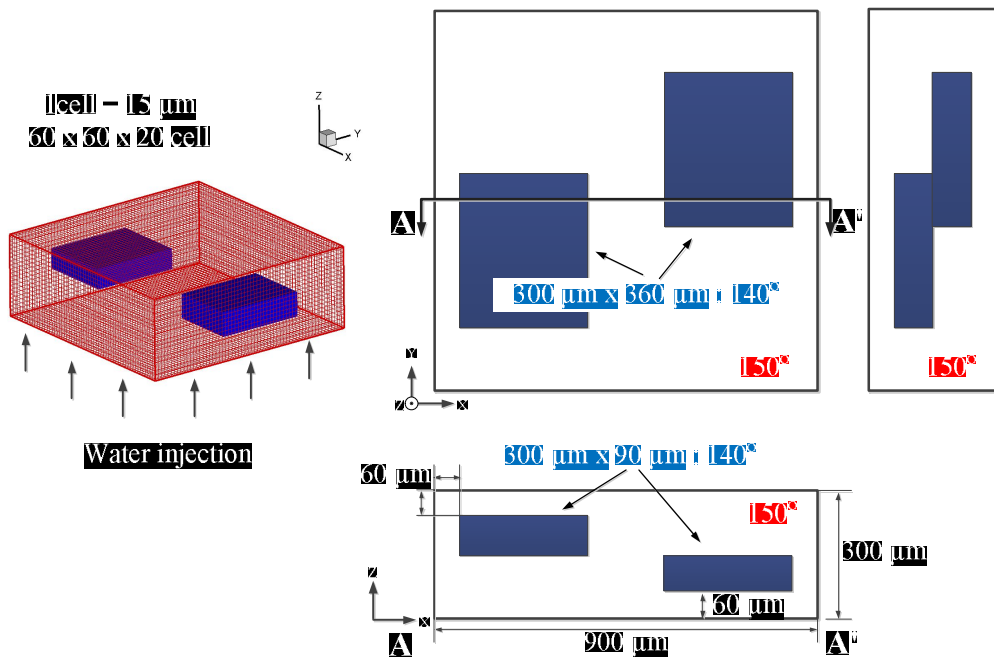


Figure 4.21 Calculation domain of the simulated aged GDL

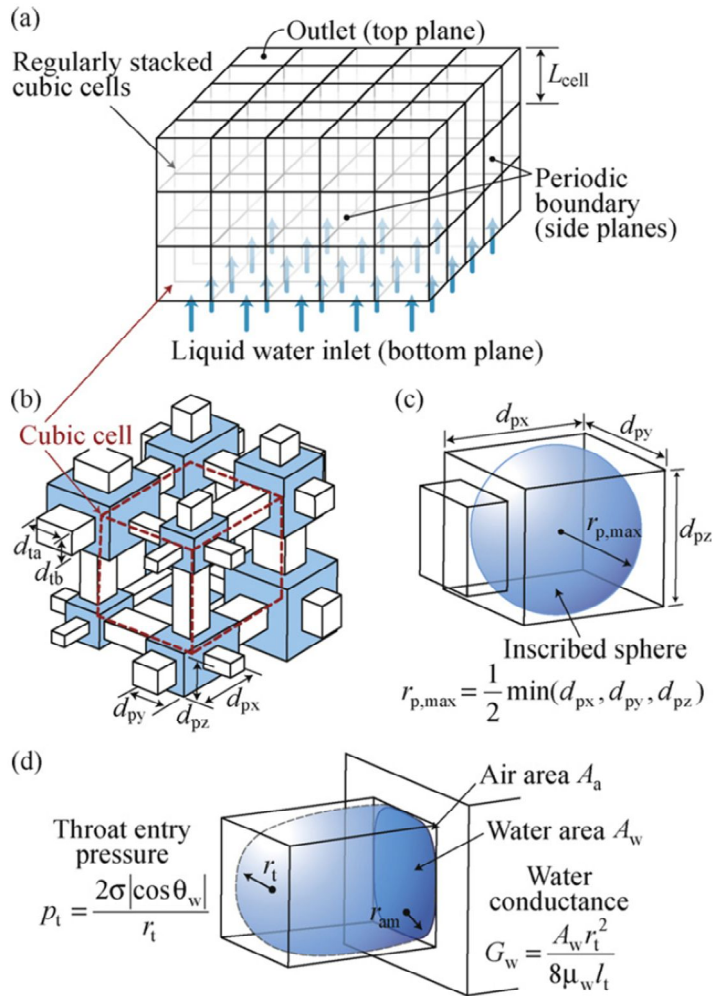


Figure 4.22 Pore-network generation: (a) regularly arranged cubic cells, (b) box-shaped pores and throats, (c) liquid water droplet in box-shaped pore, and (d) invading front of liquid water through hydrophobic rectangular throat [61]

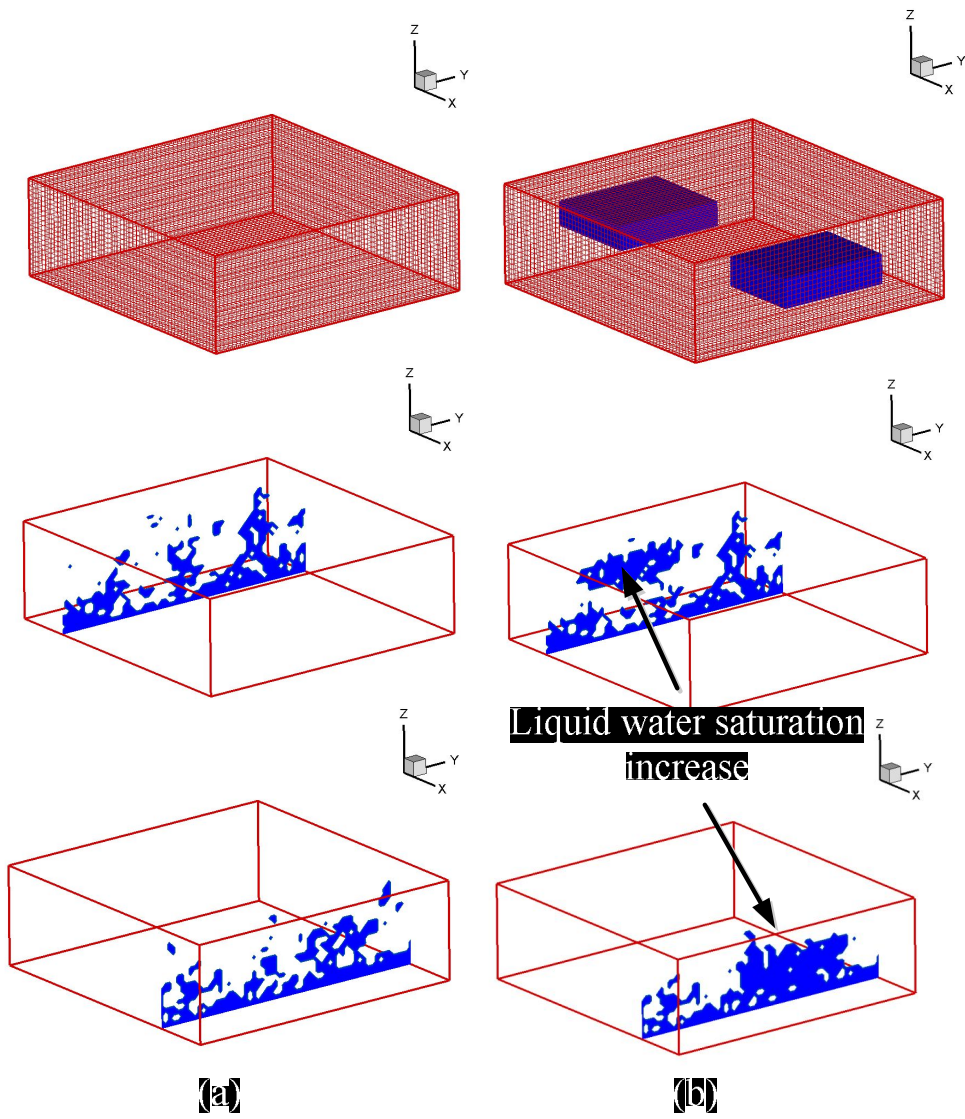


Figure 4.23 Simulation results of liquid water saturation distribution before (a)/after (b) aging of the GDL

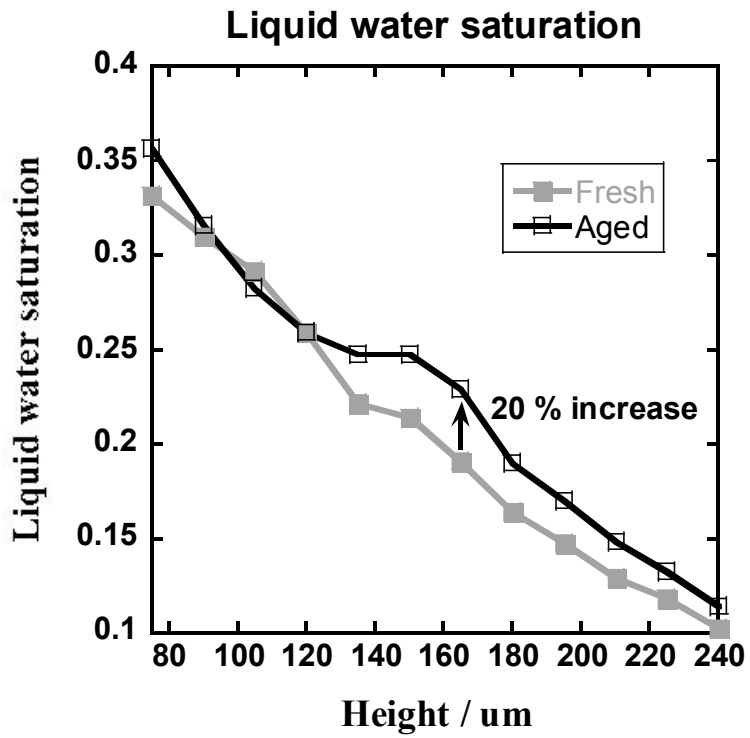


Figure 4.24 Liquid saturation changes of the xy-plane along z-coordinate before/after aging of the GDL

## Chapter 5. Conclusions

In this study, the transient response characteristic of the PEM fuel cell was systemically investigated considering operating conditions, structure of the GDL and characteristics change of the GDL.

In conclusion, when the PEM fuel cell operates at high loads suddenly, performance loss occurred because gases were instantaneously depleted and membrane became dehydrated which was induced by lots of electro-osmotic drag and internal product of heat from electrochemical reaction. And then, performance was recovered as membrane conductivity was recovered due to water supply from the GDL and water production at the cathode side. In this process, the GDL affected water flux between catalyst layer and gas channel, which were back-diffusion from the cathode side and electro-osmotic drag from the anode side. This water flux affected recovery of membrane water content, consequently, affected recovery characteristics of performance of the fuel cell. Gas diffusivity was also affected by water flux in the GDL. Water flux through the GDL was determined by capillary pressure gradient along the through-plane direction of the GDL, and this capillary pressure gradient was determined by design of structure of the GDL. In addition, capillary pressure gradient was changed by aging of the GDL, thereby transient response was also changed. This summary of the transient response is shown in Figure 5.1.

Conclusively remarkable investigations are:

1. In the case of low-load-to-high-load operation, undershoot was observed, and this response was divided into two stages. The first stage time delay, which is on the order of 0.1 ~ 1 second, is due to delay of oxygen supply, non-uniform oxygen distribution and cathode flooding. The first time delay was also verified by using cathode channel visualization and two-

phase relation of gas diffusivity in the GDL. Also, the second time delay, which is water content recovery time of the membrane, was on the order of 10 seconds. The second time delay was dominantly affected by cathode humidification condition which means back diffusion water flux is main cause of water content recovery in the membrane.

2. In the case of high-load-to-low-load operation, a fast response time of several seconds was obtained because a sufficiently hydrated membrane, active osmotic drag and back diffusion process, and better mass transfer were maintained during high-load operation.
3. The transient response was dominantly affected by characteristic of the GDL because the GDL determined gas supply and water flux of the PEM fuel cell. Water holding/removal ability of the GDL was key factor to the transient response, and holding ability was focused because low humidification operation is required in commercial application and undershoot characteristics is more dominant in low humidification condition, which means additional power sources have to compensate power loss of the PEM fuel cell in load change.
4. Water management characteristic of the GDL could be designed by controlling capillary pressure gradient through the GDL. Effects of diverse structure design on the transient response at both high and low humidification condition are summarized in Table 5.1.
5. The aging of the GDL induced deterioration of the transient response of the PEM fuel cell. The dissolution aging, which is a mechanical aging, induced decrease of hydrophobicity of the substrate because of loss of hydrophobic carbonized resin in the substrate. It induced local substrate flooding, thereby transient response was deteriorated at low humidification condition. On the other hand, chemical carbon corrosion

aging induced carbon loss of the MPL penetration part, thereby water was trapped in this region eventually induced MPL flooding. MPL flooding induced mass transport loss at high humidification condition.

This experimental research on the transient response of the PEM fuel cell related to the GDL shows correlation between characteristics of the GDL and dynamic performance of the PEM fuel cell which is difficult and clearly unknown problem. In addition, concept of GDL design is suggested and interpretation of performance degradation due to GDL aging is shown. This study contributes to the evaluation of design of GDL, fuel cell modeling, development of optimal cell design, and the construction of control logic and driving strategy for a fuel cell vehicle.

Table 5.1 Summary of GDL structure effects on the transient response of the PEM fuel cell

	Notation	Design parameter	Capillary pressure gradient	High RH	Low RH
Substrate	ACF10-60 ACF10-70	Increase of number density of macro pores	Extremely low $P_{C,Substrate}$ Extremely high $\nabla P_{C,Substrate}$ Extreme water removal	worse	worst
	ACF-5 ACF-10	Reducing number of relatively small macro pores (SMP)	Extremely high $P_{C,Substrate}$ Extremely low $\nabla P_{C,Substrate}$ Extreme water saturation	worst	better
	ACF-0	Coexistence of SMP and LMP	Water passage formed to LMP Water holding due to low $\nabla P_{C,MPL\ to\ SMP}$	best	best
MPL penetration	MP-A	Thin MPL penetration	Water saturation in the substrate due to low $\nabla P_{C,Substrate}$ MPL dehydration due to high $\nabla P_{C,MPL}$	worse	worse
	MP-C	Thick MPL penetration	Proper $\nabla P_{C,Substrate}$ and $\nabla P_{C,MPL}$ Proper water concentration in the MPL	best	best
MPL	MD-A	Dense MPL	Proper $\nabla P_{C,Substrate}$ and $\nabla P_{C,MPL}$ Proper water concentration in the MPL	best	better
	MD-B	Coarse MPL	Low $P_{C,coarse\ MPL}$ Water saturation in the substrate due to low $\nabla P_{C,Substrate}$ Low water flux to the membrane due to Low $P_{C,CL-coarse\ MPL}$	worse	worse

	MD-C	Substrate-Dense-Coarse-CL structure	Reverse gradient $\nabla P_{C,Coarse-Dense}$ Increase of water content in the MPL Slight mass transport resistance	better	best
	MF-A	Reference	Proper $\nabla P_{C,Substrate}$ and $\nabla P_{C,MPL}$ Proper water concentration in the MPL	best	plain
	MF-B	Less hydrophobic layer	Low $P_{C,LHL}$ Low $\nabla P_{C,Substrate}$ , $\nabla P_{C,HL}$ Water holding in the HL and LHL Slight mass transport resistance	a little worse	best
	MF-C	LHL + Pore path	Low $P_{C,LHL}$ , $P_{C,HL}$ due to pore path Low $\nabla P_{C,Substrate}$ , $\nabla P_{C,HL}$ Water holding in the HL and LHL Slight mass transport resistance Low water flux to the membrane due to low $P_{C,CL-HL}$	a little worse	better
GDL aging	Dissolution Loss of hydrophobicity both MPL surface and inside the substrate		Low $P_{C,aged\ substrate}$ , Low $P_{C,CL-aged\ MPL}$ Locally high $\nabla P_{C,MPL-aged\ substrate}$ Low $\nabla P_{C,aged\ substrate-GC}$ Local substrate flooding MPL dehydration	worse	worst
	Carbon Corrosion Vacant spaces at the MPL penetration part		Low $P_{C,aged\ substrate}$ , Extremely low $P_{C,CL-aged\ MPL}$ Low $\nabla P_{C,MPL-aged\ MPL\ penetration}$ MPL flooding Water flux to the membrane	worst	worse

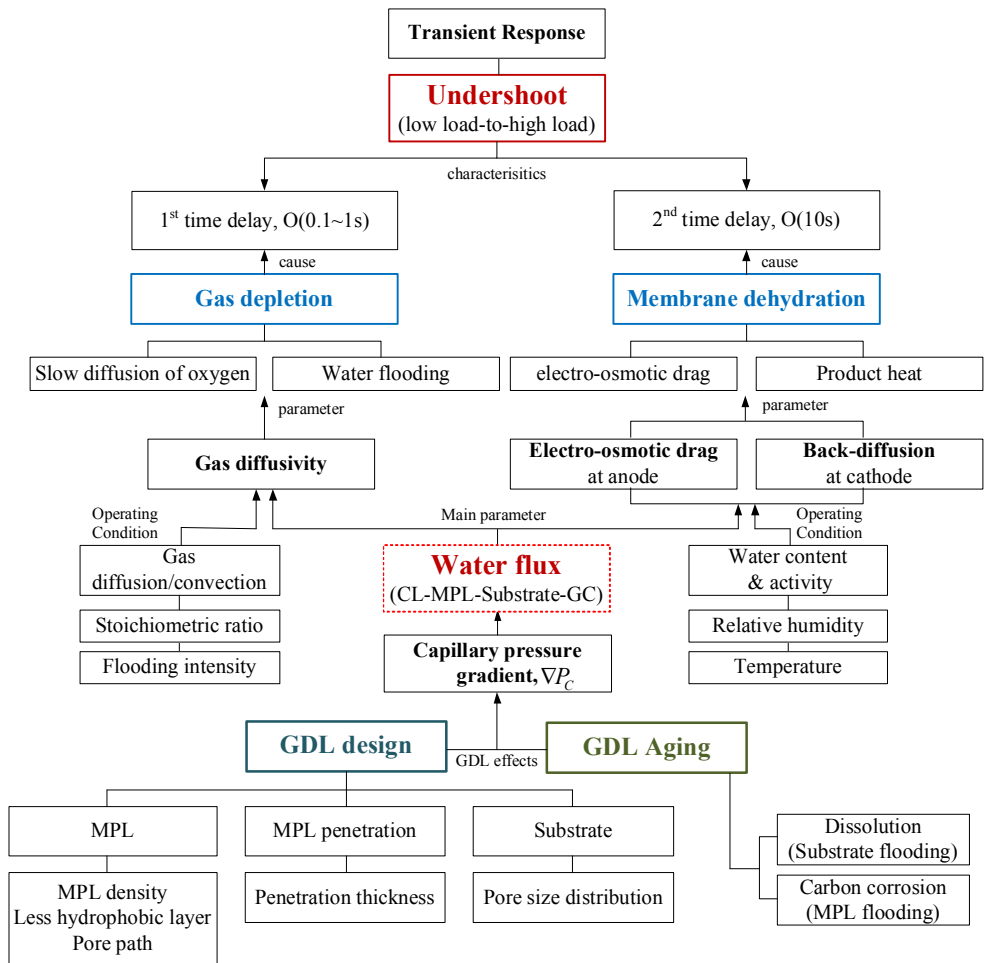


Figure 5.1 Summary of the transient response of the PEM fuel cell

## Bibliography

- [1] Larminie J, Dicks A, . K. Fuel cell systems explained. 2003.
- [2] Automotive World Car Industry Forecast Report. Global Insight; 2004.
- [3] Dai W, Wang H, Yuan XZ, Martin JJ, Yang D, Qiao J, et al. A review on water balance in the membrane electrode assembly of proton exchange membrane fuel cells. *International Journal of Hydrogen Energy*. 2009;34:9461-78.
- [4] O'Hayre RP, Cha SW, Colella W, Prinz FB. Fuel cell fundamentals: John Wiley & Sons Hoboken, New Jersey; 2006.
- [5] Kang S, Min K, Yu S. Two dimensional dynamic modeling of a shell-and-tube water-to-gas membrane humidifier for proton exchange membrane fuel cell. *International Journal of Hydrogen Energy*. 2010;35:1727-41.
- [6] Kang S, Min K, Yu S. Dynamic modeling of a proton exchange membrane fuel cell system with a shell-and-tube gas-to-gas membrane humidifier. *International Journal of Hydrogen Energy*. 2012.
- [7] Lee D, Bae J. Visualization of flooding in a single cell and stacks by using a newly-designed transparent PEMFC. *International Journal of Hydrogen Energy*. 2011.
- [8] Blanco M, Wilkinson DP, Wang H. Application of water barrier layers in a proton exchange membrane fuel cell for improved water management at low humidity conditions. *International Journal of Hydrogen Energy*. 2011.
- [9] Su A, Weng FB, Hsu CY, Chen YM. Studies on flooding in PEM fuel cell cathode channels. *International Journal of Hydrogen Energy*. 2006;31:1031-9.
- [10] Garland NL. US DOE fuel cell activities. Electric drive transportation association conference and exposition 2008.
- [11] Cindrella L, Kannan A, Lin J, Saminathan K, Ho Y, Lin C, et al. Gas diffusion layer for proton exchange membrane fuel cells—A review. *Journal of Power Sources*. 2009;194:146-60.

- [12] Li H, Tang Y, Wang Z, Shi Z, Wu S, Song D, et al. A review of water flooding issues in the proton exchange membrane fuel cell. *Journal of Power Sources*. 2008;178:103-17.
- [13] Williams MV, Begg E, Bonville L, Kunz HR, Fenton JM. Characterization of gas diffusion layers for PEMFC. *Journal of the Electrochemical Society*. 2004;151:A1173.
- [14] Ha T, Kim B, Kim HS, Min K. Investigation on the liquid water droplet instability in a simulated flow channel of PEM fuel cell. *Journal of Mechanical Science and Technology*. 2008;22:1030-6.
- [15] Park S, Lee JW, Popov BN. A review of gas diffusion layer in PEM fuel cells: Materials and designs. *International Journal of Hydrogen Energy*. 2012.
- [16] Ceraolo M, Miulli C, Pozio A. Modelling static and dynamic behaviour of proton exchange membrane fuel cells on the basis of electro-chemical description. *Journal of Power Sources*. 2003;113:131-44.
- [17] Shan Y, Choe SY. A high dynamic PEM fuel cell model with temperature effects. *Journal of Power Sources*. 2005;145:30-9.
- [18] Song D, Wang Q, Liu ZS, Huang C. Transient analysis for the cathode gas diffusion layer of PEM fuel cells. *Journal of Power Sources*. 2006;159:928-42.
- [19] Wang Y, Wang CY. Transient analysis of polymer electrolyte fuel cells. *Electrochimica Acta*. 2005;50:1307-15.
- [20] Wang Y, Wang CY. Dynamics of polymer electrolyte fuel cells undergoing load changes. *Electrochimica Acta*. 2006;51:3924-33.
- [21] Wang Y, Wang CY. Two-phase transients of polymer electrolyte fuel cells. *Journal of the Electrochemical Society*. 2007;154:B636.
- [22] Wang Y. Modeling of two-phase transport in the diffusion media of polymer electrolyte fuel cells. *Journal of Power Sources*. 2008;185:261-71.
- [23] Yan WM, Soong CY, Chen F, Chu HS. Transient analysis of reactant gas transport and performance of PEM fuel cells. *Journal of Power Sources*. 2005;143:48-56.

- [24] Shimpalee S, Lee WK, Van Zee J, Naseri-Neshat H. Predicting the transient response of a serpentine flow-field PEMFC: I. Excess to normal fuel and air. *Journal of Power Sources*. 2006;156:355-68.
- [25] Shimpalee S, Lee WK, Van Zee JW, Naseri-Neshat H. Predicting the transient response of a serpentine flow-field PEMFC: II: Normal to minimal fuel and AIR. *Journal of Power Sources*. 2006;156:369-74.
- [26] Shimpalee S, Spuckler D, Van Zee J. Prediction of transient response for a 25-cm<sup>2</sup> PEM fuel cell. *Journal of Power Sources*. 2007;167:130-8.
- [27] Kumar A, Reddy RG. Effect of gas flow-field design in the bipolar/end plates on the steady and transient state performance of polymer electrolyte membrane fuel cells. *Journal of Power Sources*. 2006;155:264-71.
- [28] Mueller F, Brouwer J, Kang S, Kim HS, Min K. Quasi-three dimensional dynamic model of a proton exchange membrane fuel cell for system and controls development. *Journal of Power Sources*. 2007;163:814-29.
- [29] Kang S, Min K, Mueller F, Brouwer J. Configuration effects of air, fuel, and coolant inlets on the performance of a proton exchange membrane fuel cell for automotive applications. *International Journal of Hydrogen Energy*. 2009;34:6749-64.
- [30] Hou Y, Yang Z, Wan G. An improved dynamic voltage model of PEM fuel cell stack. *International Journal of Hydrogen Energy*. 2010;35:11154-60.
- [31] Ning Q, Xuan D, Kim Y. Modeling and control strategy development for fuel cell hybrid vehicles. *International Journal of Automotive Technology*. 2010;11:229-38.
- [32] Qu S, Li X, Ke C, Shao ZG, Yi B. Experimental and modeling study on water dynamic transport of the proton exchange membrane fuel cell under transient air flow and load change. *Journal of Power Sources*. 2010;195:6629-36.
- [33] Khajeh-Hosseini-Dalasm N, Fushinobu K, Okazaki K. Three-dimensional transient two-phase study of the cathode side of a PEM fuel cell. *International Journal of Hydrogen Energy*. 2010;35:4234-46.

- [34] Loo K, Wong K, Tan S, Lai Y, Tse CK. Characterization of the dynamic response of proton exchange membrane fuel cells-A numerical study. *International Journal of Hydrogen Energy*. 2010;35:11861-77.
- [35] Kim S, Shimpalee S, Van Zee J. The effect of stoichiometry on dynamic behavior of a proton exchange membrane fuel cell (PEMFC) during load change. *Journal of Power Sources*. 2004;135:110-21.
- [36] Kim S, Shimpalee S, Van Zee J. The effect of reservoirs and fuel dilution on the dynamic behavior of a PEMFC. *Journal of Power Sources*. 2004;137:43-52.
- [37] Kim S, Shimpalee S, Van Zee J. Effect of flow field design and voltage change range on the dynamic behavior of PEMFCs. *Journal of the Electrochemical Society*. 2005;152:A1265.
- [38] Yan Q, Toghiani H, Causey H. Steady state and dynamic performance of proton exchange membrane fuel cells (PEMFCs) under various operating conditions and load changes. *Journal of Power Sources*. 2006;161:492-502.
- [39] Weydahl H, Møller-Holst S, Hagen G, Børresen B. Transient response of a proton exchange membrane fuel cell. *Journal of Power Sources*. 2007;171:321-30.
- [40] Takaichi S, Uchida H, Watanabe M. Response of specific resistance distribution in electrolyte membrane to load change at PEFC operation. *Journal of the Electrochemical Society*. 2007;154:B1373.
- [41] Tang Y, Yuan W, Pan M, Li Z, Chen G, Li Y. Experimental investigation of dynamic performance and transient responses of a kW-class PEM fuel cell stack under various load changes. *Applied Energy*. 2010;87:1410-7.
- [42] Bevers D, Rogers R, Von Bradke M. Examination of the influence of PTFE coating on the properties of carbon paper in polymer electrolyte fuel cells. *Journal of Power Sources*. 1996;63:193-201.
- [43] Ioroi T, Oku T, Yasuda K, Kumagai N, Miyazaki Y. Influence of PTFE coating on gas diffusion backing for unitized regenerative polymer electrolyte fuel cells. *Journal of Power Sources*. 2003;124:385-9.

- [44] Lim C, Wang C. Effects of hydrophobic polymer content in GDL on power performance of a PEM fuel cell. *Electrochimica Acta*. 2004;49:4149-56.
- [45] Park GG, Sohn YJ, Yang TH, Yoon YG, Lee WY, Kim CS. Effect of PTFE contents in the gas diffusion media on the performance of PEMFC. *Journal of Power Sources*. 2004;131:182-7.
- [46] Park S, Popov BN. Effect of cathode GDL characteristics on mass transport in PEM fuel cells. *Fuel*. 2009;88:2068-73.
- [47] Park S, Popov BN. Effect of hydrophobicity and pore geometry in cathode GDL on PEM fuel cell performance. *Electrochimica Acta*. 2009;54:3473-9.
- [48] Liu CH, Ko TH, Chang EC, Lyu HD, Liao YK. Effect of carbon fiber paper made from carbon felt with different yard weights on the performance of low temperature proton exchange membrane fuel cells. *Journal of Power Sources*. 2008;180:276-82.
- [49] Park S, Popov BN. Effect of a GDL based on carbon paper or carbon cloth on PEM fuel cell performance. *Fuel*. 2011;90:436-40.
- [50] Wang Y, Wang CY, Chen K. Elucidating differences between carbon paper and carbon cloth in polymer electrolyte fuel cells. *Electrochimica Acta*. 2007;52:3965-75.
- [51] Qi Z, Kaufman A. Improvement of water management by a microporous sublayer for PEM fuel cells. *Journal of Power Sources*. 2002;109:38-46.
- [52] Weber AZ, Newman J. Effects of microporous layers in polymer electrolyte fuel cells. *Journal of the Electrochemical Society*. 2005;152:A677.
- [53] Chun JH, Park KT, Jo DH, Lee JY, Kim SG, Lee ES, et al. Determination of the pore size distribution of micro porous layer in PEMFC using pore forming agents under various drying conditions. *International Journal of Hydrogen Energy*. 2010;35:11148-53.
- [54] Chun JH, Park KT, Jo DH, Lee JY, Kim SG, Park SH, et al. Development of a novel hydrophobic/hydrophilic double micro porous layer for use in a cathode gas diffusion layer in PEMFC. *International Journal of Hydrogen Energy*. 2011.

- [55] Weng FB, Hsu CY, Su MC. Experimental study of micro-porous layers for PEMFC with gradient hydrophobicity under various humidity conditions. *International Journal of Hydrogen Energy*. 2011.
- [56] Tang H, Wang S, Pan M, Yuan R. Porosity-graded micro-porous layers for polymer electrolyte membrane fuel cells. *Journal of Power Sources*. 2007;166:41-6.
- [57] Manahan M, Hatzell M, Kumbur E, Mench M. Laser perforated fuel cell diffusion media. Part I: Related changes in performance and water content. *Journal of Power Sources*. 2011;196:5573-82.
- [58] Zhang F-Y, Advani SG, Prasad AK. Performance of a metallic gas diffusion layer for PEM fuel cells. *Journal of Power Sources*. 2008;176:293-8.
- [59] Santamaria A, Tang HY, Park JW, Park GG, Sohn YJ. 3D neutron tomography of a polymer electrolyte membrane fuel cell under sub-zero conditions. *International Journal of Hydrogen Energy*. 2012.
- [60] Lee KJ, Nam JH, Kim CJ. Pore-network analysis of two-phase water transport in gas diffusion layers of polymer electrolyte membrane fuel cells. *Electrochimica Acta*. 2009;54:1166-76.
- [61] Lee KJ, Nam JH, Kim CJ. Steady saturation distribution in hydrophobic gas-diffusion layers of polymer electrolyte membrane fuel cells: A pore-network study. *Journal of Power Sources*. 2010;195:130-41.
- [62] Luo G, Ji Y, Wang CY, Sinha PK. Modeling liquid water transport in gas diffusion layers by topologically equivalent pore network. *Electrochimica Acta*. 2010;55:5332-41.
- [63] Sinha PK, Wang CY. Pore-network modeling of liquid water transport in gas diffusion layer of a polymer electrolyte fuel cell. *Electrochimica Acta*. 2007;52:7936-45.
- [64] Wu R, Zhu X, Liao Q, Wang H, Ding Y, Li J, et al. A pore network study on the role of micro-porous layer in control of liquid water distribution in gas diffusion layer. *International Journal of Hydrogen Energy*. 2010;35:7588-93.

- [65] Wu R, Zhu X, Liao Q, Wang H, Ding Y, Li J, et al. A pore network study on water distribution in bi-layer gas diffusion media: Effects of inlet boundary condition and micro-porous layer properties. *International Journal of Hydrogen Energy*. 2010;35:9134-43.
- [66] Hao L, Cheng P. Lattice Boltzmann simulations of liquid droplet dynamic behavior on a hydrophobic surface of a gas flow channel. *Journal of Power Sources*. 2009;190:435-46.
- [67] Hao L, Cheng P. Lattice Boltzmann simulations of water transport in gas diffusion layer of a polymer electrolyte membrane fuel cell. *Journal of Power Sources*. 2010;195:3870-81.
- [68] Park J, Matsubara M, Li X. Application of lattice Boltzmann method to a micro-scale flow simulation in the porous electrode of a PEM fuel cell. *Journal of Power Sources*. 2007;173:404-14.
- [69] Pauchet J, Prat M, Schott P, Kuttanikkad SP. Performance loss of proton exchange membrane fuel cell due to hydrophobicity loss in gas diffusion layer: Analysis by multiscale approach combining pore network and performance modelling. *International Journal of Hydrogen Energy*. 2011.
- [70] Tabe Y, Lee Y, Chikahisa T, Kozakai M. Numerical simulation of liquid water and gas flow in a channel and a simplified gas diffusion layer model of polymer electrolyte membrane fuel cells using the lattice Boltzmann method. *Journal of Power Sources*. 2009;193:24-31.
- [71] Ahluwalia RK, Wang X. Fuel cell systems for transportation: Status and trends. *Journal of Power Sources*. 2008;177:167-76.
- [72] Marcinkoski J, Kopasz JP, Benjamin TG. Progress in the US DOE fuel cell subprogram efforts in polymer electrolyte fuel cells. *International Journal of Hydrogen Energy*. 2008;33:3894-902.
- [73] Borup RL, Davey JR, Wood DL, Garzon FH, Inbody MA, D. G. PEM fuel cell durability. DOE Hydrogen Program FY 2004 Progress Report; 2004.

- [74] Wu J, Yuan XZ, Martin JJ, Wang H, Zhang J, Shen J, et al. A review of PEM fuel cell durability: Degradation mechanisms and mitigation strategies. *Journal of Power Sources*. 2008;184:104-19.
- [75] Borup RL, Davey JR, Wood DL, Garzon FH, Inbody MA, P. W. PEM Fuel Cell Durability. DOE Hydrogen Program FY 2006 Annual Progress Report; 2006.
- [76] Lim SJ, Park GG, Park JS, Sohn YJ, Yim SD, Yang TH, et al. Investigation of freeze/thaw durability in polymer electrolyte fuel cells. *International Journal of Hydrogen Energy*. 2010;35:13111-7.
- [77] Luo M, Huang C, Liu W, Luo Z, Pan M. Degradation behaviors of polymer electrolyte membrane fuel cell under freeze/thaw cycles. *International Journal of Hydrogen Energy*. 2010;35:2986-93.
- [78] Kang J, Jung DW, Park S, Lee JH, Ko J, Kim J. Accelerated test analysis of reversal potential caused by fuel starvation during PEMFCs operation. *International Journal of Hydrogen Energy*. 2010;35:3727-35.
- [79] Lim KH, Oh HS, Jang SE, Ko YJ, Kim HJ, Kim H. Effect of operating conditions on carbon corrosion in polymer electrolyte membrane fuel cells. *Journal of Power Sources*. 2009;193:575-9.
- [80] Reiser CA, Bregoli L, Patterson TW, Jung SY, Yang JD, Perry ML, et al. A reverse-current decay mechanism for fuel cells. *Electrochemical and Solid-State Letters*. 2005;8:A273.
- [81] Yousfi-Steiner N, Moçotéguy P, Candusso D, Hissel D. A review on polymer electrolyte membrane fuel cell catalyst degradation and starvation issues: Causes, consequences and diagnostic for mitigation. *Journal of Power Sources*. 2009;194:130-45.
- [82] Hiramitsu Y, Sato H, Hosomi H, Aoki Y, Harada T, Sakiyama Y, et al. Influence of humidification on deterioration of gas diffusivity in catalyst layer on polymer electrolyte fuel cell. *Journal of Power Sources*. 2010;195:435-44.
- [83] Kang J, Kim J. Membrane electrode assembly degradation by dry/wet gas on a PEM fuel cell. *International Journal of Hydrogen Energy*. 2010;35:13125-30.

- [84] Seo D, Lee J, Park S, Rhee J, Choi SW, Shul YG. Investigation of MEA degradation in PEM fuel cell by on/off cyclic operation under different humid conditions. *International Journal of Hydrogen Energy*. 2011;36:1828-36.
- [85] Weng FB, Hsu CY, Li CW. Experimental investigation of PEM fuel cell aging under current cycling using segmented fuel cell. *International Journal of Hydrogen Energy*. 2010;35:3664-75.
- [86] Borup RL, Davey JR, Garzon FH, Wood DL, Inbody MA. PEM fuel cell electrocatalyst durability measurements. *Journal of Power Sources*. 2006;163:76-81.
- [87] Chung CG, Kim L, Sung YW, Lee J, Chung JS. Degradation mechanism of electrocatalyst during long-term operation of PEMFC. *International Journal of Hydrogen Energy*. 2009;34:8974-81.
- [88] Lee C, Mérida W. Gas diffusion layer durability under steady-state and freezing conditions. *Journal of Power Sources*. 2007;164:141-53.
- [89] Parikh N, Allen J, Yassar RS. Effect of deformation on electrical properties of carbon fibers used in gas diffusion layer of proton exchange membrane fuel cells. *Journal of Power Sources*. 2009;193:766-8.
- [90] Chen G, Zhang H, Ma H, Zhong H. Electrochemical durability of gas diffusion layer under simulated proton exchange membrane fuel cell conditions. *International Journal of Hydrogen Energy*. 2009;34:8185-92.
- [91] Wu J, Martin JJ, Orfino FP, Wang H, Legzdins C, Yuan XZ, et al. In situ accelerated degradation of gas diffusion layer in proton exchange membrane fuel cell:: Part I: Effect of elevated temperature and flow rate. *Journal of Power Sources*. 2010;195:1888-94.
- [92] Radhakrishnan V, Haridoss P. Effect of cyclic compression on structure and properties of a Gas Diffusion Layer used in PEM fuel cells. *International Journal of Hydrogen Energy*. 2010;35:11107-18.
- [93] Ha T, Cho J, Park J, Min K, Kim HS, Lee E, et al. Experimental study of the effect of dissolution on the gas diffusion layer in polymer electrolyte membrane fuel cells. *International Journal of Hydrogen Energy*. 2011.

- [94] Ha T, Cho J, Park J, Min K, Kim HS, Lee E, et al. Experimental study on carbon corrosion of the gas diffusion layer in polymer electrolyte membrane fuel cells. *International Journal of Hydrogen Energy*. 2011.
- [95] Aoki T, Matsunaga A, Ogami Y, Maekawa A, Mitsushima S, Ota K, et al. The influence of polymer electrolyte fuel cell cathode degradation on the electrode polarization. *Journal of Power Sources*. 2010;195:2182-8.
- [96] Pei P, Yuan X, Chao P, Wang X. Analysis on the PEM fuel cells after accelerated life experiment. *International Journal of Hydrogen Energy*. 2010;35:3147-51.
- [97] Cho J. Transient response of unit PEM fuel cell under various operating conditions with visualization: Seoul National University; 2008.
- [98] Cho J, Kim HS, Min K. Transient response of a unit proton-exchange membrane fuel cell under various operating conditions. *Journal of Power Sources*. 2008;185:118-28.
- [99] Nam JH, Kaviany M. Effective diffusivity and water-saturation distribution in single-and two-layer PEMFC diffusion medium. *International Journal of Heat and Mass Transfer*. 2003;46:4595-611.
- [100] Kang JH. Study of Transport Phenomena in Multiple Porous Layers of Polymer Electrolyte Membrane Fuel Cells: Pore-network, Lattice Boltzmann, and Experimental Method: Seoul National University; 2011.
- [101] Zhang S, Yuan X, Wang H, Mérida W, Zhu H, Shen J, et al. A review of accelerated stress tests of MEA durability in PEM fuel cells. *International Journal of Hydrogen Energy*. 2009;34:388-404.
- [102] Quick C, Ritzinger D, Lehnert W, Hartnig C. Characterization of water transport in gas diffusion media. *Journal of Power Sources*. 2009;190:110-20.

## 초 록

고분자 전해질형 연료전지(PEMFC)를 부하 변화가 자주 요구되고, 장시간 운전이 요구되는 차량용으로 사용하기 위해서는 과도 응답 특성과 내구성 문제에 관한 연구가 필수적이다. 기체확산층(GDL: Gas Diffusion Layer)은 연료전지 내부의 물질 전달 메커니즘에 직접적으로 영향을 미치는 구성 요소로써 연료전지 성능을 확보하기 위해서는 물 관리 능력을 향상시키기 위한 GDL의 적절한 설계가 중요하게 된다. 하지만 과도 응답 특성 및 내구성 문제는 물질 전달 특성과 관련 있음에도 불구하고 GDL 내부의 이상 유동 메커니즘에 대해 실험적, 수치적으로 해석하기 어려워 물질 전달의 통로가 되는 GDL과 연관시켜 체계적으로 분석한 연구는 거의 없다. 또한 이다. 따라서 본 연구에서는 다양한 실험 결과들과 지배방정식들을 연계 해석하여 GDL의 특성과 내구성능 저하가 PEM 연료전지의 과도응답 특성에 어떠한 영향을 미치는지에 대해 분석하였다.

첫째로 다양한 작동조건에서 과도 응답 특성과 공기극 플러딩 현상에 대하여 분석하였다. 다양한 당량비, 온도, 습도, 플러딩 강도 조건에서 순간적인 전류 밀도 변화에 따른 연료전지 전압을 측정하였다. 또한 가시화셀을 이용하여 공기극의 채널 플러딩 이미지를 얻어 분석하였다. 저부하에서 고부하로 운전시 성능이 순간적으로 하락하는 언더슈트 현상이 나타나고 이는 두 개의 시간 지연 특성을 가지는 사실을 밝혔다. 내부에서 생성되는 물이 채널 표면까지 도달하는데 약 1 초의 시간 오더를 가지고, 이 때 산소의 공급이 일시적으로 저하되어 전압 손실이 발생하게 되어 언더슈트 현상이 나타난다는 사실을 분석하였다.

두번째로 GDL의 구조적 특성이 과도 응답에 미치는 영향에 대해 분석하였다. GDL은 기재, 미세다공층(MPL: Micro Porous Layer)과 MPL 침투층으로 구분할 수 있으며 각각의 설계인자들을 선정하여 다양한 GDL을 제작하여 분석하였다. 기재에 표면적이 넓은 활성 탄소 섬유를 첨가하여 GDL 제작시 첨가되는 탄소 필러, 수지, PTFE의

분포를 조절함으로써 기재의 다공층 구조가 과도 응답 특성에 미치는 영향을 분석하였다. 또한 MPL 침투 깊이, MPL 슬러리 액밀도 조절, 약소수성층 및 pore path 추가와 같은 MPL 설계인자에 따른 과도 응답 특성을 분석하였다. 특히 물을 함유하는 특성을 가진 GDL 의 경우 급격한 부하 변화시에 멤브레인 쪽으로 물을 공급하는 능력이 우수하여 탈수된 멤브레인이 빠르게 수화되면서 이온전도도가 향상되어 성능 회복이 빨라지는 결과를 얻었다. 결과들을 통해 GDL 내부에서 물질전달을 결정짓는 주된 힘은 모세관압 구배이며 GDL 설계에 따라 달라짐을 밝혔다. 이로부터 멤브레인의 물 함유량 회복속도에 GDL 이 영향을 미쳐 연료전지의 과도 응답 특성이 달라진다는 사실을 밝혀내었다.

마지막으로 GDL 의 내구성능저하가 과도 응답 특성에 미치는 영향을 분석하였다. 가속화 내구 평가 기법을 개발하여 GDL 의 소수성 및 구조 변화에 따른 연료전지 동적 성능 변화를 분석하였다. GDL 내부에 발생한 국부적인 소수성 감소지역에 물이 정체되어 국부적 플러딩 현상이 나타나 멤브레인의 수화 및 산소 공급이 불규칙해져 전압 성능이 낮아지고 불안정해지는 사실을 분석하였다. 내구 저하 방법에 따라 GDL 의 각각 다른 부위가 손상되어 성능 저하 양상이 달라짐을 보였다. 또한 포어 네트워크 모델링을 통하여 내구 저하된 GDL 에서의 물 분포를 분석하여 국부적 플러딩 현상이 생기는 사실을 밝혀내었다.

본 연구에서는 물질 전달의 핵심이 되는 GDL 의 구조적 특성 및 내구성능 변화를 고분자 전해질형 연료전지의 과도 응답 특성과 연계하여 체계적으로 분석하였다. 본 연구는 연료전지 모델링 평가 및 검증, 연료전지의 최적 설계 그리고 연료전지 차량의 제어 로직 및 운전 전략을 수립하는데 도움이 될 것이다.

주요어 : 고분자 전해질형 연료전지(PEMFC), 기체확산층(GDL), 과도 응답, 동적 성능, 내구저하, 내구성

학번 : 2008-30198